MULTIPHASE CFD-DEM MODEL FOR GASIFICATION AND MELTING APPLICATIONS

SOON QIAN YI GENEVIEVE

INTERDISCIPLINARY GRADUATE PROGRAMME

NANYANG ENVIRONMENT AND WATER RESEARCH INSTITUTE

2022

MULTIPHASE CFD-DEM MODEL FOR GASIFICATION AND MELTING APPLICATIONS

SOON QIAN YI GENEVIEVE

Interdisciplinary Graduate Programme
Nanyang Environment and Water Research Institute
Environmental Process Modelling Centre

A thesis submitted to the Nanyang Technological University
in partial fulfilment of the requirement for the degree of
Doctor of Philosophy

2022

Statement of Originality

I hereby certify that the work embodied in this thesis is the result of original research, is free of plagiarised materials, and has not been submitted for a higher degree to any other University or Institution.

16/08/2022

Date

gensqy

Soon Qian Yi Genevieve

Supervisor Declaration Statement

I have reviewed the content and presentation style of this thesis and declare it is free of plagiarism and of sufficient grammatical clarity to be examined. To the best of my knowledge, the research and writing are those of the candidate except as acknowledged in the Author Attribution Statement. I confirm that the investigations were conducted in accord with the ethics policies and integrity standards of Nanyang Technological University and that the research data are presented honestly and without prejudice.

16/08/2022
. . . .
Date

Adrian Law
. . . .
Law Wing-Keung, Adrian

Authorship Attribution Statement

This thesis contains material from three papers published in the following peer-reviewed journals in which I am listed as the first author.

Chapter 4 is published as Soon, G., Zhang, H., Yang, C., & Law, A. W. K. (2021). Simulations of Melting in Fluid-filled Packed Media due to Forced Convection with Higher Temperature. *International Journal of Heat and Mass Transfer*, 175, 121358. doi: 10.1016/j.ijheatmasstransfer.2021.121358.

The contributions of the co-authors are as follows:

- Prof Law provided the initial project direction and edited the manuscript drafts.
- I prepared the manuscript drafts. The manuscript was revised by Prof Law, Dr. Zhang and Prof Yang.
- I set up the simulation and wrote the user-defined functions.
- I performed the simulation work at the Nanyang Environment and Water Research Institute. I also analyzed the data.
- Dr Zhang and Prof Law provided guidance with the theoretical formulations and interpretation of the data.

Chapter 5 is published as Soon, G., Zhang, H., Law, A. W. K., & Yang, C. (2022). Modelling of Melting in Packed Media due to Forced Air Convection with Higher Temperature using Euler-Euler-Lagrangian approach. *International Journal of Heat and Mass Transfer,* 194, 123055. doi: 10.1016/j.ijheatmasstransfer.2022.123055.

The contributions of the co-authors are as follows:

- I co-designed the study with Prof Law and Dr Zhang and developed the methodology.
- I set up the simulations and wrote the user-defined functions.
- I wrote the drafts of the manuscript. The manuscript was revised together with Prof Law, Dr Zhang and Prof Yang.
- I performed all the simulations, and Prof Law and Dr Zhang assisted with the interpretation of the data.

Chapter 6 is published as Soon, G.; Zhang, H.; Law, A.W.-K.; Yang, C. (2023). Computational Modelling on Gasification Processes of Municipal Solid Wastes Including Molten Slag. *Waste*, 1, 370-388. doi: 10.3390/waste1020023.

The contributions of the co-authors are as follows:

- I co-designed the study with Prof Law and Dr Zhang and developed the methodology.
- Dr Zhang created the geometry, mesh and initial set up of the simulation.
- I modified the simulations and wrote the user-defined functions.
- I wrote the drafts of the manuscript. The manuscript was revised together with Prof Law, Dr Zhang and Prof Yang.
- I performed all the simulations, and Prof Law assisted with the interpretation of the data.

19/04/2023 gensqy

Date Soon Qian Yi Genevieve

Acknowledgements

I would like to express my deepest appreciation to my supervisor, Professor Adrian Wing-Keung Law, for his constant encouragement and guidance throughout the last four years. Prof Law's passion for research is infectious and under his mentorship, I am inspired to push myself to do better. Whenever I faced challenges, he was patient and understanding and would offer suggestions.

I am also grateful to my co-supervisor, Prof Yang Chun, Charles for sharing his professional experiences, writing feedback and giving me technical advice from a different perspective.

I sincerely thank my mentor, Associate Professor Grzegorz Lisak for sharing his expertise in gasification, which allowed me to see the practical applications of my work. All the professors I worked with are wonderful, supportive mentors and I am truly grateful for that.

I would also like to thank Dr Zhang Hui, who was a role model. She was extremely kind and helpful when I was struggling with the technical aspects in the initial years and was willing to share her experiences.

This study would not have been possible without the financial support of the Interdisciplinary Graduate Programme at the Nanyang Technological University, as well as the Nanyang Environment and Water Research Institute (NEWRI). I deeply appreciate the opportunity that I have been given and the administrative support throughout the four years.

ACKNOWLEDGEMENTS

Special thanks go to the people who made the tough times a little better in their own ways: fellow group members of EPMC (Dawn Pang, Li Min, Pak Hui Ying, Bi Cheng), my peers and friends at NEWRI (Theodora Lee, Ying Lebing, Yuen Jia Wei, Rochelle Silva, Jonathan Tan, Dexter Lay, Arvin Liangdy), the undergraduate students and lab staff I encountered during my time as a teaching assistant, and my family. Thank you for the fun times, encouragement, love, and support, one way or another. I am truly blessed to have known you in my life.

List of Publications

[1] **Soon, G.**, Zhang, H., Yang, C., & Law, A. W. K. (2021). Simulations of Melting in Fluid-filled Packed Media due to Forced Convection with Higher Temperature. *International Journal of Heat and Mass Transfer*, 175, 121358. doi: 10.1016/j.ijheatmasstransfer.2021.121358.

[2] **Soon, G.**, Zhang, H., Law, A. W. K., & Yang, C. (2022). Modelling of Melting in Packed Media due to Forced Air Convection with Higher Temperature using Euler-Euler-Lagrangian approach. *International Journal of Heat and Mass Transfer*, 194, 123055. doi: 10.1016/j.ijheatmasstransfer.2022.123055.

[3] **Soon, G.**; Zhang, H.; Law, A.W.-K.; Yang, C. (2023). Computational Modelling on Gasification Processes of Municipal Solid Wastes Including Molten Slag. *Waste*, 1, 370-388. doi: 10.3390/waste1020023

Table of Contents

List of Figures

List of Tables

List of Abbreviations

CFD	Computational Fluid Dynamics
DEM	Discrete Element Method
DDPM	Dense Discrete Phase Model
DPM	Discrete Phase Model
FC	Fixed Carbon
IBA	Incineration Bottom Ash
KTGF	Kinetic Theory of Granular Flows
MSW	Municipal Solid Waste
RANS	Reynolds-averaged Navier Stokes
UDF	User-defined function
VM	Volatile Matter
VOF	Volume of Fluid
WTE	Waste to Energy

List of Symbols

A_p	Particle surface area
C_d	Drag coefficient
c_p	Specific heat capacity
d	Diameter
E	Energy
$\vec{g}$	Gravitational acceleration
f	Fraction of heat absorbed by particle
$\vec{F}$	Force
$\vec{J}_i$	Diffusion flux of species i
h	Enthalpy
h_c	Convective heat transfer coefficient
h_m	Latent heat of melting
k_f	Thermal conductivity of fluid
k	Turbulence kinetic energy
K	Spring constant
K_{pq}	Interphase exchange coefficient between phase p and phase q
m	Mass
$m_\mathrm{p,0}$	Initial particle mass
Nu	Nusselt number
N_p	Number of particles per parcel
p	Pressure
Pr	Prandtl number
Q	Heat transfer term

LIST OF SYMBOLS

q	Heat flux
r	Radius
R	Net source of species from chemical reaction
Re	Reynolds number
t	Time
T	Temperature
$\vec{v}$	Velocity
S	Source term
x	Position
Y	Local mass fraction of species

Greek symbols

α	Phase volume fraction
β	Mass loss fraction
δ	Particle overlap
ε	Eddy dissipation rate
ρ	Density
η	Coefficient of restitution
$\bar{\bar{\tau}}$	Stress tensor
μ	Dynamic viscosity
μ_{fr}	Coulomb friction coefficient
γ	Damping coefficient

Subscripts

coll	Collision
f	Fluid
g	Gas
i	Index representing chemical species in mixture
l	Liquid
p	Particle
p,0	Value of assigned variable when first reaching solidus temperature
pa	Parcel
ref	Reference

Abstract

Due to the increase in urban population and consumption, there is an increasing need for evolving waste management technologies to deal with the excessive solid waste produced. Gasification is one proposed technology that achieves greater waste volume reduction compared to other thermal processes. Hence, the optimization, stability and reliability of commercial gasifiers is important, especially when diverse feedstock and waste streams are present. Other than conducting pilot trials and experiments, numerical simulations have been adopted as useful tools for modelling the chemical and physical processes to modify operating conditions and predict the resultant effects.

The study is targeted to develop a numerical modelling approach to model the melting and phase-change process in multiphase flows for gasification and other applications. A melting model that could be used for isothermal and non-isothermal melting in packed beds was established with the combination of computational fluid dynamics and the discrete element method. At present, the state-of-the-art numerical models are not found to be suitable for melting for independent, three-phase flows within packed beds, especially for complex processes such as gasification with chemical reactions. Throughout the study, some methods of reducing computational costs in particle-fluid simulations were also investigated and adapted to the model. The limitations of the approach and comparison with other approaches were also reviewed.

Application examples were used to demonstrate the capability of the melting modelling approach developed in this study. The isothermal melting of a single ice particle and a packed bed of ice flowing under warm water convection were examined as a first step. The simulations were validated against experimental results and found to be satisfactory. Insights were also obtained with regards to the modification of the mesh-particle size ratio and determination of the values of the spring constant and restitution coefficient in the linear spring-dashpot particle collision model. Subsequently, the non-isothermal melting of a wax layer in an inert packed bed under air convection was simulated. In the utilization of the approach for three-phase flows, the governing principle of particle energy balance was established together with a novel concept of particle "enthalpy" being introduced for non-isothermal melting. Due to the nature of the three-phase flow, this approach allowed for the tracking of the liquid phase and permeation through the packed bed, as well as the viewing of the formation of gas channels. The approach was also deemed to be compatible with coarse-graining, and useful in certain applications over other multiphase modelling approaches.

Lastly, attempts were made for further extension of the modelling approach for application in a prototype gasifier, including the full-scale gasification chemical and physical processes (vaporization, devolatilization, combustion and melting). However, various challenges were encountered during this process, particularly with numerical instabilities and uncertainties stemming from the approach being coupled with the commercial software. Nevertheless, the lifetime and process of a sample MSW particle was able to be predicted, and a comparison was carried to determine the effectiveness and need for slag recycling in the prototype gasifier.

In conclusion, a novel modelling approach was developed in this study for melting which can be used to improve and predict conditions in reactors. By tracking each particle individually, the model is well-equipped to simulate the packed bed in a discrete manner, allowing for unique particle temperatures, composition, and melting rates. The model has the potential to improve gasification performance as it is able to assess the performance of changing operating parameters at the design and operational stages. The use of various methods to reduce the high computational costs of modelling phase-change in large-scale facilities was also investigated, and the simultaneous melting and tracking of liquid phase within the solid packed bed was able to be predicted.

Chapter 1. Introduction

1.1 Background

Ever since the Industrial Revolution in the 18th century, the world population and standard of living has grown exponentially, especially for developed countries. On average, in 2016, 0.74 kg of municipal solid waste (MSW) was generated per person daily, ranging from 0.11 to 4.54 kg. Globally, the amount of waste that year was 2.01 billion tonnes and is forecasted to reach 3.4 billion tonnes annually by 2050 [1]. Due to this rapid production and consumption, a concern that has received growing attention is the management of the waste produced.

Improper solid waste management practices can lead to many problems: ocean and land pollution, groundwater contamination, greenhouse gas emissions, transmission of diseases and unsanitary living environments near open dumping areas. The type of practices which a country adopts, ranging from open dumping, controlled landfills, to incineration, and materials recovery, is correlated to its income [1]. Proper solid waste management is especially important in densely populated urban cities such as Singapore, due to the sheer volume of waste generated and the lack of land space for landfills. Since the 1970s, Singapore has relied on incineration to achieve a dual purpose of waste volume reduction as well as electricity generation [2]. Approximately 2 100 tonnes of non-incinerable waste and incineration ash are sent to Singapore’s last landfill, Semakau Landfill, daily from the four waste-to-energy plants. However, it is expected to be filled by 2035.

As the primary method of waste management used in Singapore, the incineration process converts MSW to ash, flue gas, and heat, which can be recovered to generate energy. Due to its high moisture content and heterogenous composition, MSW is a low-quality fuel which does not provide high calorific value. To obtain higher value products and minimize waste residues, alternative Waste to Energy (WTE) technologies to incineration are currently being explored [3].

One such proposed alternative is MSW gasification. Commercial gasification has been around since the Industrial Revolution, with the initial use of wood and coal in compact gasifiers to power vehicles [4]. The 1970s saw the development of one-dimensional numerical models for packed-bed coal gasification to improve the process by correlating product gas compositions with operating parameters [5-7]. Subsequently, biomass gasification continued to be used for electricity production, especially for developing countries where biomass was cheaper than fossil fuels [8].

The use of MSW in co-gasification started with the search for more renewable sources of fuel [9-11]. However, the challenge for MSW arises from its high moisture content, resulting in a need for pre-processing the wastes, i.e. the need for additional heat sources. Nevertheless, if successful, MSW gasification can be a source of renewable energy, high volume reduction of waste, saving on landfill space [12, 13]. More importantly, there has been rising interest in repurposing the by-products of MSW incineration and gasification, such as in Singapore where field trials are in place to test the NEWSand, a material generated from incineration bottom ash (IBA) and slag [14]. These by-products were previously regarded as waste and would be treated then disposed of in landfills. However, if they can be recycled, it will help close the waste loop, and aid in the country's vision of Zero Waste.

Potential uses of MSW fly ash include concrete aggregates, soil stabilization, manufacturing of ceramics and glass [15]. It was found that MSW ash could be used to replace cement in mortar and did not affect compressive strength. MSW slag can also be used to make glass-ceramic foams due to its glass-like and leaching resistant nature, and even have higher compressive strength than those made from waste glass and coal ash [16]. Slag from steelmaking or blast furnaces in the industry has long been re-used for other purposes such as the replacement of concrete aggregates, manufacturing of cement, and for pavement and road construction [17]. Similarly, slag produced from local MSW gasification could be used in the manufacturing of cement and partial replacement of fine aggregates, creating a positive environmental impact and reducing greenhouse gases discharged into the atmosphere through the reduction in imports of conventional materials.

1.2 Motivation

The increasing need for alternative waste management technologies has led to heightened interest in gasification over the past decades. Experimental studies conducted at pilot plants offer insights into stability of plant operation, feedstock blending and consumption rate, gas cleaning requirements, suitability of the gasifying agent and other operating parameters [18-20]. However, in full-scale facilities, it is often difficult to predict or observe actual conditions in the reactors. While high temperature slagging gasifiers are useful in removing ash residues and separating metals, the high temperatures mean that sensors and cameras are often mounted near the walls or gas exits, and it is difficult to observe the reactions happening inside the waste bed. Additionally, while adjustments such as air flow rates, feed loading rates or blending of feedstock can be experimented with and optimized, it is both time-consuming and prohibitively expensive for other parameters such as geometry of the gasifier, material and thickness of the refractory wall to be changed. Thus, various approaches such as computational fluid dynamics (CFD), artificial neural networks, thermodynamic equilibrium and kinetic models have been used as tools to predict the effect of changing operating parameters [4, 21]. Due to the limited scope, this thesis will focus on the existing CFD approaches.

There are currently a few existing approaches to model multiphase flows, depending on the volume fraction of the different phases and the related engineering applications. In these approaches, the solid phase is typically modelled via either an Eulerian or Lagrangian representation, while the fluid phases are modelled in an Eulerian manner. For example, the Eulerian approach has been adopted for the flow simulations of all three phases (gas, liquid, solid) in bubble columns [22]. However, this assumes that the solid phase is treated as a continuous medium with volume-averaged properties and does not allow for distinct, observable solid-solid interactions. In cases where interactions within the solid phase are important, such as for packed beds and granular mixing, the Lagrangian representation is preferred for the solid phase because it can provide a more accurate representation on the particle collisions as well as the particle size distribution. In such cases, the Volume of Fluid (VOF) method is commonly adopted to model the two-phase (fluid-solid) flows with a Lagrangian solid phase and an Eulerian composite fluid (gas and liquid) phase for the analysis [23, 24].

There is more complexity to the multiphase flow modelling when phase-change processes, such as melting, are involved. The melting of materials can be classified as isothermal (at a constant temperature, typically for pure materials) and non-isothermal (over a temperature range, typically for mixtures or alloys). The challenges of extending from isothermal to non-isothermal melting include the need to simulate the transition state of softening between solid and liquid as well as to quantify the subsequent liquid movement through the solid matrix over the temperature range. In particular, the transient semi-solid properties during softening are very difficult to determine, at the same time they are essential so that the interactions between the surrounding solid and liquid phases can be well represented.

CFD modelling coupled with the Discrete Element Method (CFD-DEM) is a well-developed Eulerian-Lagrangian approach that has been used extensively to simulate granular flows in packed and fluidised beds [25-27]. Originally developed by Cundall and Strack [28], DEM adopts a soft-sphere model that allows for the collisions among particles via particle deformation. Due to the individual tracking of particles, CFD-DEM can account for a wide distribution of particle sizes, and thus it can potentially provide a more accurate representation of the melting process. Despite this potential advantage, simulation studies with CFD-DEM that involve melting are rarely reported in the literature due to technical challenges, such as high computational costs, complexity in building melting models and representation of three-phase flows, and only a few studies have been mentioned up to now.

When the melting involves gas-solid packed beds, such as in the gasification processes and blast furnaces, no study has been reported to the best of our knowledge that includes the melted liquid phase and its subsequent flow through the packed bed, i.e., the full representation for the three-phase flow. Such three-phase representation can however enable the prediction of the movement of the melted liquid in the reactor, which is an important consideration in various engineering applications. For example, in solid waste gasification, it is of utmost importance to ensure that the melted liquid is able to flow through the bed towards the tapping point, especially with the temperature distribution inside the bed being non-uniform and possibly lower than the melting temperature. Thus, to address this technical gap, there is a need to develop an approach to simulate the melting process and subsequent liquid flow within gas-solid packed beds, taking into account the full three-phase considerations and computational costs. The simulation would then aid in the visualization of clogging points or areas with lower temperature so that changes in operation or design could be made to the gasifier to improve its performance.

1.3 Objectives

This thesis aims to develop new approaches for the numerical modelling of three-phase flows and melting for gasification applications. In particular, the goal for simulating melting in high-temperature gasification processes in prototype reactors is considered. The overarching objective of this study is to contribute to the advancement of modelling approaches for the melting process without compromising on accuracy.

The study involves the following scope of work:

- Develop and validate a novel approach for simulating the isothermal and non-isothermal melting process.
- Apply the developed approach to various practical applications, particularly for large-scale reactors where savings in simulation runtime are of high importance.
- Simulate the melting and tracking of the subsequent liquid flow through packed beds with the appropriate interphase heat and momentum exchanges.

1.4 Organization of the thesis

This thesis is organized into seven chapters.

Chapter 1 presents the background and objectives of the study, and also provides the motivation behind the research topic.

Chapter 2 reviews the existing research conducted, covering specifically both experimental and numerical studies on gasification, numerical modelling approaches of general multiphase flows, and coupling frameworks to model the different phases. It also describes the existing progress of phase-change modelling for melting in practical applications and the process of slag formation.

Chapter 3 details the conceptualization and development of the developed approach, henceforth referred to as CD-MELT, for both isothermal and non-isothermal melting, as well as for simultaneous combustion and melting. The formulation and challenges of the drag force representation are also discussed. Certain challenges of numerical instabilities during the development of the melting model are also described in this chapter.

Chapter 4 reports the use of CD-MELT to simulate the two-phase isothermal melting of a packed bed of ice particles under forced warm water convection. The predicted melting rate of the ice particles and their heat and mass transfer with the surrounding water are compared with experimental data in the literature under different inlet water temperature and flow velocity. The effect of mesh-particle size ratio on the predicted results is also investigated to evaluate the model's reliability.

Chapter 5 describes the utility of CD-MELT in an application example with three-phase flow and non-isothermal melting. The simulation of the melting of a layer of wax particles in a packed bed of glass particles was conducted and the predictions were then compared with the experimental data in the literature. In order to simplify the modelling, the compatibility and validation of coarse-graining with CD-MELT was also investigated. The composite VOF approach was also compared theoretically with the developed Eulerian-Eulerian-Lagrangian approach.

Chapter 6 describes the use of CD-MELT in the prototype application to gasification, including chemical reactions and simultaneous combustion and melting of MSW and slag. The effect of slag recycling is investigated numerically, with emphasis on the tracking of liquid molten slag as it permeates through the packed bed.

Chapter 7 presents the main conclusions and recommendations for future work.

Chapter 2. Literature Review

This chapter focuses on the existing literature with regards to the existing studies involving gasification, CFD simulations of phase-change, and combination of the two. The state-of-the-art approaches for simulating the melting process are also presented and reviewed. Traditionally, the main feedstock used in gasification is coal, with biomass and MSW increasing in viability as strong alternative fuels and promising renewable energy sources. Existing research on gasification can be broadly classified into two main categories; firstly, the optimization of existing gasification processes and parameters to increase efficiency, and secondly, improvements towards the design of gasifiers to reduce operational costs and mitigate common problems.

2.1 Optimization of existing gasification processes and parameters

The process of gasification refers to the thermal conversion of biomass or carbon-based materials into synthesis gases (syngas), typically at extremely high temperatures. By providing a lower amount of oxidant, usually oxygen or air, the fuels are partially combusted to produce the heat required to convert the rest to the syngas mixture of carbon monoxide (CO), hydrogen (H_2), carbon dioxide (CO_2), nitrogen (N_2), and small amounts of methane (CH_4), tar and ash [29]. The syngas can then be collected and stored as fuel for future use, among other advantages such as its flexibility to handle different types of waste due to higher operating temperatures (>700℃), providing greater energy security by reducing reliance on fossil fuels, cleaner emissions during the gasification process, and socioeconomic development from the production of fuels [8]. The gasification process consists of five main stages: heating and drying, devolatilization, combustion, cracking, and reduction. For slagging gasifiers, due to the higher temperatures (up to 2000°C), there is an additional stage of melting of the incombustible fractions into slag, which significantly affects their design and operation. Hence, much efforts have been focused into the modelling and study of slag formation, which will be reviewed in detail in Section 2.3.2.2.

There are three main kinds of gasifiers: fixed bed, fluidized bed, and entrained flow, as shown in Figure 2.1 [30]. When deciding what type of gasifier to be built, the type of feedstock and available footprint must be considered. The unique issues to each type of gasifier will be elaborated in the following.

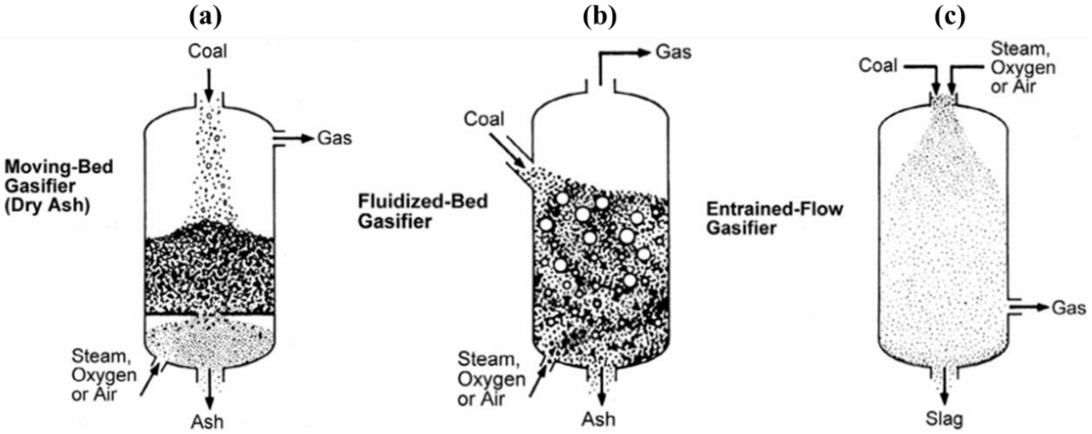

Figure 2.1. Types of gasifiers: (a) Fixed bed gasifier, (b) Fluidized bed gasifier, (c) Entrained flow gasifier [30]

Fixed (or moving) beds use a static or slow-moving waste bed while the oxidizer is passed through it, and the processes usually occur at different zones of the bed [31]. The feedstock is typically fed from the top and heated by the hot air before reaching the gasification zone. Particle residence time is in the order of hours. Advantages of fixed bed gasifiers are the low oxidant requirements and high methane content in the syngas. The main disadvantage is that fixed beds are unable to handle fine particles [30]. For this study, the focus is on modelling the melting in slagging gasification for fixed bed gasifiers.

Fluidized bed gasifiers consist of the waste bed being suspended by the oxidizer, such as air, with feedstock being continually fed ensuring fast mixing. The mixing ensures that temperatures are uniform throughout the bed. The particle residence time in a fluidized bed is shorter than in a fixed bed gasifier and oxidant requirements are moderate. Sometimes, the smaller particles are blown out of the gasifier and re-circulated into the gasifier to maintain stability [32]. It was found that a larger particle size distribution width improved the gas yield and gasification performance [33]. To evaluate the stability of plant operation, key control parameters that were used include fluctuations in the vertical temperature and exhaust gas composition profiles [20].

Lastly, for entrained flow gasifiers, the fuels and oxidizer are being fed in through the top, resulting in the oxidizers entraining the particles in a densely-packed cloud, and most of the ash being removed as slag at the bottom due to high operating temperatures. Particle residence time is in the order of seconds, thus higher operating temperatures are required for complete reactions. Entrained flow gasifiers have large oxidant requirements and typically use oxygen instead of air [30]. Due to the injection of very fine particles at high speeds, the effect of turbulent mixing and fluctuation on the heterogenous char particle reactions has been observed to be more significant in the flame region rather than the nonflame region [34].

Existing experimental and numerical studies cover a wide range of parameters to improve the gasification process and quality of the syngas. Pre-processing of feedstock, modifying operating conditions (air flow rates, blending ratios, bed temperatures, pressure, gasifying agents) are only a few of the numerous conditions that can be adjusted for each gasification system. The effects of operating pressure and temperature on syngas composition were simulated through thermodynamic equilibrium calculations [35]. Regardless of the type of gasifiers, experimental studies conducted in pilot plants mainly focus on the feasibility of co-gasification of various types of feedstock and fuel/air equivalence ratio, and how they impact tar formation, vertical temperature profiles, syngas composition and gasification efficiency [19, 20, 36]. Hence, the research interest is largely on finding alternative, renewable sources of feedstock, while still ensuring steady plant operation and high heating value of the syngas. Numerical studies also show that the type of model chosen, such as the turbulence and devolatilization rate model would affect the exit gas composition and temperatures [37].

2.2 Common operating issues of slagging gasifiers

For slagging gasifiers, which are operated at higher temperatures than conventional gasifiers, much of the available literature focuses on the formation of slag and how it affects gasifier performance. Slag is primarily formed through the melting of inorganic matter such as metal oxides or silica, depending on the fuels used. This inorganic matter, if not removed, can cause issues when deposited as fine ash particles in subsequent processes [38]. Hence, it is important to maintain a continuous, steady discharge of liquid slag from the bottom of the reactor, through an understanding of the mineral composition in the raw material, ash fusion temperature, viscosity of the resulting slag, which could differ significantly between operations. During the gasification process, slag is observed in two places; firstly, on the walls of the gasifier when particles become trapped and melt in a viscous layer, and secondly, when this viscous slag layer flows to the bottom of the gasifier before exiting at the tapping hole. For fixed bed gasifiers, where the high temperatures occur within the packed bed, the slag layer at the bottom is also contributed by melting within the bed, which then permeates through the bed and is subsequently discharged.

Different types of gasifiers have their own unique operating issues, as shown in Figure 2.2 [39], hence the research in this area largely differs depending on the type of gasifier used. There are two ways in which slag formation affects the efficiency of the gasifier. Firstly, the viscous layer formed on the refractory walls lowers the combustion efficiency [40]. When molten slag penetrates into the refractory lining, it causes damage to the reactor wall, increasing the downtime of the gasifier during replacement of the liner [41]. The failure of the refractory lining has been a strong push for more research to be conducted in improving the durability of the refractory materials, and Bennett et al. [42] attributed refractory wear to a number of issues, as shown in Figure 2.3. Hence, the existing research focuses on understanding what parameters affect the slag layer thickness on the refractory wall, chemical interactions at the slag/refractory interface, or the development of new refractory liner materials.

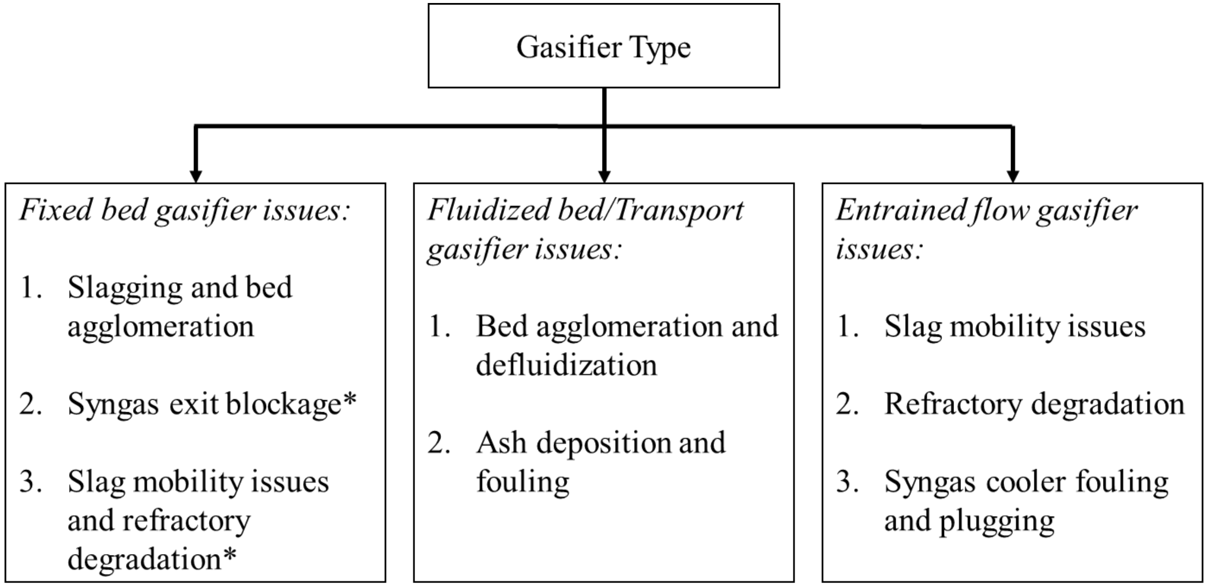

Figure 2.2. Operating issues due to mineral matter in various types of gasifiers (* specific to slagging fixed bed gasifiers) [39].

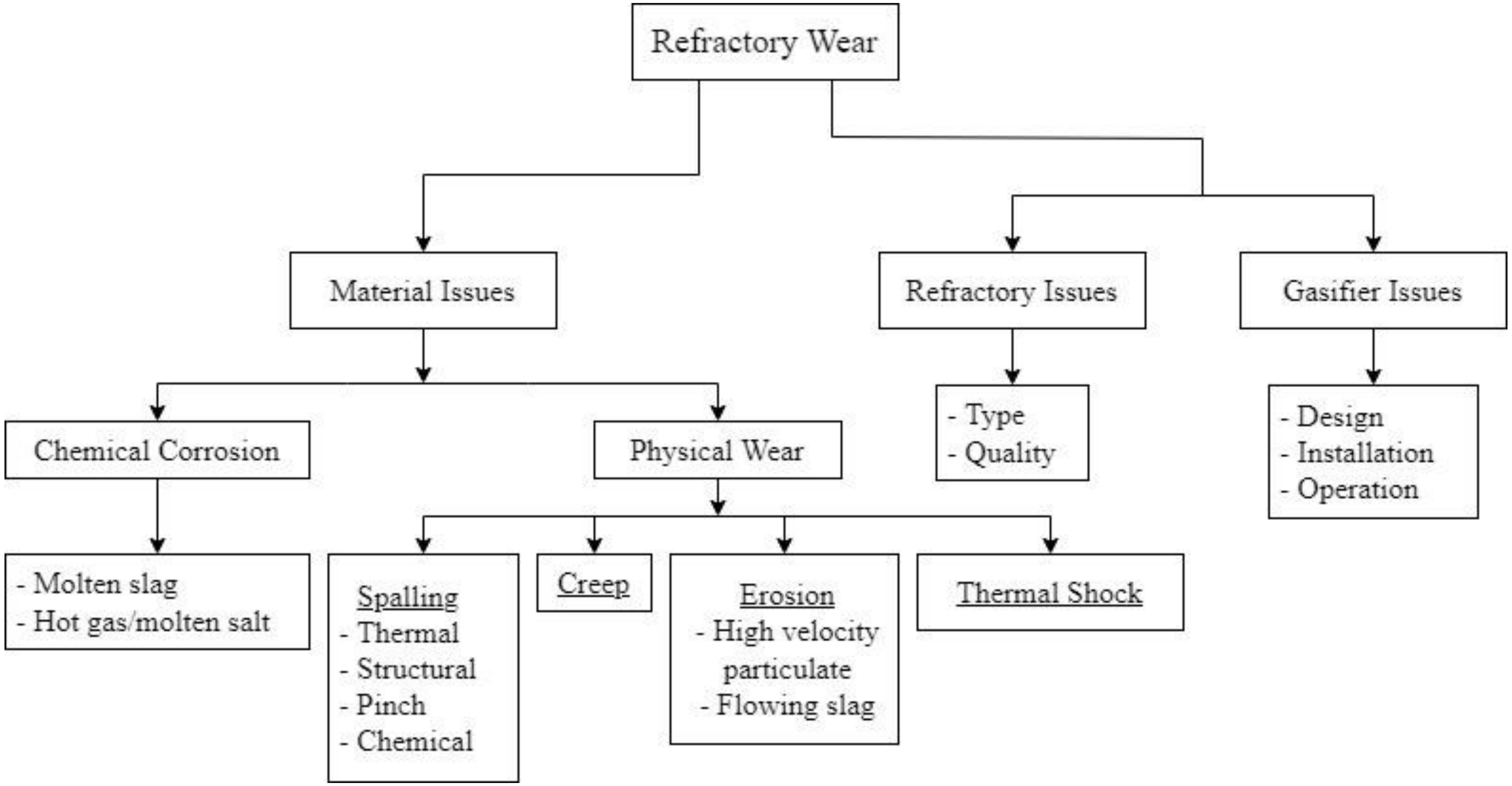

Figure 2.3. Causes of refractory wear and failure in gasifiers [42].

Secondly, clogging can occur near to or at the tapping point of the gasifier, which in worst-case scenarios, can cause emergency shutdowns and unreliability of the system. The slag deposition above the tuyeres and blockage of the gas nozzles leads to an unbalanced distribution of oxygen and steam. In turn, the temperature within the bed becomes uneven, increasing the slag viscosity and reducing discharge. The consensus in the existing literature is that to maintain the smooth operation of the gasifier, there is an optimum or critical slag viscosity for steady slag discharge [43]. The operating temperature in the gasifier, which directly affects the slag viscosity, is thus the most important parameter and has to be selected carefully based on the ash flow temperature and slag composition.

These two main issues of refractory wall damage and clogging could be mitigated by either (a) having better process monitoring, which involves the upgrading of sensors and constant replacement with the current state-of-the-art technology or (b) using a model to predict temperatures and slag flow within the gasifier and adjusting operating parameters accordingly [44]. Ideally, both strategies could be combined by using sensors to monitor the ongoing process, reinforced by a digital model to enhance preventive maintenance or make predictions for unconventional or unexpected scenarios.

2.3 Computational fluid dynamics simulations for multiphase flows

Multiphase flow phenomena occur in many engineering systems, such as splat formations [45], granular heat transfer in packed beds [46], energy storage systems [47], thermal processes of incineration and gasification for solid wastes [4], etc. Numerical simulations have become an important element in the design and operation of engineering reactors, particularly as tools to quantify and improve their performance [48-50]. The formulation of a numerical model can be validated in a smaller pilot scale and then expanded to predict the outcomes in a full-scale facility [51, 52]. Significant advancements on the adoption and usefulness of CFD models in real engineering applications have been reported recently, for example in biomass gasification and chemical process systems [53-55]. At the same time, the simulations of multiphase flows, whereby the interactions among the different phases (solid, liquid and gas) need to be accurately reproduced in order to predict the operating conditions, remain challenging [56].

CFD models are often used to simulate the freeboard region above the waste bed [56, 57]. One of the methods used is the finite volume method. After the geometry of the reactor is created, the fluid domain is then meshed and divided into discrete control volumes (cells). By integrating the governing equations of conservation of mass, momentum, energy and species over the individual cells, algebraic equations can be solved for the variables of interest. If required, additional physical models can be included to further improve the accuracy of the simulation, but also increase the computational time.

A wide variety of software and numerical methods have been used to simulate gasification with different kinds of feedstock as well as reactors [4]. This shows how complex the gasification process is, and there is no consensus on which the best method is, or to compare factors affecting syngas composition under diverse conditions. Nevertheless, CFD has been used to optimize parameters such as moisture content, air flow rates, and reactor temperatures [58-

60]. Deng et al. [57] used CFD to model coal gasification in a pressurized spout-fluid bed, concluding that pressure and bed temperature had significant effects on improving gasification performance.

While the finite volume method (an Eulerian approach) is the most common method for the modelling of fluid phase(s), there is a wider variety for the modelling of the solid phase, in an Eulerian or Lagrangian manner, which is then coupled with the fluid phase(s).

2.3.1 Fluid-solid coupling frameworks

There are two main approaches for the numerical simulations, namely the Eulerian-Eulerian and Eulerian-Lagrangian approaches, with their key difference on how the solid phase is tracked. Both approaches have been used to model gas-solid flows [56]. In the Eulerian-Eulerian approach, the multiple phases are not distinct from each other but treated in a simplified manner as inter-penetrating continuum instead via the conservation equations for mass, momentum and energy, with the simplification leading to significant savings in computational time and resources. However, when more details on the individual phases are required, the Eulerian-Lagrangian approach needs to be considered, whereby the solid phase is tracked as discrete particles, and the particle trajectories through the flow field are simulated separately to predict the associated heat and mass transfer. The particle tracking also enables the modelling of particle-particle interactions. The Eulerian-Lagrangian approach is generally very computationally intensive, especially under conditions of extensive fluid-particle mixing whereby very small timesteps as well as fine meshes are needed to ensure accuracy. In addition, when the reactor contains high volume fractions of solid phase with the associated large number of particles, very long simulation runtimes are typically required. Furthermore, when melting is involved, its simulation would impose further complexity.

Fixed bed gasifiers assume that most of the waste is concentrated at the bottom of the gasifier, forming a waste bed. In such cases, the main interactions between the freeboard region and the waste occur at the top of the bed. This can be simulated by solving the freeboard region and waste bed region either separately [61] or simultaneously [62], depending on the processing capacity of the simulation equipment and intended degree of accuracy. The outputs of each model at the interaction surfaces are fed as inputs to the other model, and this process is called coupling. As shown in Figure 2.4(a), if only one phase is affected by the other, this is known as one-way coupling; otherwise, if both phases affect each other, two-way coupling. Lastly, four-way coupling is when the discrete phase has interactions within itself, such as when there are particle interactions through collisions. Often, the consideration of which coupling procedure to use is determined by how dense the particle flow is in the fluid, and can be estimated by comparing the dispersed phase volume fraction and inter-particle spacing [63], as shown in Figure 2.4(b).

2.3.1.1 Eulerian-Eulerian approaches

In a Euler-Euler approach, both the fluid and solid phase are modelled as inter-penetrating continuum. This results in each phase being represented by its volume fraction in each cell. There are three models to achieve this: the VOF model, the mixture model, and the Eulerian model, sometimes known as the Eulerian-Eulerian Two Fluid Model [32]. In the VOF model, the volume fraction

α is set to be 1 if the cell is filled with solid phase, 0 if the cell is filled with fluid phase, and between 0 to 1 to represent an interface between the two phases. For the Two Fluid Model, the solid phase is represented by the Eulerian granular model using the kinetic theory of granular flows (KTGF) for closure, and includes provisions for packing limits, granular temperature, solids pressure on walls, and interphase interactions, while the gas phase is treated as a continuum.

Couto et al. [62] developed a 2D Eulerian model for the MSW gasification in a fluidized bed in order to validate the experimental steady-state syngas composition of Xiao et al. [64]. The approach was also used to model a bubbling fluidized bed gasifier of coal and limestone, varying different parameters to test the effect on exit gas composition [65]. Extensive studies using a two-dimensional fixed bed model gave insight on the optimization of the fixed bed reactors, by examining the effects of the moisture content, particle size, primary air and ash content [59, 66-68]. However, when the particle sizes are large, the bed cannot be assumed to be a continuous medium as each particle reacts individually [69]. Additionally, as bed properties are averaged, the Euler-Euler approach is unable to model particles of different diameters simultaneously, which could affect combustion rates, temperatures or mixing rates within the bed. Hence, the Euler-Lagrange approach provides a more precise representation and is explained in the next section.

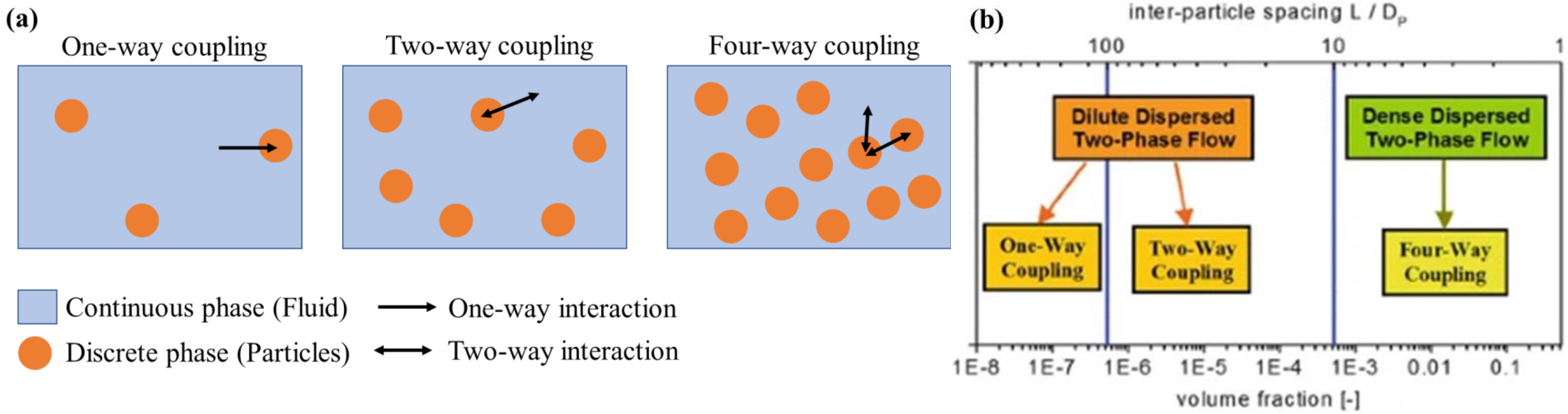

Figure 2.4. (a) Schematic framework of one-way, two-way and four-way coupling between fluid and particles; (b) Determination of coupling framework via inter-particle spacing and dispersed phase volume fraction [63].

2.3.1.2 Eulerian-Lagrangian approaches

In the Euler-Lagrange approach, the main difference is the solid phase is not continuous, but rather tracked via particle trajectories as they are transported through the flow field. For the Discrete Phase Model (DPM), the volume fraction of the solid phase is assumed to be less than 10% [70], and the phases can exchange mass, momentum, and energy. There have been many 3D CFD models used to simulate the combustion process [61, 71, 72]. Costa et al. [73] used a 3D CFD model to model the refuse-derived fuel incineration process. DPM was used to simulate fly ash particles, however the bed itself was modelled via boundary conditions to the CFD model. It is noted that with this approach, particles are usually assumed to be thermally thin with low volume fractions and the particle-particle interactions are ignored, thus saving on computational costs.

In order to simulate regions where particles have high volume fraction compared to the gas phase, such as a densely packed waste bed, the Euler-Euler approach is commonly used instead. Typically, the two-fluid model is limited by the inability to represent differing particle sizes with reasonable computational time, and the particle-particle interactions are assumed to be negligible. Instead, the hybrid Euler-Lagrange Dense Discrete Phase Model (DDPM) can be used. In this approach, the volume fraction and velocity field of the solid phase is taken from the Lagrangian solution, as in DPM, however, in the continuous phase equations, the volume fraction of the discrete phase is also accounted for. This approach has been used to successfully model a 3D circulating fluidized bed of coal transport and combustion [70].

In the DDPM, particles or groups of identical particles, known as parcels, are tracked individually in the system by solving the Newton's equations of motion, exchanging mass, momentum, and energy with the continuous phase via source terms at each time-step for a transient model. For a steady-state model, calculations are performed for both phases until the desired residuals are low enough to be considered as converged. Conversely, for a transient model, two-way coupling is performed by solving the CFD flow field for a flow time-step, thus generating the forces such as drag on the solid or liquid particles. Next, the particles will be iterated at smaller time-steps until synchronization, taking into account particle-particle collisions and updating particle properties such as velocity, position and temperature. These properties will then be used to recalculate the phase volume fraction at each fluid cell and to update mass, heat, and momentum exchange terms to the fluid phase and subsequent time-step calculation, repeating until the desired simulation time is reached [74].

A further refinement to the DDPM is the consideration of the particle-particle interactions, i.e., the four-way coupling. The Discrete Element Method (DEM) is a particle-based Lagrangian approach, describing the mechanical behaviour of particles. Traditionally, DEM has been used for applications where there is a high volume fraction of particles, such as in fluidised beds, and granular flow in hoppers, catalyst manufacturing involving very fine (micro-level) particles [26, 27]. With the recent increase in processing power and advancements in DEM techniques, it has been extended to include chemical reactions for simulating incineration [21, 75], coal combustion [76], and biomass gasification [52, 77]. An example of the solution procedure for reactive gas-solid flows is shown in Figure 2.5 [55].

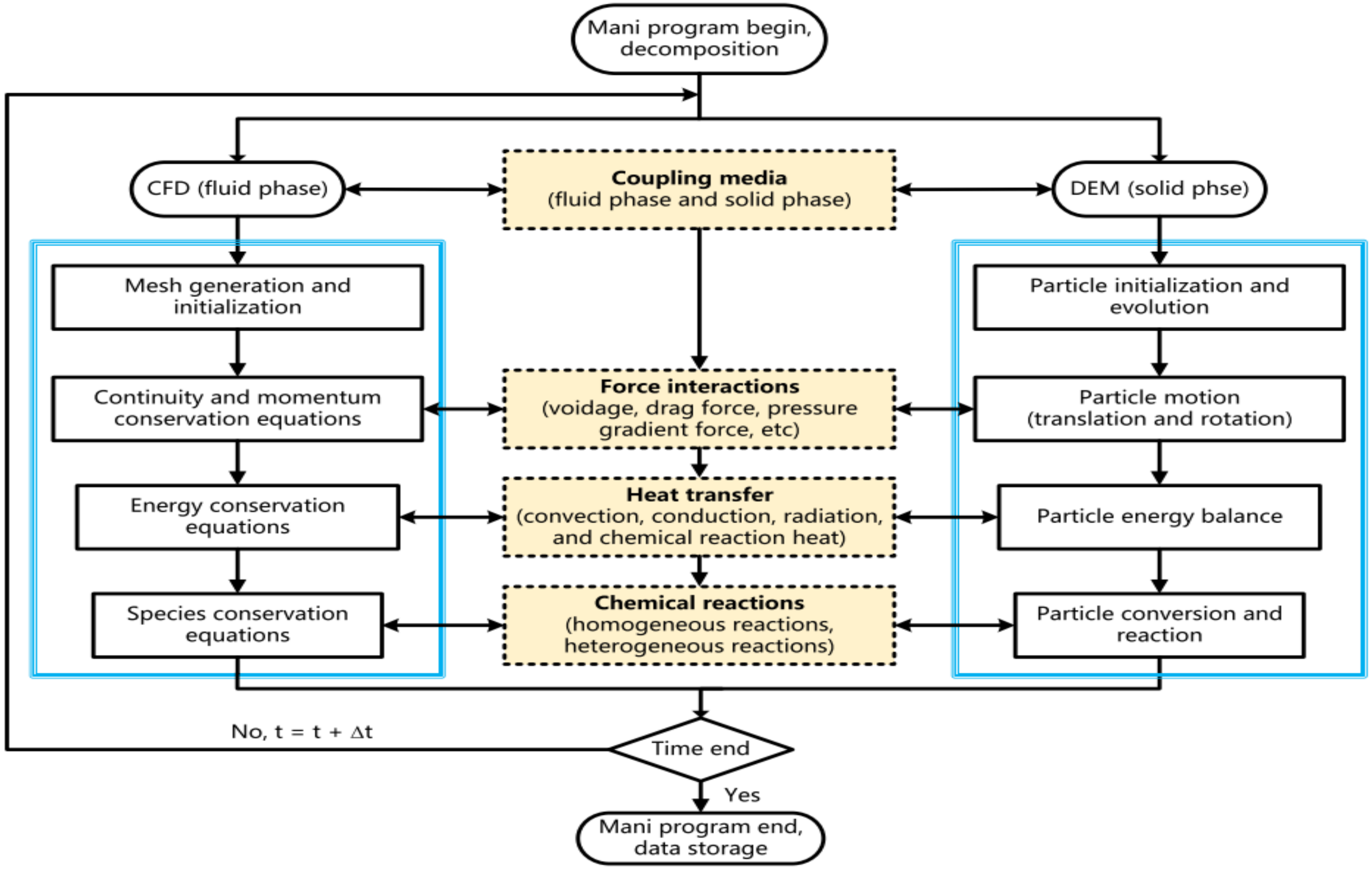

Figure 2.5. Typical solution procedure for CFD-DEM coupling for gas-solid flows with chemical and physical reactions [55].

The main assumption in DEM is that the particles only interact with each other when they are in contact, and the time step is small enough such that disturbances from each particle only affect neighbouring particles. First developed by Cundall and Strack [28], the forces between particles are calculated using a soft-sphere model, where particles can “overlap” slightly upon collision, producing a deformation as shown in Figure 2.6. This deformation can then produce a contact force from the force-displacement law, which is exerted on the particles.

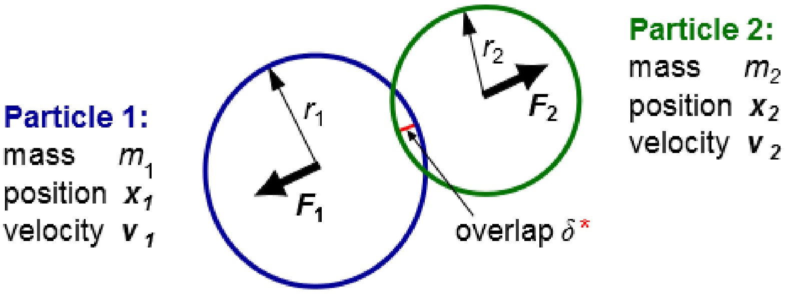

Figure 2.6. DEM soft-sphere model: overlap during particle collision [78].

Within the DEM collision models, there are several models that can be used to describe the particle-particle collisions and calculate the normal contact force [79], as shown in Figure 2.7. The linear spring-dashpot model in Figure 2.7(a) is one of the methods used to calculate the normal contact force, which was used in this work since it is less computationally expensive and intuitively understood. The force during collision is modelled by a spring-dashpot system, where upon collision with another particle or wall, the particle experiences a force as if it was “released” like a spring, but this force is also being damped by a dashpot, which represents the loss in kinetic energy. The main underlying assumptions are that the collision is inelastic, and some of the energy is dissipated during the contact. Particles after the collision will also be slower than before the collision, with the velocity ratio denoted by the coefficient of restitution.

Previous efforts have been taken to compute the actual spring constant using the non-linear spring-dashpot Hertzian contact theory or the Hertz-Mindlin theory [80], however, there is evidence that the use of unrealistic lower values of spring constant allows a larger time-step to be used [27, 81]. Navarro et al. [82] agreed that spring constant should be adjusted such that particles will not penetrate each other, yet not too high to require a small and computationally expensive time-step. The justification is that the particle motion is mostly caused by the fluid, and not significantly affected by the smaller spring constant. Additionally, spring constant is inversely related to the time-step: the smaller the spring constant, the larger the collision time. In order to resolve the collision accurately, the time-step must be smaller than the collision time. Hence, a smaller spring constant would enable the use of a larger time-step.

The most suitable collision model depends on the situation and the properties of the particles involved. Examples include the visco-elastic model [83], which includes a viscous damping term to model the energy dissipation. This is shown in Figure 2.7(c), where the hysteresis in the stress-strain curve shows that the material deforms slowly under stress. However, once the force is removed, it returns to the original form. The area enclosed by the curve represents the energy loss during this process. Similarly, there is energy dissipation during the particles' collision, as the boundary is compressed and released. Commercial software ROCKY-DEM uses an elastic-plastic model where force depends on extent of overlap [84]. It should be noted the force calculated from these elastic models are purely repulsive. Thus, the model would not be suitable for particles with cohesive and adhesive forces, for example the ash may have adhesive properties when it melts to slag. To address this issue, Wissing et al. [85] modified the normal contact force model by relaxing the spring with a lower stiffness k_2 until the minimum overlap. At this point, the negative force representing adhesive force is included, and a different spring constant k_c is required to break the contact and return to force zero, as shown in Figure 2.7(b).

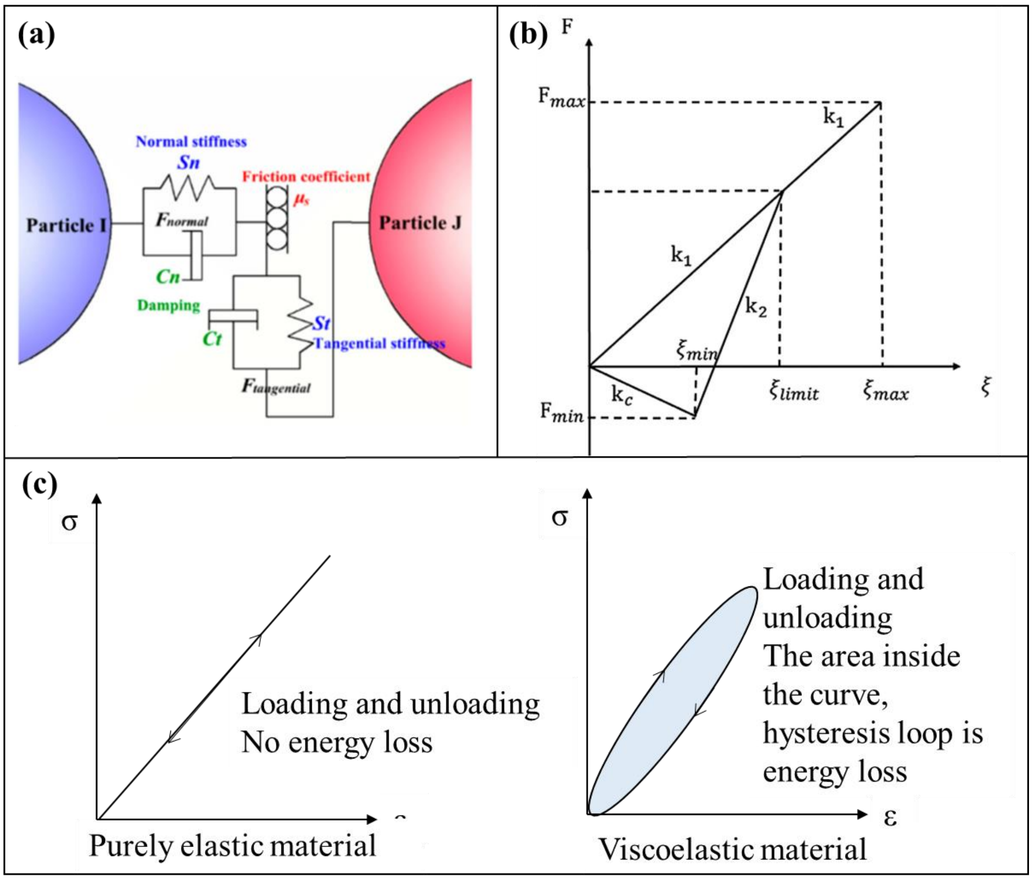

Figure 2.7. Types of DEM collision models: (a) The linear spring-dashpot model [86], (b) cohesion force model [85] and (c) visco-elastic model [83]. Different models can represent different kinds of inter-particle forces, such as cohesive and repulsive forces.

The advantage of the DEM is that it can account for a range of particle diameters, particle-particle collisions, mixing, heat transfer and chemical reactions within the waste bed as well as the mechanical and thermal loads on the conveying equipment, such as incinerators with moving grate design. However, it is very computationally intensive and difficult to get an accurate representation of particle shape, especially for MSW, which might not be pre-processed before being sent for disposal. The high computational costs are particularly obvious in simulations with many fine particles (of the order of mm), such as in fluidized beds [55]. Typically, the DEM timesteps are of the order of 10^{-6} s, resulting in ~20 s of actual time being simulated. This would likely be insufficient in representing the entire gasification process for fixed-bed gasifiers, where chemical and physical reactions can take several minutes to hours for a complete reduction of MSW to ash and liquid slag.

In order to reduce the computational time, the domain is divided using a separate Cartesian mesh. For each particle, only the neighbouring mesh cells containing particles will be checked for collisions and assumed to exert forces on it, as shown in Figure 2.8. Another strategy that has been used in the DEM to reduce the computational time is the concept of representative particles, also known as parcels or coarse-graining. Identical small particles are collected together into a single parcel, effectively reducing the number of particles to be tracked in the simulation and decreasing the computational time [87-89]. The parcels are treated as massive spheres, and the mass used in collisions is that of the entire parcel and scaled down to the particle. Coarse-graining, coupled with reduced particle stiffness ratio, has been found to be promising for large-scale dense particulate systems by a factor of up to 5000 [90]. Hence, the modelling approach was developed along these directions.

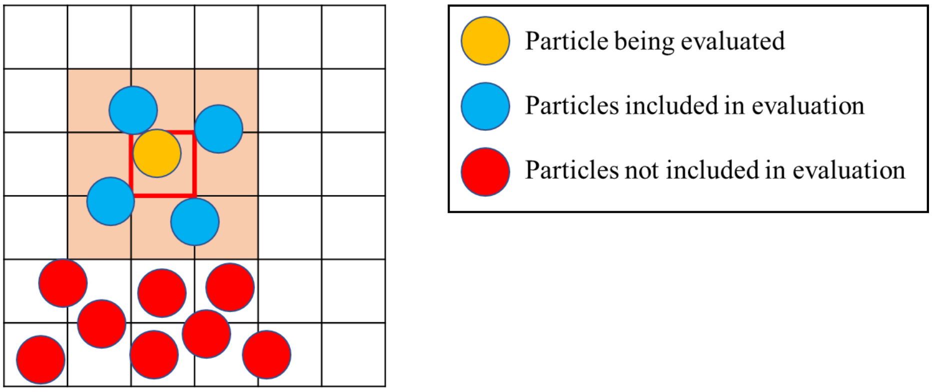

Figure 2.8. Forces evaluation on particles in neighbouring cells [78], to determine if collision occurs between neighbouring particles.

The computational requirement on the mesh-particle size ratio is very restrictive in CFD-DEM. The ratio needs to be sufficiently large in order to prevent the solid fraction from filling the fluid cell completely. At the same time, the ratio cannot be too large, otherwise the local flows around the particles cannot be accurately simulated [91]. However, the diameter of the embedded particles reduces during the melting process at different rates depending on their materials and locations within the reactor, which would naturally lead to a wide distribution of the mesh-particle ratio over the simulation time beyond the required range. In the literature, a few methods had been developed to address the mesh-particle ratio challenge, including dynamic meshing [74], coarse-graining [88], porous spheres [91], and sub-grid models for the flow around the smaller particles [52, 76]. Yin et al. [92] developed the Two-Fluid Model (TFM)-DEM method to simulate biomass gasification in a packed bed, with a large size difference between the biomass fuel and bed particles which were ~10 times smaller. DEM was used to model the biomass fuel particle, and the densely packed bed material was simulated using the KTGF (a Eulerian approach). Overall, if the melting model could be modified such that its predictions were not significantly affected by the mesh-particle size ratio, larger mesh sizes could be used. This would greatly reduce the simulation runtime and make it more applicable for larger reactors.

Given the application of simulating melting and liquid flow in a gasifier, where many particles of different compositions, sizes and melting rates are involved, the CFD-DEM approach was deemed to be the most suitable. This would allow the particles to be tracked individually and have their own unique temperatures, size and melting rates. Hence, it was even more important to prioritize the issue of high computational costs caused by the use of fine meshes and high number of particles and ensure that the developed melting model could be adapted to reduce computational costs.

2.3.2 Phase-change modelling

2.3.2.1 Softening and melting models

The simulation of the softening process has attracted much interest in recent years due to the engineering significance, such as in blast furnaces to model the cohesive zone and change in permeability due to the softening of the metal ore [93-95]. During the softening process, particles are more malleable and can fuse together, leading to a decrease in porosity and increase in pressure drop across the packed bed. A significant increase in pressure drop can disrupt the liquid tapping process if the system is not properly designed [96]. Experimental studies from Ohno et al. [97] used CT scanning to analyse the softening and melting behaviour of slag particles in a packed bed of graphite particles. The interaction forces, including the gravitational force, surface tension, drag force from the convective fluid, and resistance from porous media, determine if the softened particle stays in the cohesive layer or flows through the bed [98]. Some CFD-DEM models attempt to replicate these behaviours through the modification of the Young's modulus to represent the softening and melting processes of ore in a blast furnace [95, 99]. Others used the inclusion of cohesive forces among neighbouring particles [100]. Baniasadi et al. [101, 102] developed an eXtended Discrete Element Method (XDEM) to consider the temperature distribution within the individual particles, and developed a general approach for heat and mass transfer in packed beds, but did not consider the softening process in their model.

As of now, there have been several melting models proposed in the literature. One of the most popular Euler-Euler approaches to represent the softening and melting is the enthalpy-porosity method, whereby the transition region between the solid and fluid phases is represented by a "mushy" region. Within the "mushy" region, a momentum sink is applied based on the liquid volume fraction to restrict the liquid flow velocities [103]. The enthalpy-porosity method is particularly useful in capturing the liquid-solid interface of the melting objects as well as their shape deformation and associated stresses on the wall surfaces. Feng et al. [104] utilised the method to model the impingement of slag particles on a wall, subsequent spreading and solidification of the droplets, as well as impact of the shear stresses on the wall surface. Hummel et al. [47] modified this method for unconstrained melting within a capsule. Their results showed that the temperature distribution on the capsule wall is non-uniform during the melting process. Similarly, the flow distribution through a packed bed could affect the melting rate of the particles within the bed, which then modifies its porosity and permeability and influences the flow in return [105]. However, with the Eulerian-Eulerian approach being macroscopic, only the average properties of the fluid-filled packed bed can be predicted using this method [106]. In addition, since the collisions of individual particles and their size changes are not modelled directly, the predictions on the melting rate and bed packing might not be very accurate.

In almost all these cases, the solid and liquid phases are further combined as an overall single phase using the VOF method, whereby the flow properties, such as density and viscosity are volume-averaged, affecting the shared resultant velocity field. The VOF method is useful when there is a clear and observable liquid-solid interface, such as the melting of phase change material within capsules [107, 108]. However, VOF is unsatisfactory in situations where there are large differences in the behaviour of individual phases, as this could lead to significant irregularities especially around the fluid-solid interface, such as packed beds. Additionally, the existing momentum sink term applied on the single solid-liquid phase is inadequate to represent three-phase flows as it assumes the porosity is equal to the liquid fraction. Most recently, Celik et al. [98] developed a hybrid three-phase CFD-DEM approach, using discrete particles for the solid phase and the VOF method to represent the composite fluid (gas and liquid) phase. Their effort is the most advanced so far and to the best of our knowledge, there is currently no model that can track the three-phase flow with the movement of liquid phase considered independently and with simultaneous melting from solid to liquid phase. In other words, the effects of the subsequent liquid flow through the packed bed have been typically neglected, which is a major shortcoming in engineering applications where the liquid flow may clog the packed bed or modify the rate of the reactions inside the bed.

2.3.2.2 Slag formation and modelling

The high temperatures and pressures in gasification convert most of the non-volatile metals, mineral compounds, and residual char/ash into slag, an inert material, instead of the fly ash as generated from incineration. To counter the two main issues in slagging gasification as mentioned in Section 2.2, many numerical tools have been employed to predict the slagging behaviour. The fate and transport of ash particles and deposition rate has been correlated to gas flow fields, particle sizes and densities, and physical properties of the particles and walls [109-111]. The phenomenon of particle capture by the walls is thoroughly investigated especially in entrained-flow and fluidized bed gasifiers where the particles are very fine. In order to characterize the wall slag layer, the ash composition and temperature must be known [112]. To simplify the model, it is commonly assumed that the temperature of the slag is above the ash fusion temperature, so the slag is only in liquid form and does not re-solidify.

Chen et al. [113] developed a 2D slag model to simulate this liquid slag layer on the reactor walls during the steady state. Submodels were also created to calculate the rate of particle deposition, as well as the burning of particles on the wall. Subsequently, they developed a 3D slag flow model for coal gasification, by simulating the ash and char particles, attaching them to the walls, and subsequently “dissolving” them into the slag layer [114]. The model couples the VOF (Eulerian) with the DPM (Lagrangian) approach, and includes the particle’s mass, momentum and sensible heat into the slag phase via source terms. The forces on the particles are only drag and gravity forces. Thus, the model is a two-way coupling, and the particles are not assumed to affect each other. Figure 2.9(a) shows the interactions between the char particles and the slag layer [115]. The particles can rebound or be captured upon collision with the slag layer, where they would continue burning at a slower rate. Li et al. [111] examined the particle morphology. They found that at the critical carbon conversion, the molten minerals are exposed on the particle surface, increasing the particle stickiness. Before the particle transits from char to slag, it has a much lower stickiness as carbon is not sticky. During the transition, the particle stickiness and probability of deposition can be determined from the degree of exposure of the molten minerals on the particle surface, as illustrated in Figure 2.9(b) [111]. Thus, the carbon conversion could be an important parameter for the particle capture model.

In order to develop the slag model for the refractory walls, the particle capture criteria must be first determined. Upon contact with the slag layer, the char particles will either be captured or reflected, and the criteria can depend on the char conversion, particle and wall temperature, probability of collision, or particle kinetic energy [115-117]. An example is the modelling of particles and wall as sticky or non-sticky, then using those properties to determine if the particles are captured, as shown in Table 2.1 [115]. Walls are deemed to be sticky if the temperature is higher than a critical ash temperature, dependent on slag composition; particles are sticky if they meet the criteria for temperature and char conversion. For collisions where only the wall or the particle is sticky, the trapping of the particle depends on the particle Weber number, We. Although the slag layer does not impact the heat flux and wall temperature significantly, the study recommended to increase the wall temperatures to reduce the slag viscosity and improve slag discharge.

Table 2.1. Particle capture criteria [115].

	Sticky particle		*Non-sticky particle*	
	$We < We_{cr}$	$We > We_{cr}$	$We < We_{cr}$	$We > We_{cr}$
Sticky wall	Slagging	Slagging	Slagging	Reflect
Non-sticky wall	Fouling	Reflect	Reflect	Reflect

On the issue of blockage and clogging of the tapping point, there are also studies which aim to mitigate this issue by modelling and studying the drainage from the tap-hole. Olsen et al. [96] used a reduced order mathematical model to predict that tapping rates were significantly affected by conditions in the packed bed near the tap-hole, how the particles are arranged, particle size, and pressure drop across the bed. They found the results to be comparable with CFD simulations without porous media present, but due to computational costs, did not run simulations with porous media. This implied that with the increased detail of CFD modelling, it would be useful if there was a model to compare the results of liquid flow through the packed bed and tapping rates.

Despite extensive research into the formation of slag layer on the walls, slag formation within fixed-bed gasifiers is not commonly modelled due to its complex chemical composition and multiphase nature. Zhang et al. [106] used the Eulerian multiphase model for plasma gasification in a fixed-bed. In this study, the slag formation was represented by heat and mass transfer by setting energy and mass sinks in the solid phase, and energy loss in the gas phase.

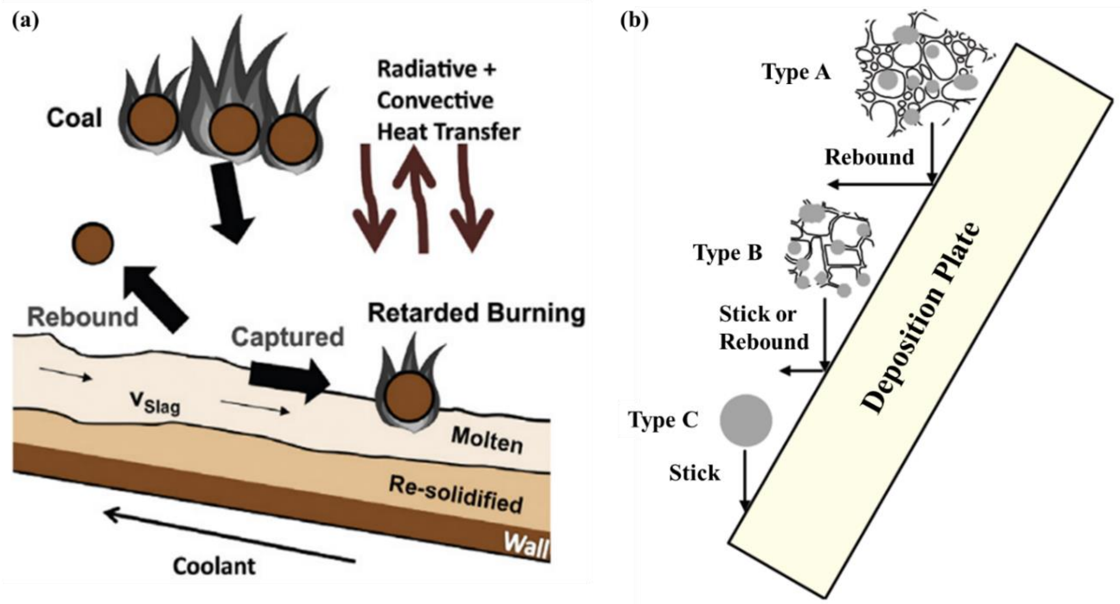

Figure 2.9. (a) Char capture process and slag layer [115]; (b) Particle fates upon impaction - A: Particle with enclosed minerals; B: Particle with partially exposed minerals; C: Slag particle [111].

Additionally, the motion of the slag was not modelled in detail and assumed not to affect the bed, which might not be necessarily true.

There is a lack of studies which address the melting of ash particles within the bed at present, as in the case for fixed or fluidized bed gasifiers. It is noted that most of the existing studies were based on coal and biomass gasification rather than MSW, which has a different composition and possibly differs in slagging behaviour. Furthermore, the literature typically focuses on small ash or char particles that are carried up by the air flow and captured on the wall, and not the melting of the larger particles in the bed that would have particle-particle interactions. Thus, further improvement is needed using the DEM to simulate the slag formation and melting process.

In summary, the current models in present studies are insufficient in terms of modelling melting in packed beds, especially for the enthalpy-porosity method which does not account for particle collisions and size changes. There are also limited studies for modelling the melting of MSW ash and slag flow in fixed or fluidized bed gasifiers, which is important for the identification of clogging points, and the visualization of slagging behaviour. The implementation of CD-MELT will attempt to address these issues through the use of CFD-DEM, and the user-defined functions (UDF) for the melting of solid particles.

Chapter 3. Methodology

3.1 Overview

This chapter describes the numerical model used for the simulations conducted, coupled with the commercial software Ansys® FLUENT Release 20.2 [78]. Throughout the studies, the Euler-Lagrange (CFD-DEM) model has been chosen as it allows for a higher accuracy, especially for the waste bed region as it includes the particle-particle interactions, as well as two-way coupling with the continuous phase. The Euler-Lagrange approach can also offer more accurate depictions of the chemical reactions as well as heat and mass transfer, as each particle's reaction is modelled individually. In cases where the particles are densely packed, the DEM collision model is used to account for the particle interactions.

The formulation of the melting model used in CD-MELT is explained in detail here, along with the procedure and considerations for the determination of the interphase momentum coefficients and drag force. First, the general conservation equations for both two and three-phase flows will be presented, then the development of the CD-MELT melting model from isothermal melting to non-isothermal melting. The challenges faced when developing the melting model are also discussed in detail.

3.2 General conservation equations

The CFD-DEM method developed in this work follows the Eulerian-Lagrangian approach which represents the fluid phase(s) as continuum(s) and the solid phase as individual particles. Each solid, liquid or gas phase is represented by its own numerical model and set of governing equations; hence, there are two models representing the two-phase flow in Chapter 4, and three models representing the three-phase flows in Chapters 5 and 6. The phases are coupled through the relevant source terms as well as interaction forces on a cell volume or particle basis. In CD-MELT, it is assumed that: (i) the solid particle density remains constant as it is melting; (ii) the shape of the particles is assumed to be spherical; (iii) the temperature is uniform within each particle; (iv) there are no chemical reactions during melting (with the exception of combustion-melting in Chapter 6); and for Chapter 4, (v) when the solid melts, it is instantaneously mixed with the surrounding liquid, resulting in negligible heat transfer and temperature change of the surrounding liquid. Assumption (v) only holds if the molten solid and surrounding liquid are of the same element, otherwise, it is not considered a two-phase flow and no instantaneous mixing occurs.

For the three-phase flows represented in Chapters 5 and 6, there are additional assumptions: (i) drag is the only interaction force between each pair of phases; in other words the inertial accelerations are negligible which are generally valid in packed beds, (ii) heat transfer only occurs between primary fluid-solid phases, and primary fluid-liquid phases, but not liquid-solid phases; this assumption limits the analysis to a shallow packed bed with negligible thermal gradient, (iii) mass transfer only occurs from the solid to the liquid phase, i.e., there is no re-solidification or subsequent vaporization of the molten liquid phase during the melting, (iv) the particles can undergo heating and melting at the same time so that the cross-sectional variation in the packed bed can be taken into account, and (v) the softening process before melting is not accounted for in the model. The assumptions listed might affect the CD-MELT model in terms of lower accuracy in melting rate prediction. For example, the spherical particle assumption might predict a lower melting rate than actual, as the surface area of the particle increases with an irregularly-shaped particle. On the other hand, the uniform temperature assumption might lead to a higher predicted melting rate than actual as more time might be required for heat to be conducted throughout the particle before it reaches melting temperature. However, the extent of the impact would depend on the size of the particles, as well as the thickness of the packed bed. In general, the smaller the particles, the lower the impact should be on the discrepancy between CD-MELT's predictions and actual melting rates.

3.2.1 Fluid-phase equations

In the fluid phase, the conservation equations for mass, momentum, and energy are solved for each cell volume. The hybrid Euler-Lagrange DDPM technique [70, 78, 118, 119] is used to account for the significant volume fraction of the solid phase within the packed bed, leading to the modifications of the mass and momentum equations for the fluid phase. Additionally, the governing equations for the fluid phases are slightly different, depending on if there are chemical reactions, and whether it is two-phase or three-phase flow. These conservative equations are expressed as follows.

For the two-phase flows in Chapter 4, where the solid phase melts directly and mixes instantaneously with the liquid phase:

Continuity equation:

$$\frac{\partial}{\partial t}(\alpha_{\mathrm{f}}\rho_{\mathrm{f}}) + \nabla \cdot (\alpha_{\mathrm{f}}\rho_{\mathrm{f}}\vec{v}_{\mathrm{f}}) = S_{\mathrm{mass}} \tag{1}$$

Momentum equation:

$$\frac{\partial}{\partial t}(\alpha_\mathrm{f}\rho_\mathrm{f}\vec{v}_\mathrm{f}) + \nabla\cdot(\alpha_\mathrm{f}\rho_\mathrm{f}\vec{v}_\mathrm{f}\vec{v}_\mathrm{f}) \\ = -\alpha_\mathrm{f}\nabla p + \nabla\cdot(\overline{\overline{\tau}}_\mathrm{f}) + \alpha_\mathrm{f}\rho_\mathrm{f}\vec{g} + K_\mathrm{DPM}(\vec{v}_\mathrm{p} - \vec{v}_\mathrm{f}) + S_\mathrm{mass}\vec{v}_\mathrm{f} \tag{2}$$

where the subscripts, f and p, refer to the fluid phase and discrete particle, respectively, α is the phase volume fraction, ρ is the density, $\vec{v}$ is the velocity vector, p is the pressure, $\overline{\overline{\tau}}_f$ is the fluid viscous stress tensor, $\vec{g}$ is the gravitational acceleration vector, and K_DPM is the particle-averaged momentum exchange coefficient [120]. S_mass is the volumetric mass source term from the discrete phase defined in Section 3.3.1, and is equal to zero, except when the solid phase undergoes melting. Here, we note that the drag force is a major contributor to the momentum exchange between the fluid and solid phases especially in packed beds [121].

The energy equation can be expressed as:

$$\frac{\partial(\alpha_\mathrm{f}\rho_\mathrm{f}h_\mathrm{f})}{\partial t} + \nabla\cdot(\alpha_\mathrm{f}\rho_\mathrm{f}h_\mathrm{f}\vec{v}_\mathrm{f}) = \alpha_\mathrm{f}\frac{dp_\mathrm{f}}{dt} + \overline{\overline{\tau}}_\mathrm{f} : \nabla\vec{v}_\mathrm{f} - \nabla\cdot\overrightarrow{q_\mathrm{f}} + Q_\mathrm{pf} + S_\mathrm{heat} \tag{3}$$

with the fluid enthalpy h_f as:

$$h_\mathrm{f} = \int_{T_\mathrm{ref}}^{T} c_\mathrm{p,f}\,dT \tag{4}$$

where $\overrightarrow{q_\mathrm{f}}$ is the heat flux vector, $c_\mathrm{p,f}$ is the specific heat of the fluid at constant pressure, T_ref is the reference temperature of 298.15 K, and S_heat is the volumetric source term representing the latent heat absorbed during the melting process and the enthalpy of the melted fluid at the melting temperature (S_heat =

0 when the particles are not melting). Q_{pf} is the heat exchange between the particles and fluid and is calculated as the change in thermal energy of the particles:

$$Q_{\mathrm{pf}} = m_{\mathrm{p,0}} \int_{T_{\mathrm{ref}}}^{T_{\mathrm{p,0}}} c_{\mathrm{p,p}} dT - m_{\mathrm{p}} \int_{T_{\mathrm{ref}}}^{T_{\mathrm{p}}} c_{\mathrm{p,p}} dT \tag{5}$$

where $m_{\mathrm{p,0}}$ and $T_{\mathrm{p,0}}$ represent the mass and temperature of the particle at the beginning of each timestep respectively, and $c_{\mathrm{p,p}}$ is the specific heat of the particle at constant pressure.

For the three-phase flows in Chapters 5 and 6, the liquid phase conservation equations are identical. For Chapter 5, the gas phase is represented by a single gas, while in Chapter 6, it is comprised of a gas mixture with chemical reactions and requires additional species transport equations to track the local mass fraction of each species. Hence, Eq. (7) and the terms R_{pg} in Eq. (6), $-\nabla \cdot \sum_i h_{i,\mathrm{g}} \vec{J}_i$ in Eq. (11) are present only when chemical reactions are included.

Primary phase (Gas):

Continuity:

$$\frac{\partial}{\partial t}\left(\alpha_{\mathrm{g}}\rho_{\mathrm{g}}\right) + \nabla \cdot \left(\alpha_{\mathrm{g}}\rho_{\mathrm{g}}\vec{v}_{\mathrm{g}}\right) = R_{pg} \tag{6}$$

Species transport equation for the gas mixture in Chapter 6 only:

$$\frac{\partial}{\partial t}\left(\rho_{\mathrm{g}} Y_i\right) + \nabla \cdot \left(\rho_{\mathrm{g}}\vec{v}_{\mathrm{g}} Y_i\right) = -\nabla \cdot \vec{J}_i + R_i \tag{7}$$

Momentum equation:

$$\frac{\partial}{\partial t}\left(\alpha_{\mathrm{g}}\rho_{\mathrm{g}}\vec{v}_{\mathrm{g}}\right)+\nabla\cdot\left(\alpha_{\mathrm{g}}\rho_{\mathrm{g}}\vec{v}_{\mathrm{g}}\vec{v}_{\mathrm{g}}\right)$$
$$=-\alpha_{\mathrm{g}}\nabla p+\nabla\cdot\left(\bar{\bar{\tau}}_{\mathrm{g}}\right)+\alpha_{\mathrm{g}}\rho_{\mathrm{g}}\vec{g}+K_{\mathrm{pg}}\left(\vec{v}_{\mathrm{p}}-\vec{v}_{\mathrm{g}}\right)+\ K_{\mathrm{lg}}\left(\vec{v}_{\mathrm{l}}-\vec{v}_{\mathrm{g}}\right) \qquad (8)$$

Secondary phase (Liquid):

Continuity equation:

$$\frac{\partial}{\partial t}(\alpha_{\mathrm{l}}\rho_{\mathrm{l}})+\nabla\cdot(\alpha_{\mathrm{l}}\rho_{\mathrm{l}}\vec{v}_{\mathrm{l}})=S_{\mathrm{mass}} \qquad (9)$$

Momentum equation:

$$\frac{\partial}{\partial t}(\alpha_{\mathrm{l}}\rho_{\mathrm{l}}\vec{v}_{\mathrm{l}})+\nabla\cdot(\alpha_{\mathrm{l}}\rho_{\mathrm{l}}\vec{v}_{\mathrm{l}}\vec{v}_{\mathrm{l}})$$
$$=-\alpha_{\mathrm{l}}\nabla p+\nabla\cdot(\bar{\bar{\tau}}_{\mathrm{l}})+\ \alpha_{\mathrm{l}}\rho_{\mathrm{l}}\vec{g}+K_{\mathrm{gl}}\left(\vec{v}_{\mathrm{g}}-\vec{v}_{\mathrm{l}}\right)+K_{\mathrm{pl}}\left(\vec{v}_{\mathrm{p}}-\vec{v}_{\mathrm{l}}\right)+S_{mass}\vec{v}_{\mathrm{p}} \qquad (10)$$

where the subscripts, g, l and p, refer to the gas, liquid (molten solid) and discrete solid particle, respectively, α is the phase volume fraction, ρ is the density, $\vec{v}$ is the velocity vector, R_{pg} is the mass added to gas phase as a result of particle surface reactions such as evaporation, devolatilization and combustion (only active in Chapter 6 simulations), R_i is the net mass added to the i^{th} species in the gas mixture via chemical or physical reactions, p is the pressure, $\bar{\bar{\tau}}$ is the fluid viscous stress tensor, $\vec{g}$ is the gravitational acceleration vector, K_{pg} is the particle-averaged momentum exchange coefficient [120], and $K_{\mathrm{lg}}=K_{\mathrm{gl}}$ is the gas-liquid momentum exchange coefficient for the drag force. S_{mass} is the volumetric mass source term from the solid to liquid phase defined in Section 3.3.2 and is equal to zero except when the solid phase undergoes melting. The volume fraction of the three phases in each cell sum to unity.

The energy equation for the primary phase can be expressed as:

$$\frac{\partial\left(\alpha_{\mathrm{g}}\rho_{\mathrm{g}}h_{\mathrm{g}}\right)}{\partial t}+\nabla\cdot\left(\alpha_{\mathrm{g}}\rho_{\mathrm{g}}h_{\mathrm{g}}\vec{v}_{\mathrm{g}}\right)$$
$$=\alpha_{\mathrm{g}}\frac{dp_{\mathrm{g}}}{dt}+\bar{\bar{\tau}}_{\mathrm{g}}:\nabla\vec{v}_{\mathrm{g}}-\nabla\cdot\vec{q}_{\mathrm{g}}-\nabla\cdot\sum_{i}h_{i,\mathrm{g}}\vec{J}_{i}+Q_{\mathrm{pg}}+Q_{\mathrm{lg}} \tag{11}$$

and the secondary phase as:

$$\frac{\partial(\alpha_{\mathrm{l}}\rho_{\mathrm{l}}h_{\mathrm{l}})}{\partial t}+\nabla\cdot(\alpha_{\mathrm{l}}\rho_{\mathrm{l}}h_{\mathrm{l}}\vec{v}_{\mathrm{l}})$$
$$=\alpha_{\mathrm{l}}\frac{dp_{\mathrm{l}}}{dt}+\bar{\bar{\tau}}_{\mathrm{l}}:\nabla\vec{v}_{\mathrm{l}}-\nabla\cdot\vec{q_{\mathrm{l}}}+Q_{\mathrm{gl}}+S_{\mathrm{mass}}(h_{\mathrm{melt}}-h_{\mathrm{ref}}) \tag{12}$$

with the fluid enthalpy h_{g} (or h_{l} for liquid phase) as:

$$h_{\mathrm{g}}=\int_{T_{\mathrm{ref}}}^{T}c_{\mathrm{p,f}}\,dT \tag{13}$$

where $\vec{q}$ is the heat flux vector, $c_{\mathrm{p,f}}$ is the specific heat of the fluid at constant pressure, Q_{pg} and Q_{lg} $(=-Q_{\mathrm{gl}})$ are the terms representing the heat transfer between each corresponding pair of phases within each cell volume and T_{ref} is the reference temperature of 298.15 K. The determination of these interphase momentum and heat exchange coefficients are further elaborated in Sections 3.4 and 3.5 respectively.

Flows with high Reynolds number are turbulent. Their characteristics are highly unsteady, rapid velocity fluctuations, and improved mixing and diffusion. Due to its chaotic nature, there have been various CFD approaches developed to simulate the turbulent flow. The most exact approach is the approach of Direct Numerical Simulation (DNS), followed by Large Eddy Simulation (LES), and lastly, the Reynolds-averaged Navier-Stokes (RANS) simulations with turbulent closures. The main differences in the three approaches are the computational time involved as well as the use of turbulence closures. DNS solves the Navier-Stokes equations without any averaging or approximation method; however, the simulation is limited by the processing speed and capacity, requiring small time-steps and grid size to model every fluid motion. Hence, it is not applicable for most industrial applications. For LES, it is conducted by filtering the velocity field and solving for the larger turbulent eddies in the domain. Lastly, for the RANS approach, flow variables, such as velocity, in the Navier-Stokes equations are separated into the mean (time-averaged) and the fluctuating components. The resulting conservation equations yield additional terms that represent the effects of turbulence, particularly the Reynolds stresses. In order to close the equations, these Reynolds stresses must be modelled through turbulence closures. For the purpose of this study, the RANS models are considered to be sufficiently accurate to study the processes during combustion and gasification.

One of the most common turbulence closures used in engineering is the standard $k - \varepsilon$ closure, first developed by Launder and Spalding [122]. Two separate transport equations are set up for turbulence kinetic energy (k) and dissipation rate (ε). In this study, the RNG k-ε turbulence closure, a modification of the standard closure is used. This turbulence closure has the advantage of including effects from smaller length scales on turbulent diffusion, making it more reliable and accurate than the standard k-ε model [37]. The governing equations for this closure (in Cartesian form) for the transport of turbulence kinetic energy, k, and eddy dissipation rate, ε, are as follows [123]:

$$\frac{\partial}{\partial t}(\rho k) + \frac{\partial}{\partial x_i}(\rho k v_i) = \frac{\partial}{\partial x_j}\left[\alpha_k \mu_{\text{eff}} \frac{\partial k}{\partial x_j}\right] + G_k + G_b - \rho\varepsilon \qquad (14)$$

$$\frac{\partial}{\partial t}(\rho\varepsilon)+\frac{\partial}{\partial x_i}(\rho\varepsilon v_i)=\frac{\partial}{\partial x_j}\left[\alpha_\varepsilon\mu_{\mathrm{eff}}\frac{\partial\varepsilon}{\partial x_j}\right]+C_1\frac{\varepsilon}{k}(G_k+C_3G_b)-\rho C_2\frac{\varepsilon^2}{k} \tag{15}$$

where G_k and G_b are respectively the turbulence kinetic energy due to mean velocity gradients and buoyancy effects, μ_{eff} is the effective turbulent viscosity, α_k and α_ε are the inverse effective Prandtl numbers, and C_1, C_2, and C_3 are constants [78, 124].

3.2.2 Solid-phase equations

The DEM approach is based on the Newton's second law of motion, and the equations of motion are solved for each particle with the particle force balance as:

For two-phase flows:

$$m_{\mathrm{p}}\frac{d\vec{v}_{\mathrm{p}}}{dt}=m_{\mathrm{p}}\frac{\vec{v}_{\mathrm{f}}-\vec{v}_{\mathrm{p}}}{\tau_r}+m_{\mathrm{p}}\frac{\vec{g}(\rho_{\mathrm{p}}-\rho_{\mathrm{f}})}{\rho_{\mathrm{p}}}+\vec{F}_{\mathrm{coll}} \tag{16}$$

$$\frac{dx_{\mathrm{p}}}{dt}=\vec{v}_{\mathrm{p}} \tag{17}$$

For three-phase flows:

$$m_{\mathrm{p}}\frac{d\vec{v}_{\mathrm{p}}}{dt}=m_{\mathrm{p}}\frac{K_{\mathrm{gp}}(\vec{v}_{\mathrm{g}}-\vec{v}_{\mathrm{p}})}{\rho_{\mathrm{p}}}+m_{\mathrm{p}}\frac{K_{\mathrm{lp}}(\vec{v}_{\mathrm{l}}-\vec{v}_{\mathrm{p}})}{\rho_{\mathrm{p}}}+m_{\mathrm{p}}\frac{\vec{g}(\rho_{\mathrm{p}}-\rho_{\mathrm{g}})}{\rho_{\mathrm{p}}}+\vec{F}_{\mathrm{coll}} \tag{18}$$

$$\frac{dx_{\mathrm{p}}}{dt}=\vec{v}_{\mathrm{p}} \tag{19}$$

where m_{p} and x_{p} are the mass and position of each particle respectively, and the terms on the right hand side of Eqs. (16) and (18) represent the drag force(s) from the fluid phases, the sum of the gravitational and buoyancy forces, and the contact forces due to particle collisions. Initially, for the two-phase flow simulations, the spherical drag law was used [125]. For the three-phase flow simulations, the drag force terms from liquid and gas phases were both represented via the Gidaspow model [126]. The details for the formulation of the drag forces are given in Section 3.4. The equations for rotational movement of the particles are not solved for each particle as the particles are relatively large and there is negligible rotational movement within the packed bed. Rotational movement of particles is more significant for small particles with frequent collisions with the wall or other particles. Furthermore, the magnitude of the torque exerted by the air or liquid convection is not expected to be significant to the bed packing. Hence, the rotational motion is not a significant factor to be considered.

The DEM soft sphere model [81] accounts for the forces from the collision of particles which are included as the $\vec{F}_{\text{coll}}$ term in the particle force balance equation. These forces are assumed to be a function of the overlap between particles or with a boundary. The linear spring-dashpot model is used to represent the collision forces which are exerted normally ($\vec{F}_N$) and tangentially ($\vec{F}_T$) to the particle surface as [78]:

$$\vec{F}_{\text{coll}} = \vec{F}_N + \vec{F}_T \tag{20}$$

The normal contact force exerted on a particle by another particle or the boundary is calculated as:

$$\vec{F}_N = \big(K\delta + \gamma(\vec{v}_{12} \cdot \vec{e}_{12})\big)\vec{e}_{12} \tag{21}$$

where K is the spring constant, δ is the overlap during contact, γ is the damping coefficient, $\vec{v}_{12} = \vec{v}_2 - \vec{v}_1$ is the relative velocity, $\vec{e}_{12}$ is the unit vector in the normal direction between the particles or between the particle and the boundary. The particle overlap during collision is estimated to be:

$$\delta = \|x_2 - x_1\| - (r_1 + r_2) \tag{22}$$

The damping coefficient, which is analogous to the dashpot, is calculated as:

$$\gamma = -2\frac{m_{12} ln\eta}{t_{coll}} \tag{23}$$

where m_{12} is the reduced mass, and t_{coll} is the collision time as:

$$m_{12} = \frac{m_1 m_2}{m_1 + m_2} \tag{24}$$

$$t_{coll} = \sqrt{\frac{(\pi^2 + \ln^2 \eta) m_{12}}{K}} \tag{25}$$

The tangential contact force is calculated in CD-MELT via a Coulomb model:

$$\vec{F}_T = \mu_{fr} \vec{F}_N \tag{26}$$

where the friction coefficient, μ_{fr} is set at 0.3. We note that the direction of the tangential force is opposite to the relative tangential motion.

In Chapters 4 and 5, the simulated particles were assumed to be inert and did not undergo physical or chemical reactions other than melting. Hence, for such applications, the particle temperature was calculated and solved via the energy balance equation for each particle as:

For two-phase flows:

$$m_{\mathrm{p}} c_p \frac{dT_{\mathrm{p}}}{dt} = h_c A_{\mathrm{p}} \left(T_{\mathrm{f}} - T_{\mathrm{p}}\right) + \frac{dm_{\mathrm{p}}}{dt} h_m \tag{27}$$

and for three-phase flows:

$$m_{\mathrm{p}} c_p \frac{dT_{\mathrm{p}}}{dt} = h_c A_{\mathrm{p}} \left(T_{\mathrm{g}} - T_{\mathrm{p}}\right) + \frac{dm_{\mathrm{p}}}{dt} h_m \tag{28}$$

where the terms on the right-hand side of both equations refer to the energy exchanged with the continuous phase due to convection and latent heat of fusion (with melting particles). For applications in which the solids are inert, we assume that prior to melting, the particles undergo inert heating only, and the melting rate, $\frac{dm_{\mathrm{p}}}{dt}$, is zero before reaching the melting temperature (T_{m} for isothermal melting) or solidus temperature (T_{s} for non-isothermal melting). Here, the melting rate is defined as the change in the mass of the solid particle and is negative when the particle is undergoing melting.

For two-phase flows, the convective heat transfer coefficient, h_c, is calculated using the Ranz-Marshall correlation [127]:

$$h_c = \frac{k_{\mathrm{f}} Nu}{d_{\mathrm{p}}} \tag{29}$$

$$Nu = 2.0 + 0.6 Re_{\mathrm{p}}^{\frac{1}{2}} Pr_{\mathrm{f}}^{\frac{1}{3}} \tag{30}$$

where k_{f} is the fluid thermal conductivity and Pr_{f} is the fluid Prandtl number.

Re_p is the particle Reynolds number defined as:

$$Re_\mathrm{p} = \frac{\rho_\mathrm{f} d_\mathrm{p} \left| \vec{v}_\mathrm{p} - \vec{v}_\mathrm{f} \right|}{\mu_\mathrm{f}} \tag{31}$$

For three-phase flows, h_c is calculated in a similar way, albeit replacing fluid properties in Eqs. (29) to (31) with the gas properties.

Upon melting in two-phase flows, the following equation shall be applied which can be derived from Eq. (27) as:

$$\frac{dm_\mathrm{p}}{dt} h_m = -h_c A_\mathrm{p} \left(T_\mathrm{f} - T_\mathrm{p} \right) \tag{32}$$

where the temperature of the fluid, T_f, is replaced accordingly with the temperature of the gas, T_g, for three-phase flows and gas convection. In other words, the particle is assumed to undergo only phase change at the melting temperature, and the heat to melt the particle is gained through convection from the fluid. This heat gain and the enthalpy of the melted fluid is converted to the volumetric energy source term absorbed from the continuous phase, S_heat.

For applications where the particles are not inert, such as in Chapter 6 where prior to melting, they could undergo physical or chemical processes such as vaporization, devolatilization, and combustion, the particle energy balance equation changes based on the current particle law. At every DPM timestep, the particle law is implemented for each particle depending on its particle composition and temperature. Depending on the particle law, the Lagrangian equations for particle energy balance equations are solved for each particle at every DPM timestep as listed in Table 3.1, with no changes to the particle force balance equations.

Table 3.1. Particle laws and corresponding particle energy balance equation [78].

Particle Law(s)	Particle Energy Balance Equation	No.
Inert Heating	$m_{\mathrm{p}} c_{\mathrm{p}} \frac{dT_{\mathrm{p}}}{dt} = h_c A_{\mathrm{p}} (T_{\mathrm{g}} - T_{\mathrm{p}})$	(33)
Vaporization	$m_{\mathrm{p}} c_{\mathrm{p}} \frac{dT_{\mathrm{p}}}{dt} = h_c A_{\mathrm{p}} (T_{\mathrm{g}} - T_{\mathrm{p}}) + \frac{dm_{\mathrm{p}}}{dt} h_{vaporization}$	(34)
Devolatilization	$m_{\mathrm{p}} c_{\mathrm{p}} \frac{dT_{\mathrm{p}}}{dt} = h_c A_{\mathrm{p}} (T_{\mathrm{g}} - T_{\mathrm{p}}) + \frac{dm_{\mathrm{p}}}{dt} h_{devolatilization}$	(35)
Surface Reactions (Combustion/Pyrolysis)	$m_{\mathrm{p}} c_{\mathrm{p}} \frac{dT_{\mathrm{p}}}{dt} = h_c A_{\mathrm{p}} (T_{\mathrm{g}} - T_{\mathrm{p}}) - f_h \frac{dm_{\mathrm{p}}}{dt} H_{reac}$	(36)
Simultaneous Melting and Combustion	$m_{\mathrm{p}} c_{\mathrm{p}} \frac{dT_{\mathrm{p}}}{dt} = h_c A_{\mathrm{p}} (T_{\mathrm{g}} - T_{\mathrm{p}}) - f_h \frac{dm_{\mathrm{p}}}{dt} H_{reac} + \frac{dm_{\mathrm{p}}}{dt} h_m$	(37)
Melting	$m_{\mathrm{p}} c_{\mathrm{p}} \frac{dT_{\mathrm{p}}}{dt} = h_c A_{\mathrm{p}} (T_{\mathrm{g}} - T_{\mathrm{p}}) + \frac{dm_{\mathrm{p}}}{dt} h_m$	(38)

As described earlier, the solid phase is represented by the individual discrete particles, and the conservation equations are solved on a Lagrangian manner for each particle using the DEM. Depending on the characteristics of the individual particles, their melting behaviour can be distinctly different. In Chapter 5, to be described later, two types of particles, glass and wax, are both represented as the solid phase and have identical conservative equations for particle force balance and inter-particle collision. Their only difference lies in the particle energy balance and melting process for the wax particles, which are implemented by UDFs. The UDFs update the particle diameter and mass during melting and modify the source terms to the gas phase before coupling with the fluid flows. The molten solid is also added to the liquid phase with the relevant mass, momentum, and energy source terms. Conversely, the primary gas phase generates the interaction forces that act on the particles as they pass through the cell volume. The details of the UDFs will be described in Section 3.3.

3.2.3 Coupling and solution procedures

The simulations for CD-MELT are implemented in this study with the commercial CFD software, Ansys® Fluent, Release 20.2 [78] using the finite volume method, where the fluid domain is discretized into many cells. The pressure-velocity coupling in the fluid region is solved using the pressure-based Phase Coupled Semi-Implicit Method for Pressure Linked Equations (PC-SIMPLE) algorithm [128]. Relatively coarse hexahedral meshes are used to satisfy the assumption for the CFD-DEM governing equations which require a cell-to-particle size ratio of at least 1.63 [129].

A full CFD-DEM can extend to four-way coupling interactions, i.e. the fluid and particle phases interacting with each other (two-way coupling), as well as changes within the particle phase and also particle-particle interactions [101]. The fluid phases can be solved via the standard Eulerian approach over each cell volume considering the boundary conditions, while the solid phase can be tracked via the DEM for each particle as discussed above. Generally, the timestep needs to be sufficiently small to capture the flow and the movement of the particles within each cell volume. At the same time, a coarser mesh would allow for a larger timestep, reducing the total computational time. For the fluid phase, the timestep is restricted by the Courant-Friedrichs-Lewy (CFL) condition, which is a function of flow velocity, mesh size and timestep such that the CFL number is always less than 1. On the other hand, the DEM timestep should be smaller than the particle collision time, t_{coll} [81]. As a result, the timesteps for both fluid and discrete phases usually have different order of magnitudes depending on the flow/particles' velocities or the timescales of chemical processes.

The DEM timestep is typically much smaller than the CFD timestep. At each DEM timestep in CD-MELT, the position, velocity, temperature and size of each particle are calculated, accounting for collisions from other particles, drag and body forces from the fluid, and heat and mass transfer to and from the surrounding fluid. The source terms from the discrete phase to the fluid phase are then updated as the sum of the changes in mass, momentum and energy of the particles in each cell volume. The fluid phase is then solved considering the effects of the particle volume fraction, interaction forces and volumetric source terms. The flow field's temperature, pressure and velocity are then updated, and these changes in turn produce similar effects on the particles. The cycle repeats until the desired simulation time is reached.

Due to the discrepancy in fluid and DEM timesteps, care must be taken when coding UDFs for particles and fluids, which are executed at different times. For example, to track if the source terms were added correctly, the mass loss from melting was calculated for each particle during each DEM timestep, and saved to the user-defined memory (UDM) variable of the cell that the particle was located in. This term was then cumulated over the DEM timesteps to account for the mass losses from multiple particles. When the CFD timestep is reached, the mass in the UDM for each cell is converted and added to the volumetric mass source term for the liquid phase and reset to zero afterward. To ascertain mass conservation, the total mass source to the liquid phase can be summed over the domain and compared with the change in total mass of the solid and any mass outflows, with similar procedures being done for momentum and energy.

3.3 Development of CD-MELT melting model

The modified heat integration method is adopted in CD-MELT to calculate the latent heat absorbed and subsequent mass change of the particle [130], i.e. for every particle that increases to a temperature beyond the melting point (T_m), only a portion of the particle is assumed to undergo phase change. In the case for demonstrating isothermal melting of packed ice spheres filled with water under forced convection, instantaneous mixing is assumed, and the melted ice is added into the surrounding fluid within the timestep. However, for the case of non-isothermal melting in three-phase flow, the instantaneous mixing assumption is removed and heat transfer allowed to occur between gas and liquid. The full description and code of the UDFs are given in Appendix A.

3.3.1 Isothermal melting

The portion of melted liquid is represented in CD-MELT by a mass loss fraction, β, which ranges from 0 (the initial mass of the particle, i.e. no mass loss) to 1 (the particle has completely melted). This representation in CD-MELT is unique and differs from other existing models. In some way, it is analogous to the mushy zone mentioned in the literature [49, 131], however CD-MELT utilises the mass fraction and not the volume fraction used in these studies. In doing so, we aim to capture the heat transfer for the melting which is dominantly mass-dependent in a more accurate manner, rather than the shape and motion of the packed media. Moreover, if desired, β could also be used in CD-MELT as a particle-specific variable to modify other particle properties, such as the heat capacity, spring constant and heat transfer coefficient, which could change during the melting process. We find that this representation is particularly effective for particles which are composed of different materials or have thermal properties that change with size.

An overview of the melting model in CD-MELT is shown in Figure 3.1. A UDF (**dpm_switch**) is included in CD-MELT to determine if the particle undergoes inert heating or melting based on the particle temperature. If the temperature is more or equal to T_m, the isothermal melting law (through another UDF (**meltinglaw**)) is then implemented as follows:

(i) obtain the new particle temperature, T_n assuming inert heating according to Eq. (27).

(ii) calculate the heat absorbed from convection within the particle timestep as follows:

$$Q = m_{\mathrm{p}} c_{\mathrm{p}} \Delta T \tag{39}$$

where ΔT is the temperature difference, i.e. $\Delta T = T_n - T_m$.

(iii) compute the mass change of the particle, based on Eq. (32):

$$\frac{dm_{\mathrm{p}}}{dt} = -\frac{Q}{h_m} \tag{40}$$

(iv) update the particle diameter based on the new mass, keeping density constant.

(v) calculate the mass loss fraction, $\beta = 1 - \frac{m_\mathrm{p}}{m_\mathrm{p,0}}$, where m_p is the current particle mass and $m_\mathrm{p,0}$ is the particle mass at the start of the melting process.

(vi) set the temperature of the particle back to T_m if Q is positive.

In summary, the equivalent amount of heat due to setting the temperature back to T_m is used to melt a part of the particle and change the mass. The volumetric latent heat absorbed with the liquid enthalpy is then added to the fluid phase as a heat sink, S_heat, and the mass change of the particle is added to the fluid phase as a mass source, S_mass, as well as a momentum source, $S_\mathrm{mass}\vec{v}_\mathrm{f}$ through a UDF (**particle_source**). When β is ≥ 0.95, the particle is removed from the flow, and the equivalent mass, momentum and energy source terms are added accordingly.

3.3.2 Non-isothermal melting

A modified heat integration method is adopted in CD-MELT to calculate the heat absorbed and mass change of the particle due to melting [130], i.e. for every particle that increases to a temperature beyond the solidus temperature (T_s), only a portion of the particle is assumed to undergo phase change. This portion is calculated via a unique particle-specific variable called particle enthalpy in CD-MELT, generated from the heat absorbed during convection from the gas phase. The heat absorbed from the gas and the enthalpy of the molten solid are then respectively converted to volumetric energy source terms Q_pg and $S_\mathrm{mass}(h_\mathrm{melt} - h_\mathrm{ref})$. This non-isothermal melting approach is implemented directly in CD-MELT.

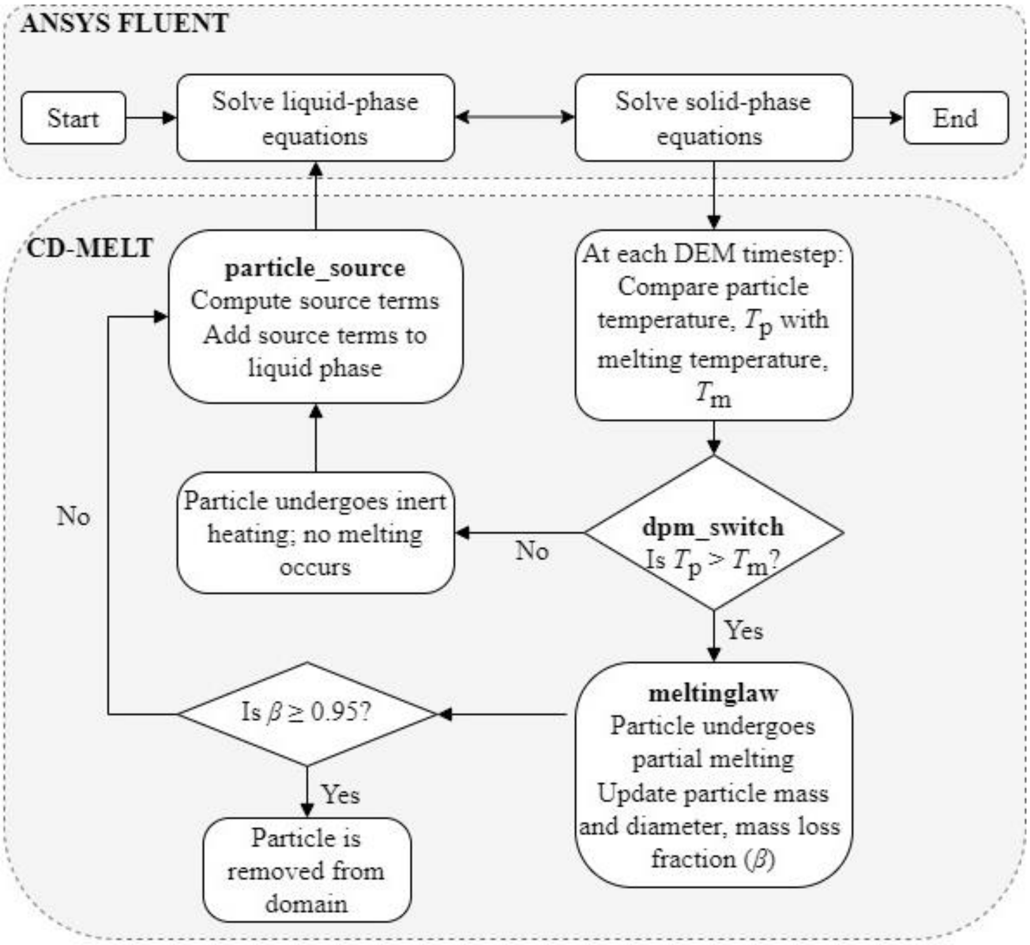

Figure 3.1. Implementation for two-phase flows and coupling of CD-MELT with ANSYS Fluent (UDFs in bold) for computing heat and mass transfer between solid and fluid phases during the melting process.

The numerical steps for the melting simulation are described in the following. CD-MELT has been formulated to incorporate both isothermal (for simplification or pure materials) and non-isothermal melting, based on the same governing equation of particle energy balance, Eq. (28). Once the temperature of the particle is above the solidus temperature, surface melting will occur and the melted liquid will detach from the solid and flow through the porous media in the liquid phase. During the melting, the particle diameter is assumed to undergo a linear decrease based on its temperature [99] within the solidus and liquidus temperature range. In CD-MELT's non-isothermal melting approach, the liquid phase is represented through an assembly of droplets.

For applications with reactive gas-solid flows, a simplified particle lifetime process is illustrated in Figure 3.2. The energy balance equation solved for each particle at each DEM timestep is based on its pre-determined particle law, and only one law can be used at a time. The switching of particle laws is implemented via a UDF (**dpm_switch**) based on the presence of liquid mass fraction, volatile fraction, char fraction, and particle temperature. The particle would then sequentially undergo vaporization, devolatilization, combustion and melting as its temperature increased. For particles without physical or chemical reactions, **dpm_switch** is only used to switch the particle law from inert heating to melting and vice versa. An overview of the melting model in CD-MELT and its coupling with the ANSYS® Fluent software is shown in Figure 3.3. Upon the first instance when the particle reaches the solidus temperature, T_{s}, its mass, diameter, heat capacity and density are recorded in a storage array unique to the particle. This array can be accessed where subsequently needed (relevant variables subscripted as p,0). The heat capacity and density were then assumed to be constant throughout the melting process and not weighted based on composition. The non-isothermal, non-reactive melting law (through the UDF (**meltinglaw**)) is then implemented for each particle as follows:

Step 1: Obtain the new particle temperature, T_{p} assuming inert heating according to Eq. (28).

Step 2: Calculate the heat absorbed from convection within the particle time step:

$$Q = m_{\mathrm{p}} c_{\mathrm{p}} \Delta T \tag{41}$$

where ΔT is the temperature difference, i.e. $\Delta T = T_{\mathrm{p}} - T_{\mathrm{p,i}}$. $T_{\mathrm{p,i}}$ is the particle temperature at the start of the time step.

Step 3: Add the heat absorbed to the particle enthalpy, h_{p}.

Step 4: Assume that the particle rises to the temperature T_{p}, its corresponding diameter and change in mass are then computed while keeping the density constant as follows:

$$d_{\mathrm{p}} = d_{\mathrm{p,0}} - d_{\mathrm{p,0}} \frac{T_{\mathrm{p}} - T_{\mathrm{s}}}{T_{\mathrm{l}} - T_{\mathrm{s}}} \tag{42}$$

$$\Delta m = \frac{\rho_{\mathrm{p}} \pi}{6} \left(d_{\mathrm{p}}^3 - d_{\mathrm{p,i}}^3 \right) \tag{43}$$

where $d_{\mathrm{p,0}}$ is the initial particle diameter at solidus temperature before any melting occurs (mass loss fraction, β = 0), $d_{\mathrm{p,i}}$ is the particle diameter at the start of the time step. T_{l} and T_{s} are the liquidus and solidus temperature respectively.

Step 5: Calculate the total enthalpy (sum of the latent heat of melting, $\Delta m h_m$, and sensible heat, Q) required to reach T_{p} and compare its magnitude with the particle enthalpy. If $h_{\mathrm{p}} \geq (\Delta m h_m + Q)$, then there is sufficient particle enthalpy and partial melting occurs. Particle temperature, diameter and mass are updated to the calculated values. Otherwise, no melting occurs, and the particle temperature, diameter and mass are reverted to the values at the start of the timestep.

Step 6: Calculate the mass loss fraction, $\beta = 1 - \frac{m_{\mathrm{p}}}{m_{\mathrm{p,0}}}$, where m_{p} is the current particle mass and $m_{\mathrm{p,0}}$ is the particle mass at the start of the melting process.

In summary, the energy absorbed from the surrounding gas via convection is used to melt a portion of the particle and raise its temperature simultaneously. The volumetric heat absorbed is then added to the gas phase as a heat sink, Q_{pg}. When melting occurs, the mass and heat transfer from the solid particle is added to the liquid phase via the mass source, S_{mass}, momentum source, $S_{\mathrm{mass}}\vec{v}_{\mathrm{f}}$ and enthalpy source, $S_{\mathrm{mass}}(h_{\mathrm{melt}} - h_{\mathrm{ref}})$. When the mass loss of the particle to melting exceeds 95% of its original mass (i.e., $\beta \geq 0.95$), the particle is removed, and the equivalent mass, momentum and energy source terms are added accordingly to the liquid phase to ascertain the conservation within the domain. We note however that combustion and melting can occur simultaneously, if char fraction is still present in the particle. In these cases, the process flow is slightly modified based on the condition if char fraction is present in the particle, and the full process is described in Appendix B. In other words, particles in the same region but with different compositions, sizes or temperatures can undergo vastly different processes. Given initial properties and composition (i.e., % moisture, VM, FC and ash) of the particles, CD-MELT can simulate individually the subsequent changes of these particles with different melting rates.

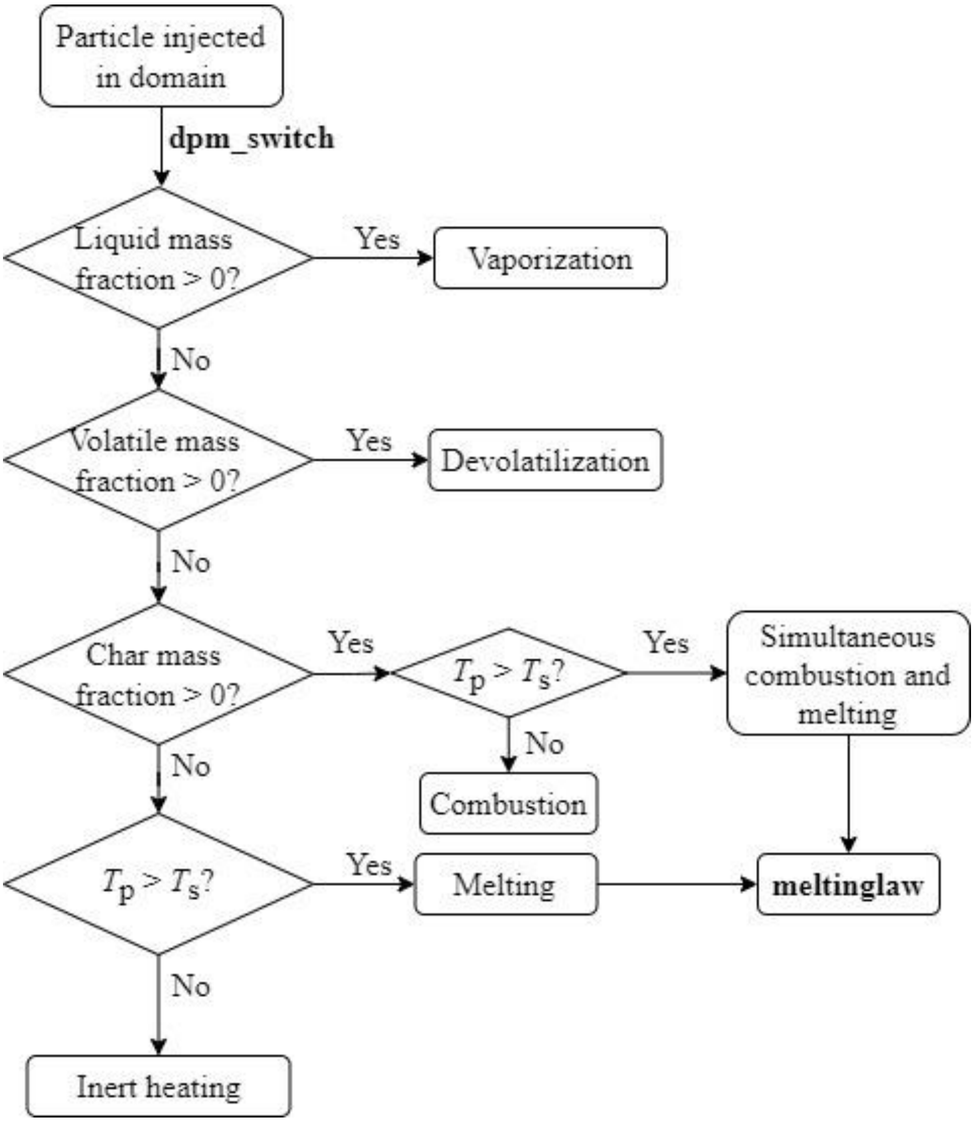

Figure 3.2. Simplified particle lifetime process implemented by UDF (**dpm_switch**). T_p is particle temperature, while T_s is the solidus temperature.

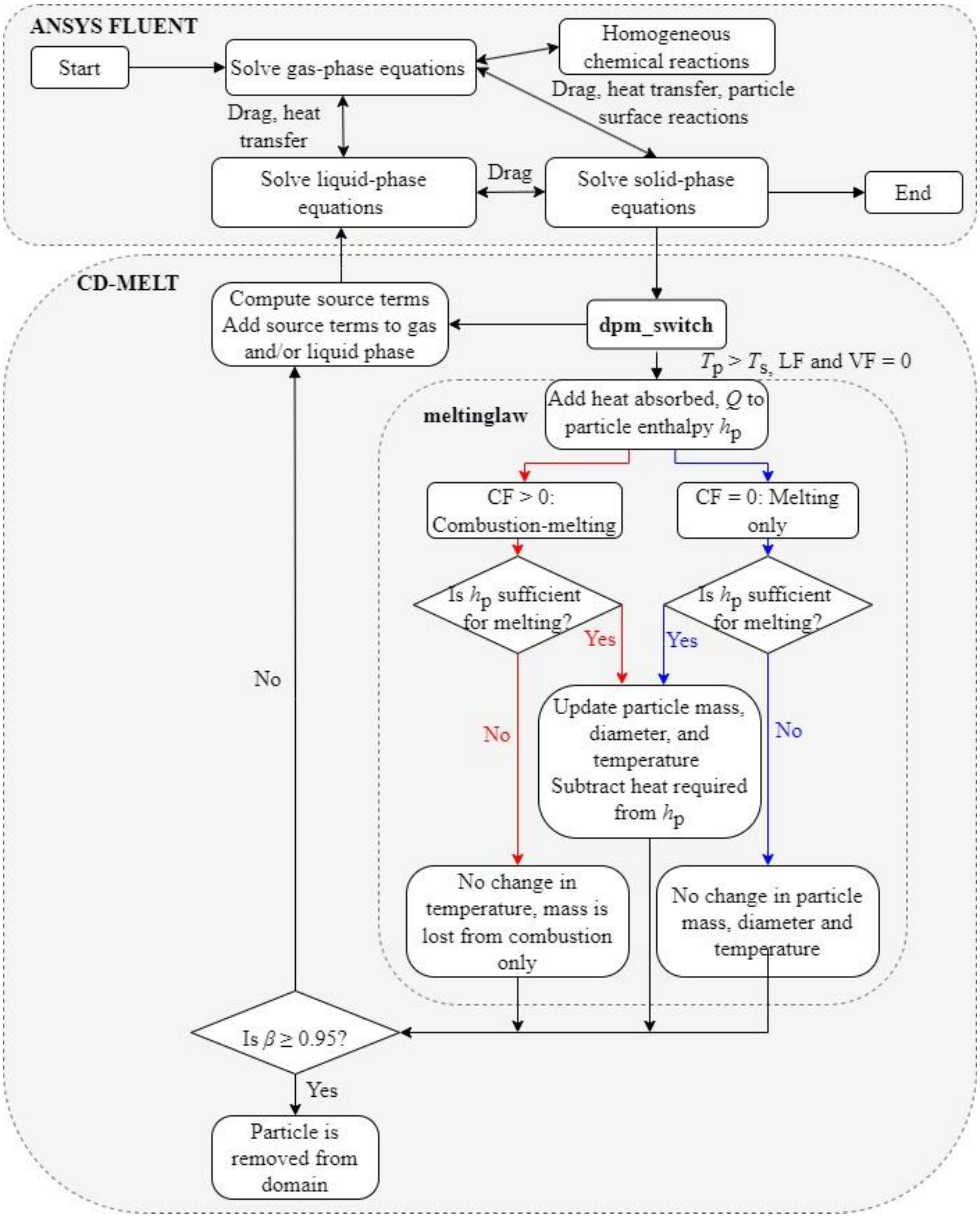

Figure 3.3. Implementation and coupling of CD-MELT with UDFs within the ANSYS Fluent software for computing heat and mass transfer for three-phase, non-isothermal melting processes.

3.3.3 Challenges of the melting model

Several challenges were encountered during the implementation of the combustion-melting model in Chapter 6. Prior to t = 5000 s, there were existing MSW and slag particles in the system. These particles did not undergo melting, only combustion and inert heating and were removed upon reaching liquidus temperature. However, the melting model requires the variable of the particle diameter when it first reaches solidus temperature. Hence, an on-demand UDF was written (**flag_particles**) and executed at t = 5000 s to flag all the particles that were above solidus temperature at the time, and these particles would not undergo the combustion-melting model but only undergo combustion or inert heating (if char fraction is equal to 0), and be removed upon reaching liquidus temperature.

There were also issues with determining the corrective source term for ANSYS Fluent. During the preliminary development for the non-isothermal melting model for Chapter 5, it was noted that a corrective source term was required due to the way the fluid was coupled with the particles in ANSYS Fluent. Mass and energy sources were computed during every DEM timestep based on the change in the mass and enthalpy of the particles, and added to the primary phase by default (programmed into the commercial software). This was acceptable in Chapter 4 for the simulation with two-phase flows where the solid was mixing directly with the primary phase (liquid) after melting, but not in Chapters 5 and 6, where the primary phase was gaseous and no mass transfer should have occurred between that gaseous phase and the solid phase. The energy transfer term was also incorrect. Hence, corrective source terms for mass and energy had to be introduced to modify the default source terms. Due to the low velocity of the particles involved, corrective momentum source terms were not included. The corrective source terms were formulated given information from the ANSYS theory guide [78]. However, there was difficulty in determining the formulation of the corrective source term for Chapter 6 as it was unclear how the char fraction of the particle factored into the equation, if at all. Numerical instabilities occurred after a certain point in the simulations and could not be resolved despite numerous attempts.

Challenges were also encountered when treating the melting and removal of the existing slag and MSW particles. Prior to t = 5000 s, the particles were removed once they reached liquidus temperature, and no liquid slag was added in their place. Initially, it was expected that the liquid slag could be added in when the particles were removed, as had been done with the previous studies. However, numerical instabilities were observed and the simulation could not proceed. It is plausible that this was due to a large volume of liquid phase being added at a single timestep, rendering the simulation unstable. Alternatively, it could also be due to the large energy sink from the gas phase within one timestep via the source term when accounting for melting of the particle. Hence, the results of liquid slag observed in Chapter 6 are only from the melting of the slag particles which were below solidus temperature at t = 5000 s, while the other particles were simply removed. If the melting model had been activated from t = 0 s rather than t = 5000 s, the liquid slag formation and distribution within the bed would be more accurate. Lastly, it was noted that when a particle is removed from the system, the enthalpy of the particle should be transferred entirely to the liquid phase, however, due to the nature of the specific heat capacity being composition and temperature dependent, the exact particle enthalpy is unknown. It is acknowledged that this led to the results being less reliable, nevertheless, some conclusions can be drawn for the two cases with and without slag recycling and are thus mentioned in Chapter 6.

3.4 Determination of interphase drag forces

3.4.1 Spherical drag law for two-phase flow

The representation of the drag force between phases has been developed over the duration of the research. In the preliminary simulations, when the two-phase flow of water through a packed bed of melting ice was considered, the focus was on simulating the isothermal melting process and not on the tracking of the liquid melt through the packed bed. Additionally, even without the assumption of instantaneous mixing, the flow velocity and density of the liquid melt through the packed bed was expected to be of similar magnitude as the warm water. Hence, the only drag force considered was the drag force between the warm water and the ice particles. The spherical drag law was used due to its simplicity.

τ_r represents the particle relaxation time which can be expressed as [132]:

$$\tau_r = \frac{\rho_\mathrm{p} d_\mathrm{p}^2}{18\mu_\mathrm{f}} \frac{24}{C_d Re_\mathrm{p}} \tag{44}$$

where d_p is the particle diameter, C_d is the drag coefficient, μ_f is the dynamic viscosity of the fluid, and Re_p is the particle Reynolds number, defined as:

$$Re_\mathrm{p} = \frac{\rho_\mathrm{f} d_\mathrm{p} \left| \vec{v}_\mathrm{p} - \vec{v}_\mathrm{f} \right|}{\mu_\mathrm{f}} \tag{45}$$

C_d is represented using the relationship for smooth particles from Morsi and Alexander [125]:

$$C_d = a_1 + \frac{a_2}{Re_\mathrm{p}} + \frac{a_3}{{Re_\mathrm{p}}^2} \tag{46}$$

where a_1, a_2 and a_3 are constants as shown in Table 3.2, depending on the Reynolds number.

Table 3.2. Parameters for drag coefficient [125].

$\boldsymbol{a_1}$	$\boldsymbol{a_2}$	$\boldsymbol{a_3}$	**Reynolds number**
0	24	0	*Re* < 0.1
3.69	22.73	0.0903	0.1 < *Re* < 1
1.222	29.1667	−3.8889	1 < *Re* < 10
0.6167	46.5	−116.67	10 < *Re* < 100
0.3644	98.33	−2778	100 < *Re* < 1000
0.357	148.62	−47500	1000 < *Re* < 5000
0.46	−490.546	578700	5000 < *Re* < 10000
0.5191	−1662.5	5416700	*Re* ≥ 10000

3.4.2 Gidaspow drag model for three-phase flow

For the three-phase flow simulations, the primary coupling among the three phases in CD-MELT is through the interaction forces. Due to the large size of the solid particles in a typical packed bed, only drag force was considered to represent the interaction forces between gas, liquid and particles instead of other forces such as thermophoretic, Brownian and lift forces. In many reported studies, the addition of interaction forces for Eulerian approaches is via source terms in the momentum equations, and for Lagrangian approaches in the particle force balance. In the current study, the Gidaspow drag model [126], commonly used for densely-packed beds, is chosen to represent the drag forces between gas and solid, liquid and solid, and gas and liquid. The basic formulation for the drag force on the continuous phase *q* from a discrete phase *p* is as follows:

$$\vec{F}_{drag} = K_{\mathrm{pq}}\left(\vec{v}_{\mathrm{p}} - \vec{v}_{\mathrm{q}}\right) \tag{47}$$

where K_{pq}, the momentum exchange coefficient, is calculated based on either the Wen and Yu model [133] ($\alpha_{\mathrm{q}} > 0.8$) or the Ergun equation [134] ($\alpha_{\mathrm{q}} \leq 0.8$) as follows:

$\alpha_{\mathrm{q}} > 0.8$:

$$K_{pq} = \frac{3}{4} C_d \frac{\alpha_{\mathrm{p}} \alpha_{\mathrm{q}} \rho_{\mathrm{q}} \left| \vec{v}_{\mathrm{q}} - \vec{v}_{\mathrm{p}} \right|}{d_{\mathrm{p}}} \alpha_{\mathrm{q}}^{-2.65} \tag{48}$$

$$C_d = \frac{24}{\alpha_{\mathrm{q}} Re_{\mathrm{p}}} \left[1 + 0.15 \left(\alpha_{\mathrm{q}} Re_{\mathrm{p}} \right)^{0.687} \right] \tag{49}$$

$\alpha_{\mathrm{q}} \leq 0.8$:

$$K_{\mathrm{pq}} = 150 \frac{\alpha_{\mathrm{p}}^2 \mu_{\mathrm{q}}}{\alpha_{\mathrm{q}} d_{\mathrm{p}}^2} + 1.75 \frac{\alpha_{\mathrm{p}} \rho_{\mathrm{q}} \left| \vec{v}_{\mathrm{q}} - \vec{v}_{\mathrm{p}} \right|}{d_{\mathrm{p}}} \tag{50}$$

where Re_{p} is the relative Reynolds number similar to Eq. (31), with phase *p* replacing the particle variables and phase *q* the gas variables.

The above formulation of the Gidaspow model is used to represent fluid-solid flows in many CFD studies [77, 92, 135]. However, a two-phase flow is typically assumed in the classical formulation, with the porosity, ε, replacing α_{q}, and $(1 - \varepsilon)$ in place of α_{p}. This is intuitively extended to approaches that use the VOF method, with ε set equal to the fluid volume fraction, and hence, the solid volume fraction is $(1 - \varepsilon)$. There are very few studies for three-phase flows which incorporate the Gidaspow drag model, and of those which do, the model is typically applied to interactions between two phases only, i.e., gas-solid, liquid-solid, or fluids-solid [22, 98]. In CD-MELT, we use the Gidaspow drag model to model interactions between two individual phases, namely, gas-liquid, gas-solid and solid-liquid, replacing phase *q* terms with the less dense phase and phase *p* terms with the denser phase accordingly. The underlying assumption is that each pair of interphase interactions is treated through distinct and separate forces, and the magnitude of the forces only depends on the properties of the two phases involved, such as the density, volume fraction and velocity. The existing drag model is capable of representing the resistance to the motion of the molten slag through the packed bed. However, for smaller MSW and solid slag particles, other forces such as pressure gradient or lift forces might also be needed as they can be carried out of the domain via the gas.

3.5 Interphase heat transfer

CD-MELT models the Eulerian secondary liquid phase through an assembly of spherical droplets. The representation allows the tracking of the liquid phase distinctly and independently, and the interphase exchange coefficients such as drag forces and heat transfer are based on this representation. Hence, the range of droplet diameter must be carefully chosen as it will directly affect the calculation of gas-liquid interfacial area, liquid flow and temperature. When the volume fraction of liquid increases, the interfacial area should decrease and less heat transfer should occur between liquid and gas. To account for this effect, the droplet diameter is calculated as follows, assuming one droplet is located in each fluid cell:

$$d_{\mathrm{l}} = \left(\frac{6\alpha_{\mathrm{l}} V_{\mathrm{cell}}}{\pi}\right)^{\frac{1}{3}} \tag{51}$$

where d_{l} is the diameter of a single spherical droplet based on the total equivalent liquid volume in each cell, and V_{cell} is the volume of the cell.

For the three-phase flow, heat transfer is only assumed to occur between the gas phase and the other phases, as represented by the Q_{lg}, Q_{gl} and Q_{pg} terms. The volumetric heat exchange between the gas and liquid phases is a function of the temperature difference and interfacial area as follows:

$$Q_{\mathrm{lg}} = -Q_{\mathrm{gl}} = h_{\mathrm{lg}} A_i \left(T_{\mathrm{l}} - T_{\mathrm{g}}\right) \tag{52}$$

where h_{lg} is the convective heat transfer coefficient based on the Ranz-Marshall correlation [127], similar to Eq. (29) to Eq, (31), but with the particle variables being replaced by the liquid droplet variables. The interfacial area per unit mixture volume between the two phases, A_i, is computed from an algebraic relationship with the spherical droplet diameter and liquid volume fraction [78]:

$$A_i = \frac{6\alpha_{\mathrm{l}}}{d_{\mathrm{l}}} \tag{53}$$

Q_{pg} is the heat exchange between the solid particles and gas, and is calculated as the change in thermal energy of the particles:

$$Q_{\mathrm{pg}} = m_{\mathrm{p,i}} \int_{T_{\mathrm{ref}}}^{T_{\mathrm{p,i}}} c_{\mathrm{p,p}} dT - m_{\mathrm{p}} \int_{T_{\mathrm{ref}}}^{T_{\mathrm{p}}} c_{\mathrm{p,p}}\, dT \tag{54}$$

where $m_{\mathrm{p,i}}$ and $T_{\mathrm{p,i}}$ represent the mass and temperature of the particle at the beginning of each timestep respectively, and $c_{\mathrm{p,p}}$ is the specific heat of the particle at constant pressure. It is noted that when the particle is within the melting temperature range, Q_{pg} is equal to Q in Eq. (41), representing the heat absorbed from the gas phase, even if the particle does not melt and undergo a mass reduction. The last term on the right-hand side for the liquid phase energy equation (Eq. (12)), $S_{mass}(h_{melt} - h_{ref})$, is the source term added from the enthalpy of the molten liquid during the melting process.

Chapter 4. Two-phase isothermal melting

4.1 Overview

CD-MELT is developed to model the isothermal melting of a packed bed subjected to a forced convection with higher temperature. The formulation of CD-MELT allows a high degree of representation of the melting process. With specific melting parameters, the particles in the packed bed undergo mass, diameter and temperature change individually, and the packed bed is reconfigured afterward through particles collision and contact. CD-MELT's predictions are compared with the results from an earlier experimental study on the melting of a single ice sphere as well as a packed bed of ice spheres due to a forced convection of warm water. The comparison is found to be satisfactory despite the use of a coarse mesh, and the computational run is stable despite the varying mesh-particle size ratio. Finally, the effects of spring constant and restitution coefficient in the particle collision model are further investigated for the case of a non-floating packed bed under forced convection. Recommendations are made on how their suitable values can be determined in future melting studies.

4.2 Melting of a single particle

CD-MELT is first evaluated via comparing the predictions with experimental results of a single ice particle subjected to forced warm water convection by Hao and Tao [136]. The experiments recorded the change in shape, surface area and equivalent spherical diameter of the melting ice sphere under the forced convection in a horizontal open channel. In CD-MELT, the ice sphere is assumed to remain as a sphere throughout the melting process. Hence, the verification is based mainly on the comparison of the equivalent diameter.

We note that the size ratio is usually not a primary concern in studies that do not involve melting, and their grid sensitivity analysis is typically carried out with a fixed particle diameter. However, in CD-MELT, the tracking of melt is a primary objective, which is controlled by the associated phase change and the changing diameter of the particles during the melting process. Hence, in this study, the effect of the mesh-to-particle size ratio is first considered and investigated by refining the mesh used in the simulation. For all the simulations done in Chapter 4, the CFD and DEM timesteps are chosen to be 0.1 s and 1 ms respectively, which are deemed to be sufficient as we find that using smaller steps produce similar results in the simulations.

4.2.1 Simulation model

In the experimental setup by Hao and Tao [136], the warm water flow occupied a test section of 500 mm × 152 mm × 130 mm, and the ice particle of initial diameter of 36 mm was fixed to the bottom via a straw and base. A numerical domain is established for this configuration as shown in Figure 4.1.

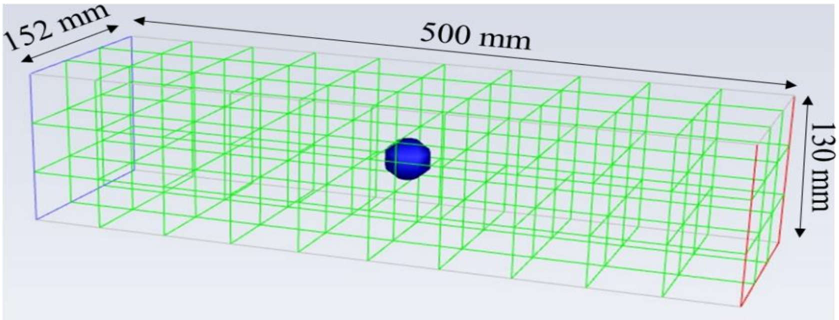

Figure 4.1. Simulation setup for the melting of a single ice particle under forced warm water convection.

Table 4.1 lists the properties of water and ice used in the simulations, with the ice properties assumed to be constant over the temperature range of 257.15 K to 273.15 K. To replicate the experimental conditions, the inlet water temperature and velocity are fixed at 299.15 K and 0.06 m/s, respectively, as the boundary conditions as well as the initial conditions throughout the domain. The particle is injected as an inert particle into the centre of the domain at the beginning with a temperature of 257.15 K and its melting temperature set at 273.15 K. Since the position of the ice sphere is unchanged, the only force acting on the particle is the drag force exerted by the moving fluid (i.e. the gravitational and buoyancy forces are neglected). In the simulations, the particle position is fixed by setting its velocity to be zero in all three directions via a simple UDF.

Table 4.1. Physical properties of ice and water.

Physical Property	**Water**	**Ice**
Temperature, T (K)	299.15	257.15 – 273.15
Density, ρ (kg/m^3)	995.67	920
Specific heat capacity, c_p (J/kg·K)	4180	2100
Thermal conductivity, k_f (W/m·K)	0.62	-
Latent heat of melting, h_m (J/kg)	-	334, 000
Dynamic Viscosity, μ (kg/m·s)	800.82×10^{-6}	-

During the simulations, the particle diameter and heat transfer rate to the particle are output regularly in order to compare with the experimental results later. The typical mesh size used is 47.9 mm edge length (EL). However, the simulations are also repeated with a smaller mesh (23.9 mm edge length) to investigate the effect of the mesh-particle size ratio on CD-MELT predictions.

4.2.2 Validation and transient characteristics

In this section, we compare the CD-MELT predictions with the experimental results from Hao and Tao [136] for validations. Figure 4.2 presents the comparison on the heat transfer rate to the particle over the time period that the ice takes to melt completely. In the predictions, the heat transfer rate decreases almost linearly over time as the ice particle melts. The comparison on the transient evolution of the equivalent spherical diameter based on the same ice volume is also shown in the figure.

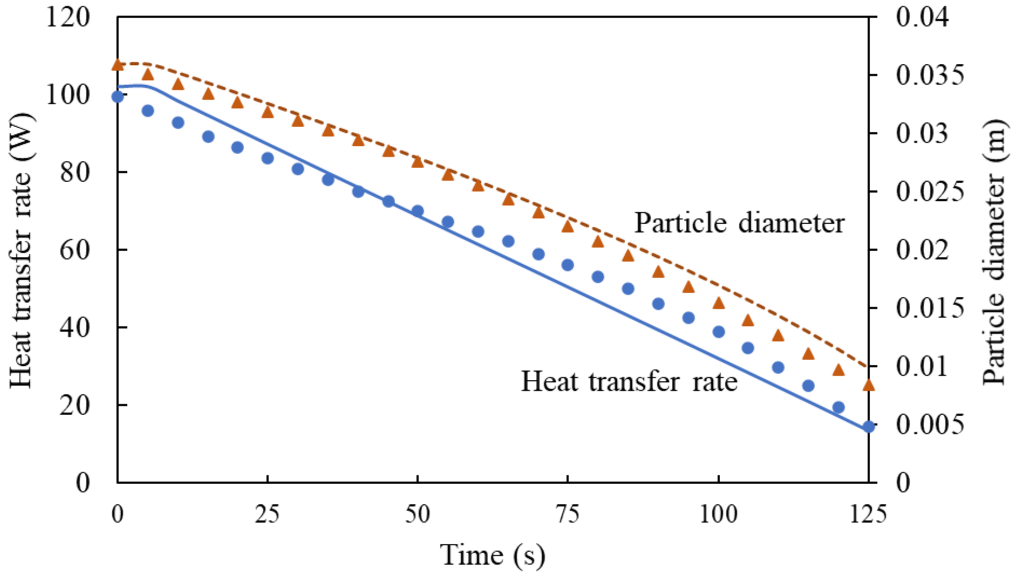

Figure 4.2. Melting of a single ice particle: Comparison of heat transfer rate to particle (●) and particle diameter (▲) over time (lines are predictions, point markers are experimental results [136])

From the figure, it can be observed that CD-MELT slightly over-predicts the particle diameter. The difference is however deemed to be acceptable given that the change in particle shape is not fully accounted for and the temperature within the particle is assumed to be uniform. It is also noted that the discrepancy in the particle diameter between the experiment and simulation increases over time. As remarked by Hao and Tao, the shape of the melting ice particle became increasingly irregular, and the surface area would become significantly larger than that of a sphere with the same volume which was also observed in the experiments [136]. In addition, the local heat transfer coefficient was relatively evenly distributed across the downstream half of the particle, and the conduction effect was generally not significant except for a short initial period. Hence, the use of the particle-averaged heat transfer coefficient in CD-MELT is sufficient to represent the heat transfer process. Under free convection, Guo et al. [137] found that the local heat transfer coefficient on the upwind side is larger than the downwind side and the ice sphere experiences non-uniform melting. This effect would be further enhanced under forced convection. The shape irregularity directly contributes towards a slightly higher melting rate and smaller particle diameter over time.

4.2.3 Effect of mesh size

As mentioned above, two mesh sizes are tested in the simulations: 47.9 and 23.9 mm edge length. The mesh-particle size ratio (SR) obtained is calculated and shown in Figure 4.3. The effects of the mesh size on the changing particle diameter, size ratio and percentage error are also illustrated in the figure. It can be observed that a smaller mesh size generally leads to a smaller particle diameter, implying higher melting rate. However, the difference in the predicted diameter with the two mesh sizes is not too significant (mostly less than 10%). Additionally, even though the initial size ratio of the smaller mesh is below 1, the simulation is found to be numerically stable. This can be attributed to the node-based averaging process in Fluent [78], where the effects of particle properties such as volume fraction, velocity, and temperature, are distributed to the surrounding mesh nodes and not being limited to the cell centre that the particle is in. In CD-MELT, a Gaussian distribution is used for the weighting function with a Gaussian factor of 6 [138]. Nevertheless, the percentage error with the smaller mesh is consistently lower, suggesting that having a smaller size ratio would improve the model predictions. Overall, CD-MELT is deemed to have performed reasonably well in the melting of a single ice particle.

4.3 Melting of a packed bed of ice particles

The verified CD-MELT for the single ice particle is extended to simulate the convective melting of a granular packed bed of ice particles which experiments were also carried out in another study by Hao and Tao [139]. Since a packed bed consists of many particles in contact with each other, the modelling of the collisions and heat transfer among particles is of primary importance, which is the key objective of the verification. Similar to the single particle simulation, the effect of water inlet temperature and velocity on melting rate is studied, and the experiment results are compared with the CD-MELT predictions to assess its accuracy for packed bed simulations.

In the linear-spring dashpot model for the DEM collisions, a key challenge is to determine the spring constant, K, and the normal restitution coefficient, η, which there is no universal method at present and their values varied widely in the literature. Several studies used an artificially lower K in order to be able to adopt a larger particle timestep [27, 81, 82, 140] to reduce the computational time. However, if K is too small, the particles will penetrate each other. On the other hand, Marchelli et al. [121] claimed that the results are not significantly affected by the value of K if it is more than 100 – 1000 N/m.

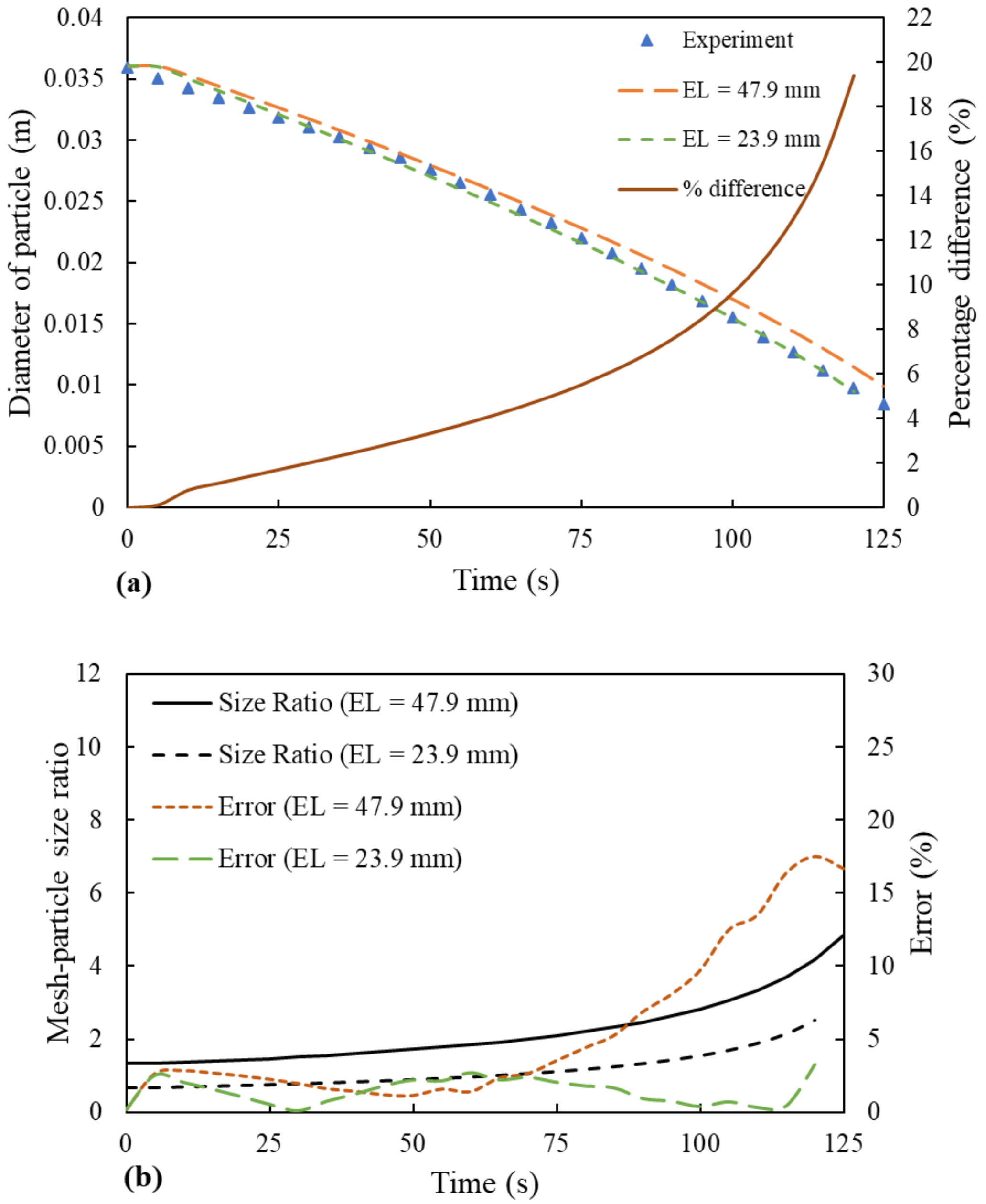

Figure 4.3. Melting of a single ice particle: Effect of mesh edge length (EL = 47.9 mm and EL = 23.9 mm) on (a) Melting particle diameter and percentage difference between the two meshes; (b) Size ratio and percentage error compared to experiment diameter [136].

η represents essentially the ratio of relative velocity between two particles before and after impact; the smaller the value, the more the particle energy dissipation shall be upon collision. Experimental studies investigating η allege that it is dependent on the particle material, surface conditions, impact velocity, as well as the particle size [141-143]. Moreover, for simplification, DEM simulations often use a single value to represent the spring constant and restitution coefficient between two particles of the same material, regardless of the size of the two particles or their relative impact velocity. In the following, we shall investigate how these two constants affect the average porosity and particle packing for a non-floating packed bed, so as to provide insights on how their appropriate values can be determined under dynamic conditions.

4.3.1 Simulation model

The experiments by Hao and Tao were conducted in a horizontal test section, and the ice spheres were removed and weighed at regular intervals to track the mass of the packed bed before resubmerging back into the flow. In our simulations, the packed bed is generated by randomly injecting a total mass of 2.0 kg of particles with a diameter of 26.2 mm (a total number of 231 particles), into a stationary ambient water with dimensions 300 mm × 152 mm × 100 mm (L × W × H). Therefore, only net buoyancy forces and contact forces are acting on the particles initially, and these particles float upward due to their lower density forming the packed bed. After they have reached the equilibrium packing state, their positions are then saved and used as the starting positions for the actual simulations as shown in Figure 4.4.

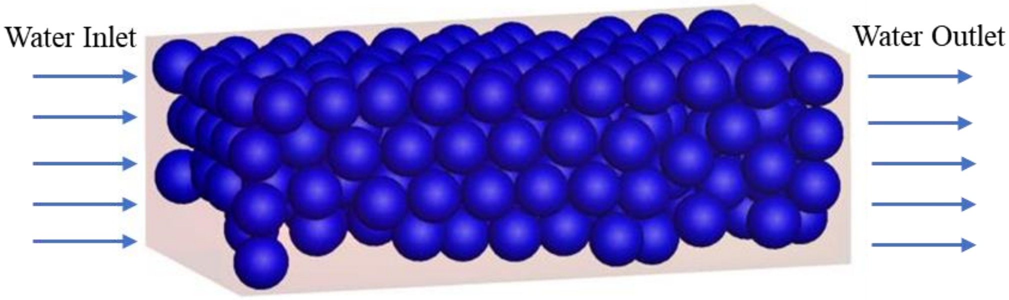

Figure 4.4. Starting positions of particles (ice spheres) in the packed bed simulations.

Similar to the single particle configuration, the simulation is started by setting the water temperature and velocity throughout the domain to represent the steady flow, and the particles of the packed bed are then inserted at their respective positions. The velocity at the inlet is specified normally to the boundary, while the top boundary and outlet are set to outflow boundary conditions. The boundary conditions of the side and bottom walls are set to be non-slip and adiabatic. Here, the UDFs are connected to Fluent via three distinct routes: (i) the specification of particle characteristics for the heat and mass exchange, (ii) the stipulation of source terms to the fluid phase, and finally (iii) the initialization for the creation and record of particle variables.

A total of six cases are carried out to examine the effects of inlet water velocity and temperature on the melting rate. Three different inlet velocities, i.e. 0.01, 0.05 and 0.1 m/s are first simulated with the inlet water temperature set at 303.15 K. Subsequently, three different inlet water temperatures, i.e. 303.15, 293.15, and 283.15 K, are also simulated with the inlet water velocity at 0.1 m/s to examine the temperature effect on the melting rate. The total enthalpy source to the fluid phase and mass of the packed bed in the domain is recorded throughout the simulations, along with the individual particle parameters including the diameter, latent heat absorbed and mass, in separate data files. The initial temperature of the ice particles in the packed bed is set at 253.15 K, and the isothermal melting point, T_m, is 273.15 K. Table 4.2 shows the parameters used for the particle collision model.

Table 4.2. Parameters used for the DEM collision model.

Parameter	**Value**
Initial number of particles	231
Particle-particle spring constant (N/m)	200
Particle-wall spring constant (N/m)	400
Normal restitution coefficient, η	0.6
Friction coefficient, μ_{fr}	0.3

For the simulation setup for the packed bed simulations, we also examine the need for turbulent modelling for this case which requires extensive computational time and resources. Inside the porous space of the packed bed, the Reynolds number is small and hence the laminar flow modelling with associated heat transfer might be appropriate. Exterior to the packed bed, however, the flow is typically turbulent, and the surface of the packed bed is thus subjected to turbulent heat transfer. The ideal combination would be a Reynolds closure that encompasses a good laminar-turbulent transition; however, such closures are normally inaccurate at present [144]. Instead, we investigate by comparing the CD-MELT results between full laminar modelling and full turbulent modelling for the packed bed for inlet velocities of 0.01 and 0.05 m/s. The results are shown in Figure 4.5. Based on the results, the use of the RNG k-ε closure to account for the turbulent Reynolds stresses does not lead to significant changes in the melting rate and mass of the packed bed in CD-MELT's predictions. At the same time, we find that the full laminar modelling for the inlet velocity of $v = 0.1$ m/s ($Re >$ 10000) causes numerical instability frequently. Hence, the turbulence closure is used in CD-MELT for this case, despite the potential savings in the computational time and resources.

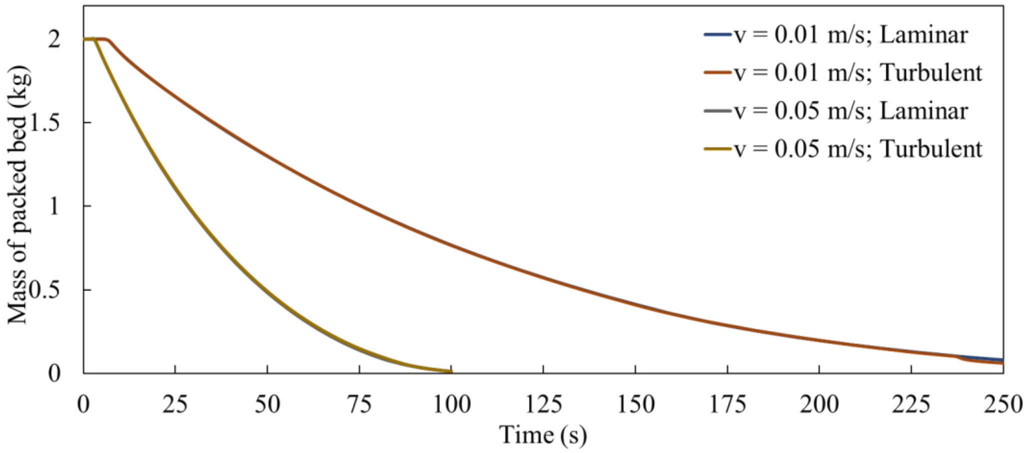

Figure 4.5. Melting of a packed bed under forced convection: Comparison of laminar and turbulence closures (RNG k-ε model) on the mass of packed bed at inlet water velocity of $v = 0.01$ and 0.05 m/s and $T = 303.15$ K.

4.3.2 Effect of inlet velocity and temperature

In this section, we compare the numerical predictions directly with the experimental results for the packed bed simulations to assess the accuracy of CD-MELT. In our preliminary studies, despite the use of the node-based averaging approach, reducing the mesh edge length (from EL = 36.2 to 18.1 mm) often leads to numerical instabilities. This suggests the mesh-particle size ratio cannot be reduced freely for the packed bed simulations due to the close proximity as well as high solid volume fraction of the particles. However, for the time period that both EL simulations are stable, the difference of the total mass of the packed beds is less than 10% between the two mesh sizes. Hence, we conclude that CD-

MELT's predictions on the melting rate are not significantly affected by the mesh size.

Figure 4.6 compares the effect of inflow velocity on the mass of the packed bed. Both the experimental and CD-MELT's results show that higher inlet velocities induce higher convective heat transfer rates to the ice particles and increases the melting rate. CD-MELT slightly over-predicts the melting rate of the packed bed with v = 0.1 and 0.05 m/s, but under-predicts the melting rate at v = 0.01 m/s. The discrepancy between the predicted and experimental results increases over time, suggesting that the packing dynamics and particle size have a significant effect on the heat transfer. As the particles melt, they reduce in size and the local flows around the particle become more important in determining the heat transfer coefficient and melting rate of the particles. As the heat transfer coefficient in CD-MELT is based on a forced convection regime and linked to the particle Reynolds number, it is under-predicted at low flow velocities, leading to a lower melting rate. In such cases, heat transfer correlations for a natural [145] or mixed convection [146] would be more appropriate. Thus, the under-prediction of the melting rate at low velocities and a higher predicted mass of the packed bed, as shown in Figure 4.6, can be directly attributed to this consideration. This agrees with the observations by Ou et al. [147] that the melting rate is strongly influenced by the convective heat transfer via thermal buoyancy under natural convections.

Figure 4.7 presents the effect of water inlet temperature on the mass of the packed bed. Similarly, as the water inlet temperature increases, so does the convective heat transfer and melting rate. The CD-MELT's predictions are also reasonable compared with the experimental results, and with good agreement for cases with higher water inlet velocities. This implies that the bed packing, which changes more significantly with velocity than temperature, is an important factor in affecting melting rate and not represented as well in CD-MELT. At the same time, CD-MELT is able to capture the effect of change in temperature on melting rate very well. The discrepancies towards the end of the melting process, when the particles become small and their shape irregular, are probably due to changes in the local heat transfer coefficients that are not fully accounted for in CD-MELT.

Figure 4.8 provides a visual illustration of how the particle diameter and mass loss fraction change throughout the melting process with the three inlet temperatures. Due to the lower density of the ice particles, the particles then float upwards and are pushed to the right by the flow convection. We note that convective heat transfer to the particles should be most efficient at the bottom of the packed bed where the exterior water velocity is the fastest. Hence, as expected, the particles located at the top right corner take the longest time to melt. Typically, a very fine mesh and small timesteps are needed to increase the accuracy of numerical simulations, especially in cases where local fluid flows must be fully resolved. However, in CD-MELT, we find that the coarse mesh still performs satisfactorily for the modelling of melting in the packed bed under forced convection for this case.

4.3.3 Variation of spring constant and restitution coefficient

We also investigate the effect of the spring constant (K) and the normal restitution coefficient (η) on the packing pattern of the ice spheres in the floating bed. These two parameters affect the forces among the particles, and directly influence the packing configuration and the resulting melting behaviour. From the experiments, it was observed that the flow velocity affects the packing of the bed significantly, i.e. given the same mass and material of the packed bed, there exists a velocity threshold such that the convective force by the flow dominates over the buoyancy force. Above this threshold, the ice particles are pushed against the wall instead of floating upwards, forming non-floating packed beds instead.

For the simulations conducted for the non-floating packed bed, the initial total mass of ice particles is 1.0 kg, with each ice particle having an initial diameter of 26.2 mm and temperature of 253.15 K. The inlet water velocity is set at v = 0.13 m/s, and the temperature set at 303.15 K. The values of η are chosen to match experimental measurements for ice spheres [143], which were observed to be from 0.95 to 0.6 at low velocities. The values of K are set to vary from 200 to 1800 N/m, as values outside of this range lead to numerical instabilities or require an excessively small DEM timestep. The 12 combinations of K and η tested are listed in Table 4.3.

Table 4.3. Combinations of restitution coefficients and spring constants

Restitution coefficient	**Spring constant (N/m)**
0.3	1000
0.6	200, 600, 1000, 1400, 1800
0.8	400, 600, 1000, 1400, 1800
0.9	1000

From the simulations, the iso-surface with a fluid volume fraction, α_{f} = 0.8 is deemed to be the best representation of the interface between the packed bed and fluid region. The line representing $\alpha_{\mathrm{f}} = 0.8$, at $z = 0.076$ m (middle plane of domain), is then extracted and plotted for all the cases. To estimate the average porosity of the packed bed, the fluid cells with $\alpha_{\mathrm{f}} > 0.8$ are removed, as illustrated in Figure 4.9. The average porosity is calculated as the ratio of the remaining volume of fluid to the total volume of the cells.

Figure 4.10 shows the effects of the spring constant on the average porosity and liquid-solid interface. In general, the average porosity generally increases over time and is not significantly affected by the value of K. The simulation results show that a higher K increases the contact force upon collision with other particles, resulting in the particles not being able to pack as tightly as shown in Figure 4.10(c) and (d). This observation agrees with Zhang et al.'s [148] results that the packing density decreases with a higher spring constant. Given a lower restitution coefficient ($\eta = 0.6$), the sensitivity to the change in spring constant also decreases. With the increase in the damping coefficient, the contact forces are damped more significantly, and thus the particles have less kinetic energy to repack. Hence, we find that using a smaller spring constant with a lower restitution coefficient does not significantly impact the packing of the bed under forced convection. Instead, it provides the advantage of enabling a larger DEM timestep to be used and reduces the computational time.

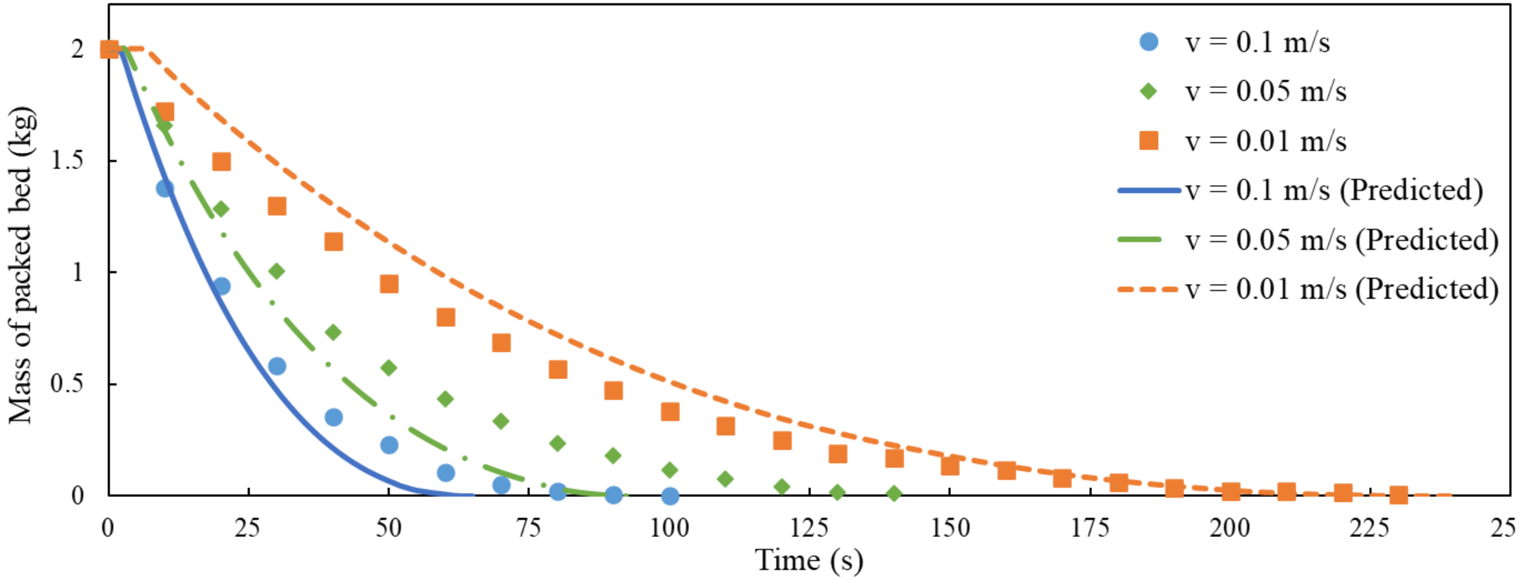

Figure 4.6. Melting of a floating packed bed under forced convection: Effect of water inlet velocity (v = 0.1, 0.05, and 0.01 m/s) on mass of packed bed at fixed inlet temperature (T = 303.15 K) over time (lines are predictions, point markers are experimental results [139]).

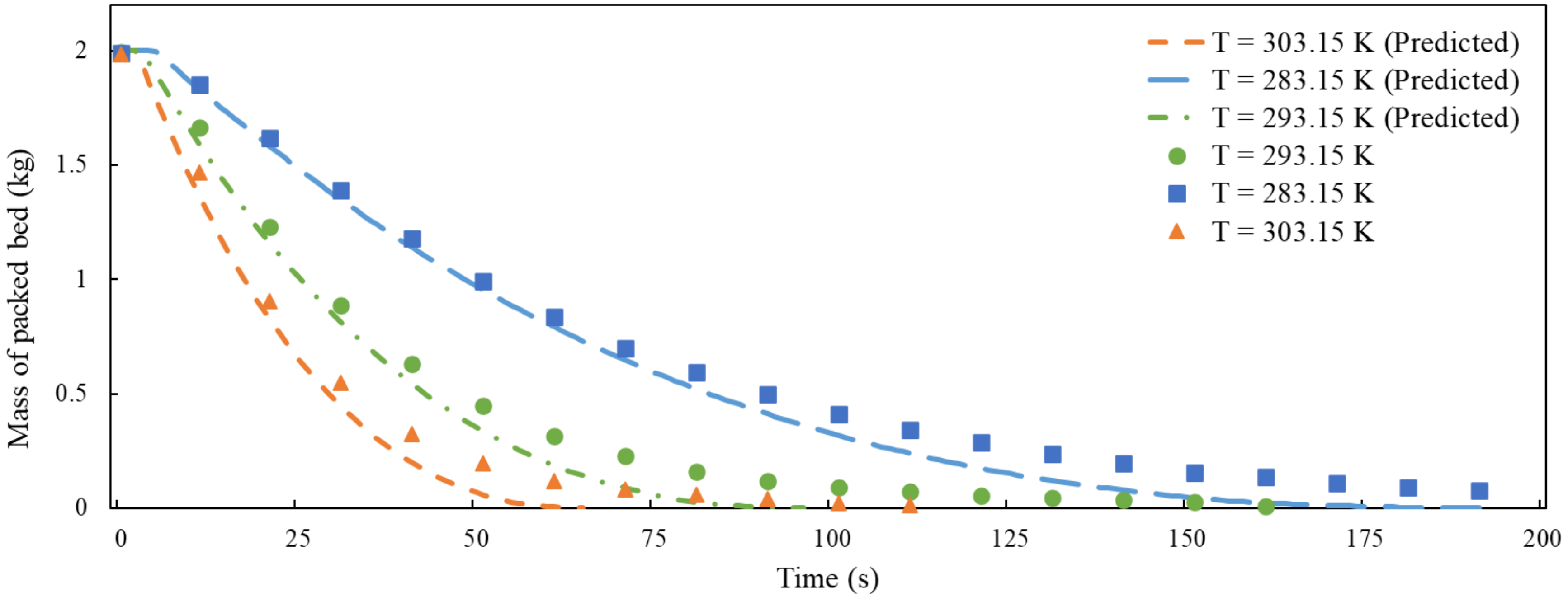

Figure 4.7. Melting of a floating packed bed under forced convection: Effect of water inlet temperature (*T* = 303.15, 293.15, 283.15 K) on mass of packed bed with fixed inlet velocity (*v* = 0.1 m/s) over time (lines are predictions, point markers are experimental results [139].

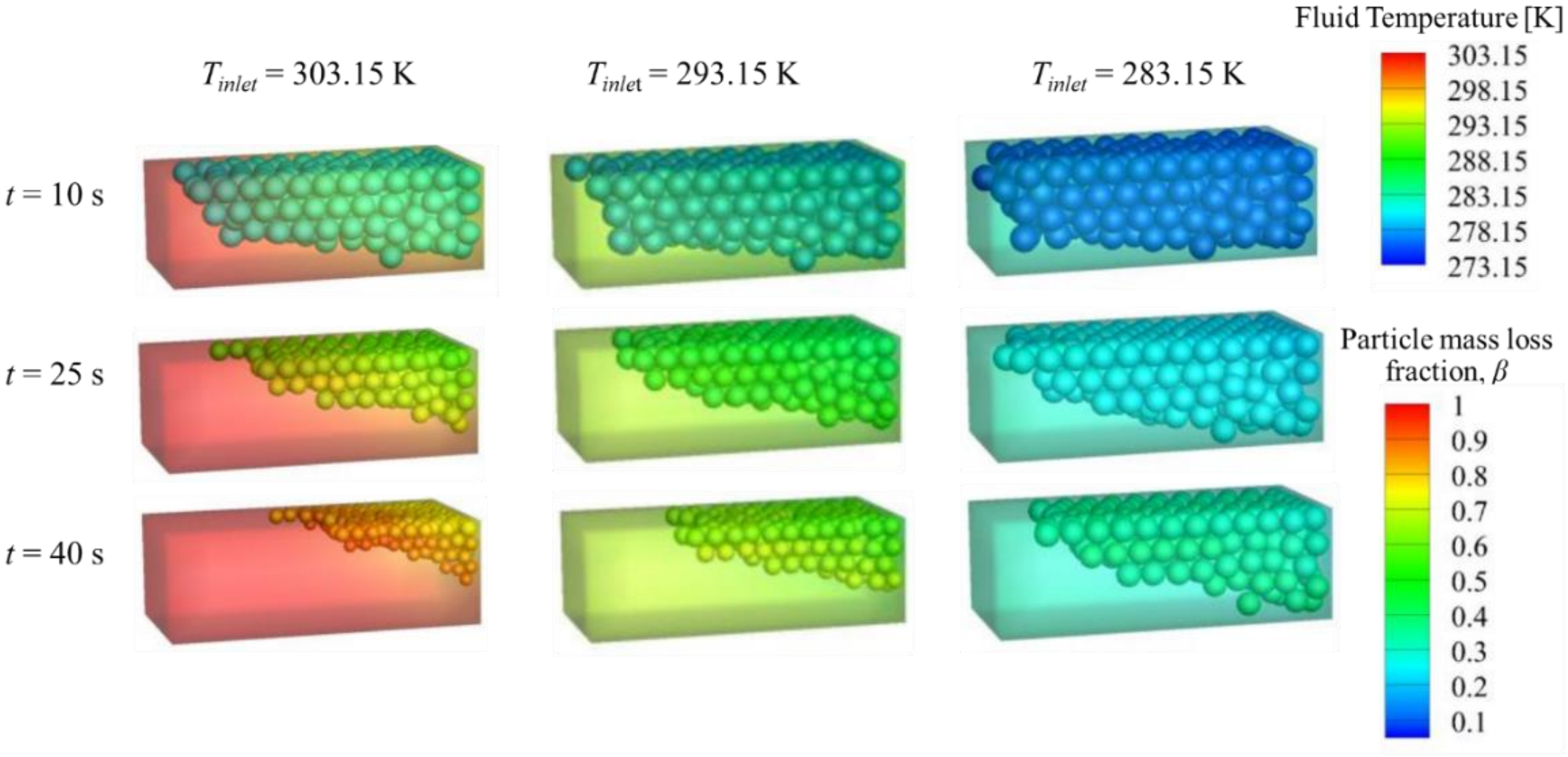

Figure 4.8. Melting of a floating packed bed under forced convection: Change in particle diameter and mass loss fraction (β) at different inlet temperatures (T = 283.15, 293.15, and 303.15 K), at t = 10, 25, and 40 s, and v = 0.1 m/s.

Figure 4.11 depicts the effect of change in η on the average porosity and liquid-solid interface given a fixed value of K. No significant impact on porosity can be observed given $K = 1000$ N/m. Except for $\eta = 0.3$, in general, particles are slightly more compact with a lower restitution coefficient, packing more towards the water outlet. This is because more kinetic energy is dissipated upon collision with a lower restitution coefficient, thus the particles are less able to rearrange and are instead pushed by the flow towards the right.

The overall results show that the spring constant and restitution coefficient do not influence the average porosity and liquid-solid interface significantly in a forced convection at higher velocities. This is likely due to the fact that the drag force dominates over the particle collision forces in this situation generally, restricting the particles' freedom to repack. Under cases with a different fluid medium or even different particle geometry, the choice of spring constant and restitution coefficient might be more important as suggested by others [149, 150] in the literature.

Lastly, there exists an upper limit on the spring constant in order that the particles can be tracked correctly to ensure numerical stability, i.e. the particle collision time needs to be larger than the DEM timestep. The particle collision time is a function of the effective mass, restitution coefficient and spring constant (Eq. (25)) of the particles and is most sensitive to the spring constant. During the melting process, the particle collision time decreases continuously as the particles' masses are reduced. Hence, we recommend that the spring constant or the DEM timestep to be set such that the initial collision time is at least 15 times the DEM timestep if the particle is removed at ~1% of the initial particle mass (β

= 0.99). However, if the particle is removed at an earlier stage ($\beta < 0.99$), the mass of the particle and collision time is larger, hence the upper limit of the spring constant should be increased. Nonetheless, the spring constant and restitution coefficient are found to have minimal effects on melting rate and heat transfer to the particles and hence the mass of the packed bed for all simulation cases. Given these results, the chosen values of K = 200 N/m and η = 0.6 for our study in order to use a larger DEM timestep is justified.

4.4 Summary

An original CFD-DEM method named as CD-MELT was developed in this study to simulate the isothermal melting of a packed bed under forced convection with a higher temperature. The formulation of CD-MELT allows each particle to undergo mass and temperature changes individually rather than relying on averaging assumptions, and thus enables the modelling of particle materials with different heat capacities or melting temperatures. It also accounts for the continuous diameter change of the particles during melting and allows for the modelling of the melt via source terms, which is crucial for simulating the full three-phase flow. The melting change is described through a key melting parameter, β, which is unique to every particle. Thus, CD-MELT has a high degree of control and representation of the entire melting process.

In this study, the predictions of CD-MELT for the melting of ice spheres under a forced convection of warm water are validated with the experimental results for the two cases of a single particle and a packed bed. The comparison shows that CD-MELT is able to predict the melting rate reasonably well, and the

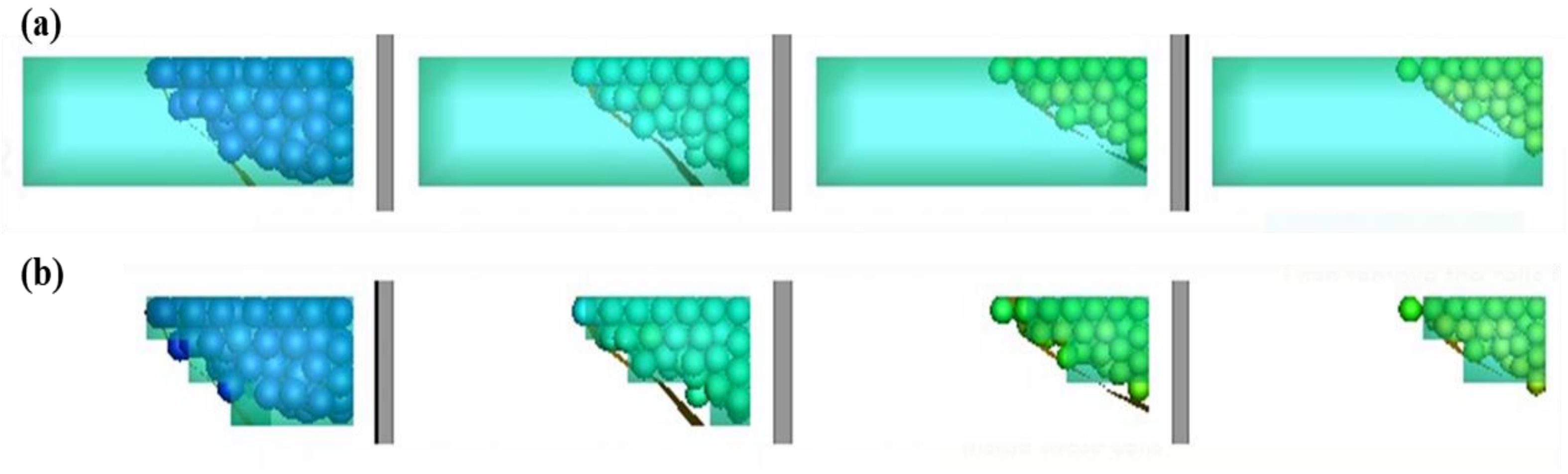

Figure 4.9. Side view of the non-floating packed bed under forced convection at t = 10, 30, 50 and 60 s; (a) Original data, and (b) after removal of fluid cells with $\alpha_{\mathrm{f}} > 0.8$ for calculation of average porosity within the packed bed. The iso-surface representing $\alpha_{\mathrm{f}} = 0.8$ is also shown.

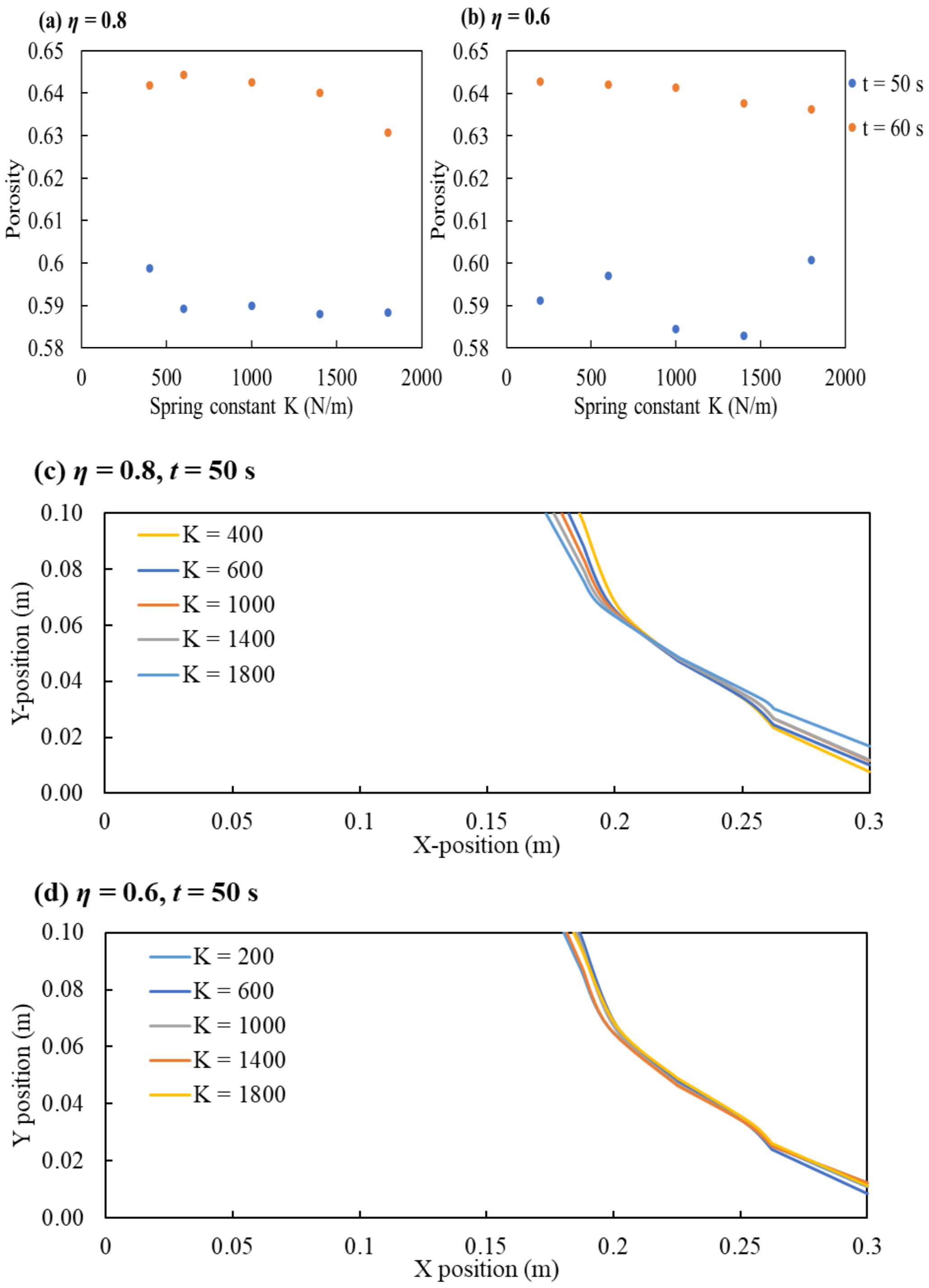

Figure 4.10. Melting of a non-floating packed bed under forced convection: Effect of spring constant on average porosity at t = 50 and 60 s for η = (a) 0.8 and (b) 0.6; and on liquid-solid interface at t = 50 s for η = (c) 0.8 and (d) 0.6.

(a) *K* = 1000 N/m

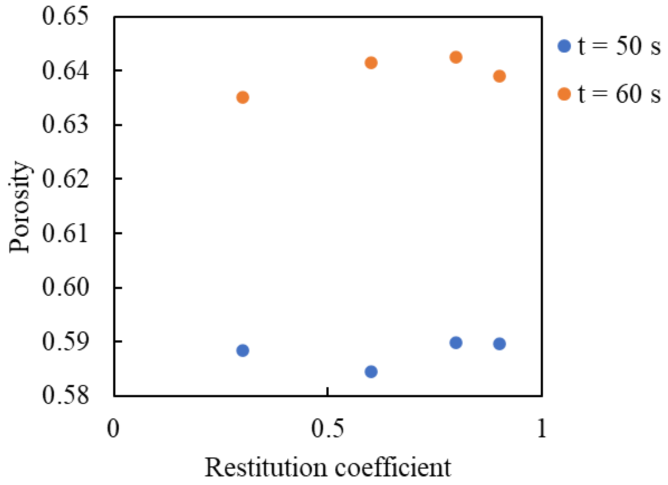

(b) *K* = 1000 N/m, *t* = 50 s

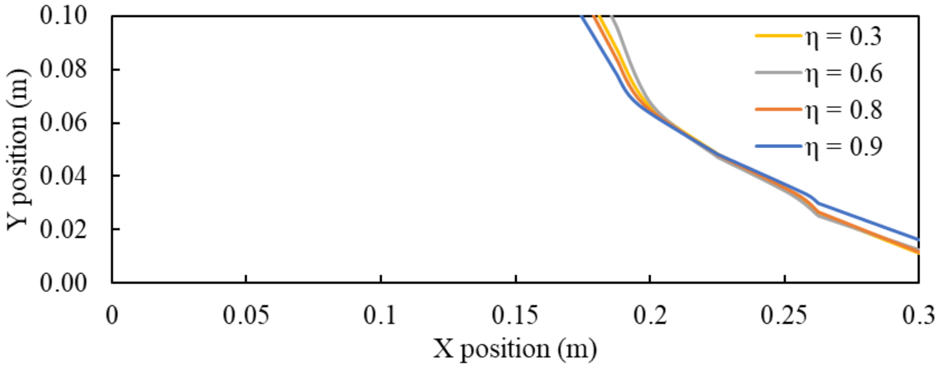

Figure 4.11. Non-floating packed bed: Effect of restitution coefficient, given *K* = 1000 N/m, on (a) average porosity at *t* = 50 and 60 s; and (b) liquid-solid interface at *t* = 50 s.

changing mesh-particle size ratio does not significantly affect the stability of the computation runs. The spring constant and restitution coefficient in the linear-spring dashpot model for DEM collisions are further evaluated in terms of the particle packing and melting rate. It is found that smaller values of these two parameters facilitate a larger DEM timestep without sacrificing the simulation accuracy.

Chapter 5. Three-phase non-isothermal melting

5.1 Overview

The formulation of the CFD-DEM method, CD-MELT, is further extended to three phases (gas, liquid and solid) with melting in this study. The new CD-MELT provides the characterizations of the three individual phases, which is superior to the current VOF approaches whereby the fluid phases (gas and liquid) are lumped together in the computational cell and not distinguished. In addition, CD-MELT allows for the consideration of both latent heat and sensible heat in the non-isothermal melting process via the introduction of a particle enthalpy variable, where the melting rate is determined by the balance of heat gained from convection and heat required for melting. To demonstrate the new capability, CD-MELT is applied to simulate the non-isothermal melting of wax spheres packed in a single layer in a glass bed subjected to forced air convection with higher temperature, where the setting is similar to an earlier experimental study. In this application, the coarse graining approach is adopted to simplify the modelling of the melting rate and bed packing, based on theoretical considerations of the source terms and variables for non-isothermal melting. The predictions of CD-MELT are then compared with the published experimental and theoretical studies related to this application. It is found that latent heat and most importantly tracking of the melted liquid phase are dominant factors in order to simulate the melting process accurately. Furthermore, the predictions on the melted liquid movement through the packed bed by CD-MELT provides additional insights to the gas channel formations and liquid holdup phenomena which cannot be obtained using the VOF approach.

5.2 Application example: Melting of wax particles in a packed bed

CD-MELT is used to simulate the convective non-isothermal melting of wax particles in a packed bed based on the laboratory study of Chew et al. [151]. They performed experiments to replicate the cohesive melting zone in a blast furnace, through observation of the softening-melting characteristics of a flat, cohesive wax layer across the reactor diameter. The reactor comprised of a cylinder with dimensions 300 mm (diameter) × 600 mm (height), with an open end at the top for gas release, and liquid can exit only through the base plate. The pressure at the bottom and temperature at different bed heights were measured via sensors and thermocouples.

5.2.1 Simulation model

To accelerate the computation, we adopt a coarse graining approach with CD-MELT to simulate the application example. A total number of 2074 glass parcels and 937 wax parcels are included. The geometry, mesh and bed packing conditions before melting are shown in Figure 5.1. A relatively coarse mesh was used, comprising of 4280 hexahedral cells and characteristic edge length of 0.030 m. The CFD and DEM time step are chosen to be 0.1 s and 0.005 s, respectively. The simulation begins by setting the gas inlet temperature and surface to 363.15 K and velocity in the upwards *y*-direction to 0.6 m/s throughout the domain to represent the steady flow. The parcels of the packed bed are then inserted at their respective positions. The velocity at the inlet is specified normally to the boundary, while the top boundary and outlet are set to outflow boundary conditions. The boundary conditions of the side walls are set to be non-slip and adiabatic.

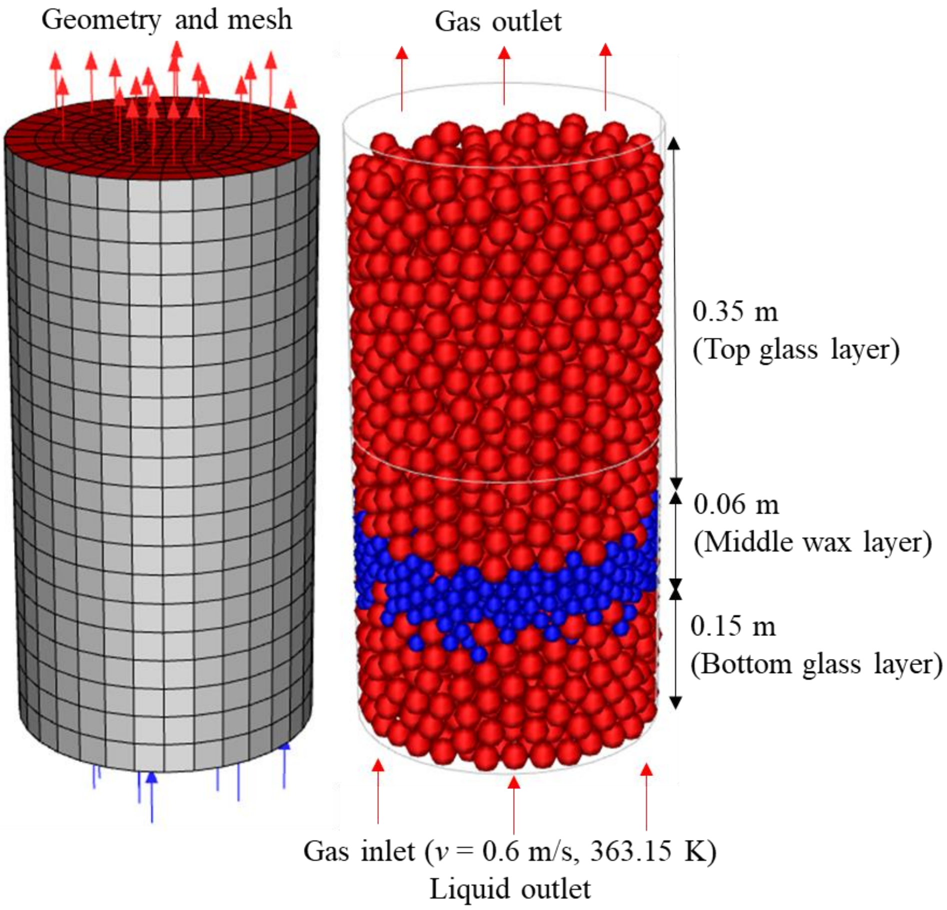

Figure 5.1. Geometry, mesh and packing conditions of wax (blue spheres) and glass (red spheres) parcels before melting in a cylindrical reactor. Top (height = 0.35 m) and base (height = 0.15 m) layers consist of glass spheres, while the middle (height = 0.06 m) layer consists of wax spheres.

Table 5.1 shows the properties of the air, liquid wax, glass and wax parcels and DEM parameters used in the simulations. Due to the melting and continuous change in diameter of the wax particles, the ratio of the collision timestep to the DEM timestep decreases over time. The spring constant has been chosen such that the initial collision time is at least 5-10 times the DEM timestep. This is to ensure that the collision timestep is much larger than the DEM timestep during the melting process in order that the proper resolution of the collision process can be achieved. Contact heat transfer between particles was not accounted for primarily because the software does not have that functionality. Nevertheless, although it would be more scientifically accurate to include the contact heat transfer between particles generally, in this case the thermal gradient within the wax layer itself is very small (~5 K) compared to the temperature difference between the heated air and wax particles. Thus, the heating of surface layer of the wax particles for melting is dominated by the heat transfer from the forced air convection with higher temperatures. The UDFs from CD-MELT are connected to Fluent for the following purposes: (i) the specification of wax parcels' properties during the melting process, (ii) the stipulation of source terms to the fluid phases, (iii) the implementation of drag forces on the liquid phase from the gas and solid phase, and (iv) the removal of liquid from the bottom surface of the reactor.

In the simulations, air is introduced continuously and evenly over the bottom surface at the velocity of 0.6 m/s and temperature of 363.15 K, based on the experimental conditions [151]. The simulated pressure, averaged over the surface of $y = 0.05$ m, is recorded over time for comparison with the experiment results. The total mass of the solid wax in the reactor is also outputted at a regular time interval to assess the melting rate of the wax. As mentioned previously, the air inside the reactor is allowed to escape at the top, while the liquid wax is removed once it reaches the bottom surface, thus there is no accumulation of the liquid wax in the domain.

5.2.2 Transient profile of gas and molten liquid in packed bed

The numerical results of CD-MELT are then compared with the experimental and predicted results from the literature. Figure 5.2 plots the mass of the solid wax over time, as well as the surface-averaged pressure at $y = 0.05$ m. As shown in the figure, the transient reduction in mass due to melting is not constant but is slower in the initial and end phases. This is due to the longer time taken to heat and melt the wax in the initial phase, as different positions of the wax particles in the reactor have slightly different melting rates. The non-isothermal melting nature of the wax also directly contributes to a decrease in the convective heat transfer to the wax when the temperature difference between the air and wax decreases. Hence, there is a decrease in melting rate towards the end of the melting process.

A number of variables can be employed to evaluate the different stages of the melting process [99, 151]. Firstly, the transient pressure measurements at the bottom of the bed provide important information on the softening and melting process, for the present case of the melting of a single and cohesive wax layer. In both the experiment of Chew et al. [151] and the simulation of Yang et al. [99], the pressure drop across the bed was observed to be stable initially at the base pressure, then increased rapidly to peak at approximately 30 mbar, and finally declined slowly back to the base level. In our simulation, however, the pressure remains consistent throughout the melting process instead at around 7 mbar which is similar to the base pressure in the experiment of Chew et al. [151]. The difference occurs because the softening process of the wax is not simulated in our study.

Table 5.1. Properties of the air, wax, and glass parcels and DEM parameters used in the simulation.

Parameter	**Air**	**Wax**		**Glass**
		Liquid	Solid	
Density (kg/m^3)	1.2	770	900	2500
Diameter (m)	-	$\left(\frac{6\alpha_l V_{cell}}{\pi}\right)^{\frac{1}{3}}$	0.011	0.017
Heat capacity (J/kg·K)	1000	3100	2500	840
Thermal conductivity (W/m·K)	0.0262	0.12	0.25	1.05
Dynamic viscosity (kg/m·s)	1.85×10^{-5}	$0.001e^{-4.25+\frac{1790}{T}}$	-	-
Melting range temperature (K)	-	-	320.15 – 347.15	-
Particle-Particle spring constant (N/m)	-	-	1500	6000
			Wax-Glass:1500	
Particle-Wall spring constant (N/m)	-	-	1500	2000
Normal restitution coefficient, η	-	-	0.8	0.9
			Wax-Glass: 0.8	

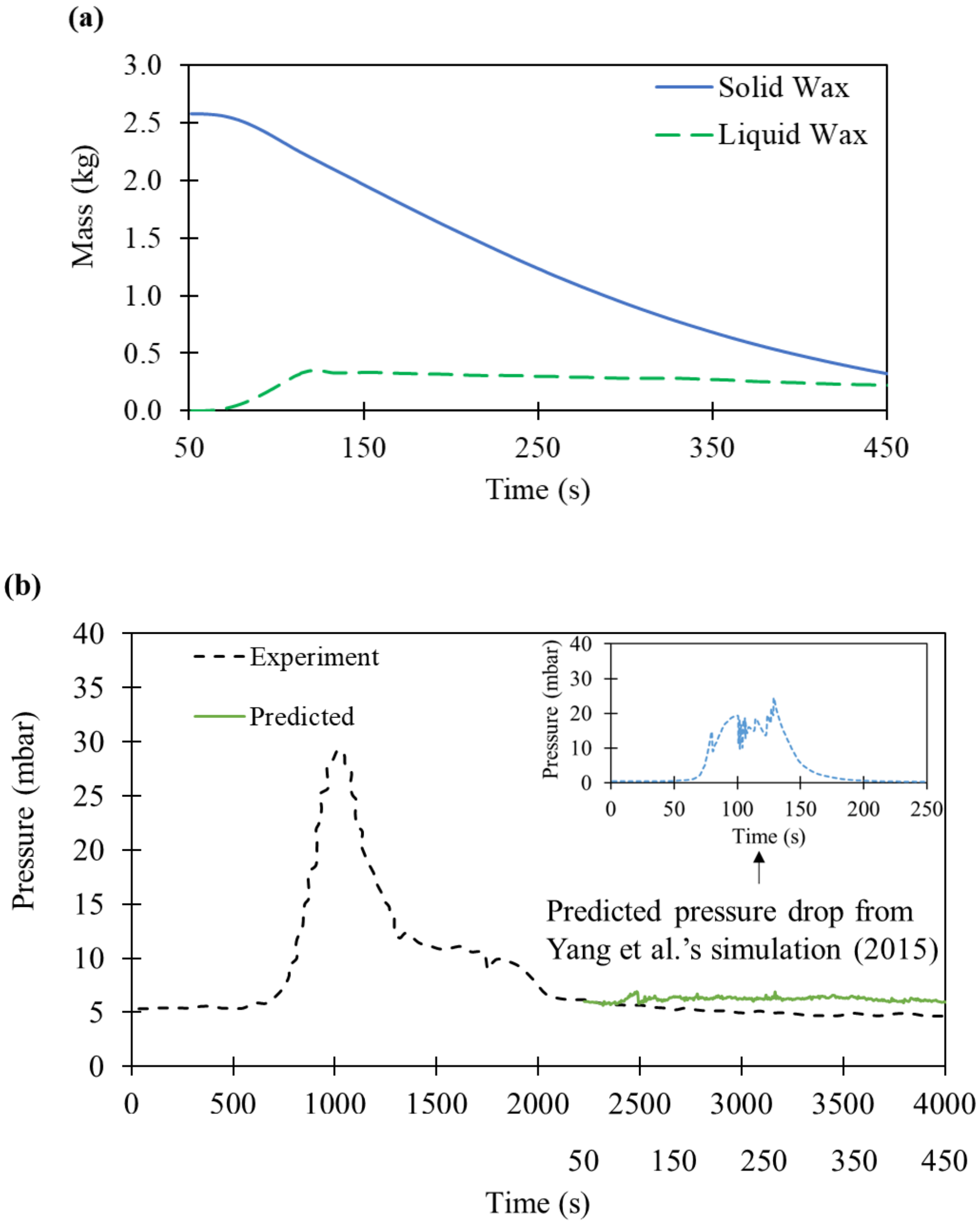

Figure 5.2. Development of wax melting over time: (a) Predicted total mass of solid and liquid wax in reactor, and (b) Predicted surface-averaged pressure at $y = 0.05$ m (Height of point A1 in Chew et al.'s experiments) over time (secondary x-axis) compared to measured experiment pressure over time (primary x-axis) [151]. Yang et al.'s predicted pressure drop over time in insert [99].

During softening, the porosity of the wax layer reduces, and the particles are packed closer together with larger overlap, which in turn reduces the available void fraction for the gas to flow through. The reduced void fraction in turn increases the pressure drop across the bed and reduces the gas flow. Once the melting process initiates and the melted liquid begins to detach from the solid, the gas is able to flow better and the pressure would decrease and stabilise. This explanation is further corroborated by Yang et al.'s predictions of the temperature in the wax layer over time when the pressure increases [99]. In their study, they simulated the softening over the temperature range of 307 to 320 K before the melting process and obtained the increase in pressure drop directly corresponding to the time period and temperature range when the wax layer was undergoing the softening. Nevertheless, CD-MELT correctly predicts that the pressure drop would be consistent at the base level after the melting initiates, which was observed in both Chew et al. [151] and Yang et al. [99].

Another interesting observation is the timescales of the entire melting process in the numerical simulations are much shorter than the experimental observations. In the numerical study of Yang et al. [99], the softening and melting process took less than 250 s, while in our study, the melting process alone takes about 500 s. Both times are much shorter than the entire experimental duration in Chew et al. [151] which was more than 3000 s. The time difference could be attributed to a wide variety of reasons, such as boundary heat loss in the experimental setup during the heating process, time taken to raise the particle temperature before the softening, effects of particle shape on the heat transfer [152], the assumption of uniform particle temperature, etc. In the experiment, a significant amount of time from $t = 0$ s was spent on the slow heating up of the experimental setup as well as the softening of the wax particles, although there was no information on the heating process given in the paper. Hence, we are not able to simulate this softening time duration in details and assume the particles were heated up uniformly before melting. Most importantly, the focus of the study is on the melting process of the packed bed and not the softening, hence we align the time axis to the corresponding time period in the experiment when melting occurred. In particular, we note that the time taken for the melting process in our study is approximately twice that of Yang et al. [99]. We attribute the increase in time taken to our inclusion of latent heat during melting in CD-MELT, which was not considered by Yang et al., which we deem to be important and necessary. This is because the heat gained by the wax particle is partitioned into two main purposes: (i) the sensible heat to raise its temperature and (ii) the latent heat for its melting. However, the relative significance and proportion of latent heat compared to sensible heat is strongly correlated to the latent heat of fusion, heat capacity of the solid, and melting temperature range.

For the present case, the latent heat required to melt a wax particle is approximately 2.5 times the sensible heat to heat the same particle over the melting temperature range. Thus, neglecting the latent heat would result in all the heat gained channelling into sensible heat, leading to a much faster increase in the particle temperature and higher melting rate. Finally, the presence of the molten liquid in the bed provides a small resistance to gas flow contributing to the additional pressure drop across the bed on top of the base level, which is part of the liquid holdup phenomena. This is why after the melting is initiated, the pressure drop across the bed increases by a small extent in our study (t = 100 s onwards) due to the melted liquid present in the packed bed, which is consistent to the experimental observation. On the other hand, the liquid phase was not simulated in the model by Yang et al., thus their pressure drop decreased to the base level as soon as the melting process was initiated.

Figure 5.3 provides an illustration of the predicted liquid volume fraction profile over time by CD-MELT from *t* = 70 s to 270 s. Figure 5.3(a) shows the horizontal cross-sections at the bed height of 0.15 m, while Figure 5.3(b) illustrates a vertical cross-section of the centre of the reactor. With the ability of CD-MELT to track the melted liquid flow through the bed, the simulated results provide insights on how the multiphase melting processes are taking place inside the reactor. It is observed that from *t* = 220 s to *t* = 270 s, the volume fraction of liquid does not change significantly, which implies a quasi-steady state in liquid distribution within the reactor. The top and side view observations in Figure 5.3 show that there is a biased accumulation of liquid near the walls of the reactor in this case, which would lead to faster heat transfer and higher melting rates in this region. This could be attributed to the fact that more gas channels are predicted to be formed near the reactor walls in the simulation results, as shown in Figure 5.4, which is consistent with the multiple experimental observations [151] that major gas channels were noticed to form adjacent to the wall. As the gas channels are crucial for determining flow through the bed and regions of increased melting, incorporating the softening model would make the simulation more accurate. Additionally, the liquid volume fraction throughout the bed is rather uniform in terms of height, suggesting that the liquid faces resistance from the solid particles in the packed bed, and allows for observation and estimation of the liquid flow from the outlet.

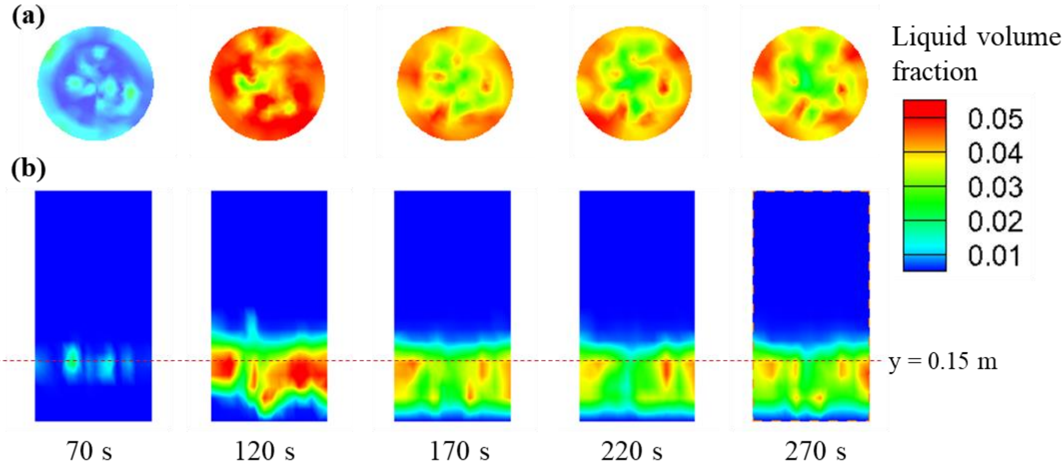

Figure 5.3. CD-MELT model prediction: Liquid volume fraction in reactor at t = 70, 120, 170, 220, and 270 s; (a) y = 0.15 m (top view) and (b) centre of domain, z = 0.0 m (side view).

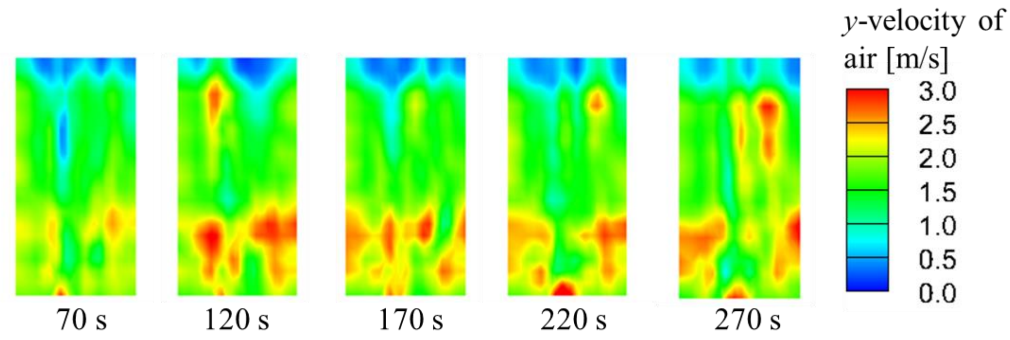

Figure 5.4. CD-MELT model prediction: Distribution of y-velocity of air in reactor at t = 70, 120, 170, 220, and 270 s at centre of domain, z = 0.0 m (side view).

Overall, our results show that the new CD-MELT with coarse graining is able to simulate well the melting of the wax layer in the packed bed in this case. In addition to the pressure loss, our simulations have also provided additional insights into the heat transfer processes with melting, as well as the quantitative simulation results yield the predicted distribution of the liquid volume fraction and the gas channels through the packed bed. These predictions on the locations of gas channels agree well with what were observed in the experiments. The ability to model the melting and subsequently track the flow of melted liquid through the packed bed provides a distinct advantage of CD-MELT over the existing CFD-DEM models in the assessment of the reactor performance during the quasi-steady operation. We note that the initial softening process is not included at this point. However, in engineering applications involving large melting packed bed reactors such as gasifiers for solid waste gasification, the feed waste is typically fed continuously into the reactor and the feed gas is typically supplied continuously into the reactor. In such cases, the size of feed particles is typically small and their interaction is normally very dynamic, and the softening process does not normally play a significant role in affecting the operating conditions compared to the melted liquid flow through the packed bed.

5.3 Coarse-graining and validation

Coarse graining (or parcel modelling) is a method that has been commonly used in CFD-DEM simulations [153]. A representative grain (or parcel) is used to model the collective behaviour of a group of particles with similar properties [87, 89, 154] as shown in Figure 5.5. With this approach, the parcel is tracked instead of the particles, with collision forces being modified to represent the collisions of the parcels instead of the particles. Each parcel is assumed to be non-porous, i.e. no gas flow within the parcel [153]. Additionally, particles with the same diameters are grouped into parcels, with separate parcels representing different particle diameters. However, all the parcels can be represented with a single parcel diameter, allowing for a larger mesh and particle timestep, while still accounting for the effect of particle size on melting rate. Overall, the coarse graining allows for large savings in computational time.

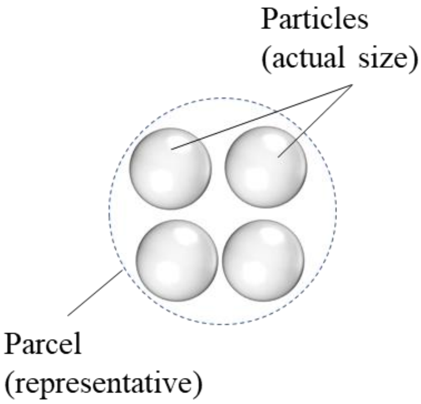

Figure 5.5. Particles in a representative parcel.

Keeping the density of the parcel and particle constant, each parcel is assumed to have an equivalent total mass as the group of particles it represents, and thus a diameter d_{pa} can be set such that the parcel’s volume is equivalent to the sum of the particles’ volume. For each parcel, the number of particles per parcel, N_{p}, is calculated based on their diameters as follows:

$$N_{\mathrm{p}} = \frac{V_{\mathrm{pa}}}{V_{\mathrm{p}}} = \left(\frac{d_{\mathrm{pa}}}{d_{\mathrm{p}}}\right)^3 \tag{55}$$

where the subscript ‘p’ and ‘pa’ refers to the particle and parcel respectively, V is the volume and d is the diameter.

When adopting the coarse graining approach, the calculations of melting rate, source terms, and heat transfer for the parcel versus those for the particle need to be carefully considered and treated accordingly. Larger parcels might cause instabilities from the source terms to the fluid phases, affecting the packing dynamics or predicting a slower than actual melting rate due to decreased surface area. Here, to evaluate the sensitivity of the developed melting approach to coarse graining, we investigate the effect of coarse graining on melting rate with a hypothetical scenario of three particles and one parcel, as well as the effect on the particle packing in a fixed bed. The source terms to the fluid phases as written in Section 3.3 and 3.4 are calculated carefully using the original particle mass, diameter, and surface area, then scaled by N_p within the UDFs. The effect on melting rate is investigated via comparing the predicted total mass over time of three particles with the mass of a single parcel as the melting process takes place under forced air convection. The single parcel has the same initial mass as the three particles, hence $N_p = 3$. In terms of choosing Np for future applications, the guidelines are similar to when choosing particle sizes, i.e., parcel diameters should have a mesh-particle ratio that is not too small, and spring constants chosen appropriately such that collision times are larger than the DEM timesteps, as in Chapter 4. It is also noted that N_p does not necessarily have to be a whole number, allowing for the flexibility of representing particles of various diameters with a single parcel diameter.

A hypothetical scenario is generated to test the effect of coarse graining on melting rate with the 3-particle parcel. The domain is generated based on a cylindrical reactor of diameter 300 mm and height 600 mm from the experimental setup by Chew et al. [151], and is consistent for all the simulations in this study, as shown in Figure 5.1. Three particles of diameter 11 mm, set far apart enough to not have any interparticle interactions, are injected into the domain at different locations.

The properties of the particles and parcel are listed in Table 5.2, with an initial temperature of 318.15 K, solidus temperature of 320.15 K and liquidus temperature of 347.15 K. The density of the particle is assumed to be constant over the melting temperature range, and the mass of the parcel is three times the mass of one particle. The gas inlet is the entire bottom surface, with an inlet velocity of 0.6 m/s and at a temperature of 363.15 K. The walls of the reactor are set to be adiabatic, and the top surface is open and allows gas to escape.

Table 5.2. Physical properties of particle and parcel.

Physical Property	**Particle**	**Parcel**
Initial diameter, d (m)	0.011	0.016
Density, ρ (kg/m^3)	900	900
Specific heat capacity, c_p (J/kg·K)	2500	2500
Thermal conductivity, k_p (W/m·K)	0.25	0.25
Latent heat of melting, h_m (J/kg)	166, 000	166, 000
Number of particles per parcel, N_p	1	3

To assess the effect of coarse graining on the melting rate, three simulations were conducted: (i) the three particles and a DEM timestep of 0.1 ms, (ii) the three particles and a DEM timestep of 1 ms, and (iii) the single parcel with the DEM timestep of 1 ms. Theoretically, the first simulation with the smaller DEM timestep should have the most accurate melting rate and is also used to assess if the melting model is sensitive to the DEM timestep. The mass of each particle, parcel, and the total mass of both solid and molten liquid are then tracked and outputted to a data file every second to compare the melting rate. During the simulations, the melted liquid is accumulated in the domain and not allowed to escape through the bottom surface.

Figure 5.6 presents the results of the hypothetical scenario of three particles versus one equivalent parcel, including the individual mass of the particle or representative particle over time as it melts, as well as the total mass of solid and molten liquid. In Figure 5.6(a), for the particle cases, the particle compared is chosen at the same location, while for the parcel case the mass compared is that of the representative particle used for the melting rate calculations (i.e., same initial diameter as the three particles). From Figure 5.6(a), it is observed that the individual melting rate of particles is higher than that of the melting rate of the representative particle and using a smaller DEM timestep of 0.1 ms does not significantly affect the result (less than 5% difference). The discrepancy in melting rate can be explained by the source terms to the fluid phase being scaled by $N_p = 3$ for the parcel case. Thus, more heat would be absorbed from the immediate fluid cells surrounding the parcel compared to those surrounding the particles, resulting in a lower fluid temperature and slowing down convective heat transfer. However, for cases with densely packed beds, this would be less of an issue as the heat absorption should be more uniform throughout the domain.

Although the DEM timestep does not seem to affect the melting rate of the individual particle, collectively, it seems that when the total mass of solid is compared in Figure 5.6(b), the melting rate of the case with DEM timestep = 0.1 ms is slower than that of the case with DEM timestep = 1 ms. On the other hand, the melting rate for the parcel is almost identical with the collective melting rate of the three particles with DEM timestep = 0.1 ms, which is theoretically the more accurate one. This suggests that the coarse graining approach predicts a result that is close to the average melting rate of the three particles and does not significantly affect melting rate and hence can be used in our model. However, we emphasise that the heat absorption and melting rate must be based on the size of the original particle and not of the parcel to obtain comparable results.

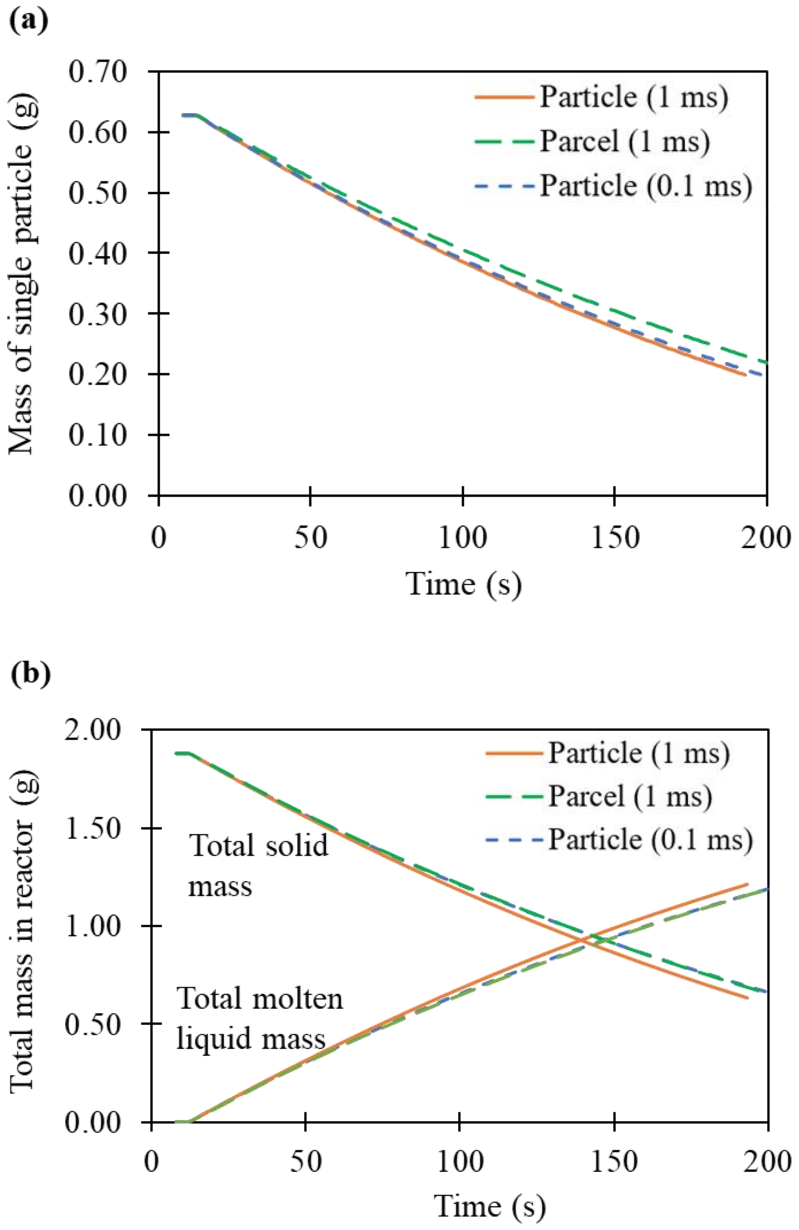

Figure 5.6. Effect of coarse graining on melting rate; Comparison of (a) Mass of individual particle, and (b) Total mass of solid and molten liquid over time with DEM timestep of 0.1 ms and 1 ms for particles and 1 ms for parcel.

Next, to further investigate the effect of parcels on bed packing, in preparation for the application example, three setups (called S1, S2, and S3) are generated to compare the height of each layer in a three-layered packed bed. The heights of the layers are based on the experimental setup by Chew et al. [151], with the bottom layer having a height of 0.15 m and particle diameter of 17 mm, the middle layer with a height of 0.06 m and particle diameter 11 mm, and the top layer with a height of 0.35 m and particle diameter 17 mm. S1 consists of only particles, S2 of parcels (for the 17-mm particles only) and particles, and S3 of only parcels. The details of S1, S2, and S3 are shown in Table 5.3. Due to a lack of information of the mass or number of particles in each layer from the experiment, the particle and parcel numbers are determined assuming a void fraction of 0.325, and then calculating the volume of solids required to achieve that void fraction. The diameter of the parcels, spring constant, and restitution coefficients chosen are chosen subject to constraints such as particle-cell size ratio, DEM timestep and materials, which has been discussed previously [155] and will not be further elaborated here.

Table 5.3. Details of setups S1, S2, and S3 used to compare the effect of coarse graining on bed packing.

	S1 – Only particles	**S2 – Parcels and particles**	**S3 – Only parcels**
Top and bottom layer			
Particle/Parcel Diameter (m)	0.017	0.028	0.028
Total number	9273	2074	2074
Number of particles per parcel, N_p	1	4.47	4.47
Middle layer			
Particle/Parcel diameter (m)	0.011	0.011	0.018
Total number	4107	4107	937
Number of particles per parcel, N_p	1	1	4.38
DEM timestep (s)	1×10^{-4}	5×10^{-4}	5×10^{-4}

The generation of the packed bed is done in the following manner. First, the parcels for the bottom layer are injected randomly into the domain and allowed to settle, then the middle layer in the space above the bottom layer, and finally the top layer above the existing two layers. The simulation is then run for 70 s without the melting model to ensure it reaches a pseudo-steady state in terms of bed packing for the three scenarios S1, S2, and S3 as shown in Figure 5.7.

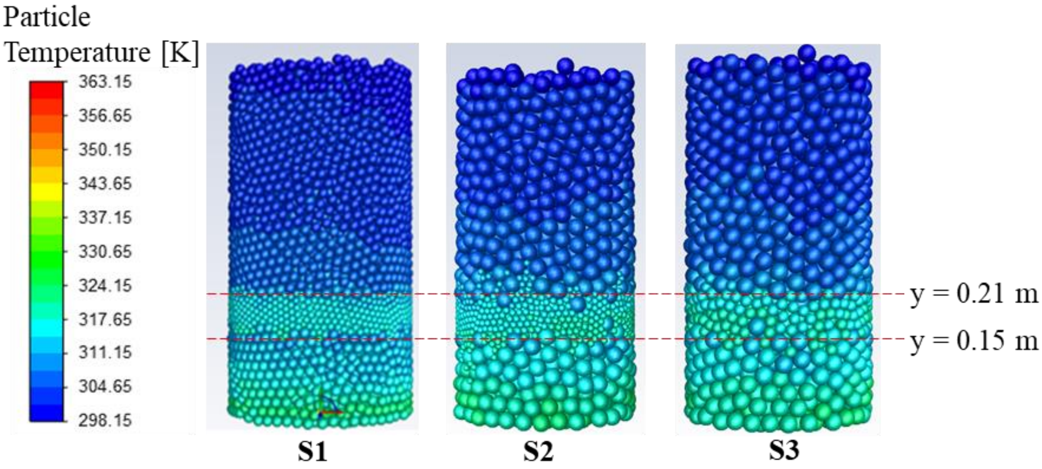

Figure 5.7. Particle/Parcel temperatures and bed packing at *t* = 70 s. (S1: "Only particles"; S2: "Parcels and Particles"; and S3: "Only Parcels". The dashed lines at *y* = ~0.15 and ~0.21 m represent the interface between the top, middle and bottom layers.)

Under the same void fraction and given sufficient time to repack, the total volume of the particles and parcels should be identical. In our case, the linear spring-dashpot model for the particle contact force requires the spring constant to be adjusted. When two parcels collide, it is assumed that all the represented particles undergo the collision at the same time. Hence, the normal contact force is also scaled by a factor of $\left(\frac{d_{\mathrm{pa}}}{d_{\mathrm{p}}}\right)^3$ as derived by Sakai et al. [156]. According to Di Renzo et al. [153], due to the formulation of the collision forces, the restitution coefficient in the particle force collision model does not need to be modified with coarse graining, which we also found to be the case. Overall, it can be observed that the heights of the different bed layers are comparable in Fig. 5, indicating that the modified collision forces by coarse graining are properly accounted for.

To summarise, although the number of DEM particles is not many with 3011 after coarse-graining, it would still take a long time for the simulation to execute due to the detailed Euler-Euler-Lagrangian formulations involved with the requirements of very small time steps. Here, it took 5 days to simulate 500 s in a workstation with 16 nodes × 128 GB with a 2.00 GHz Intel Xeon (E5-2683 v3) processor for a single run with coarse-graining. Without the coarse-graining, the number of DEM particles will be increased to 13380 from 3011, and the computational time step will need to decrease by at least ten times. We estimate that based on experience that the total computational time will then increase to at least 1.5 months for a single run which is beyond our capability. Most importantly, we had carried out a preliminary comparison for the first 70 s and managed to show that the coarse-graining did not affect the bed packing and melting rate significantly, which justified the use of the coarse-graining approach for future uses in large scale gasifiers.

5.4 Comparison between VOF and CD-MELT

Table 5.4 shows the mass conservation equations for the DPM model, VOF model, VOF-DEM model and Eulerian CFD-DEM model such as CD-MELT. As discussed earlier, VOF is a very popular approach for multiphase flow simulations currently, and recently Celik et al. utilised the CFD-DEM approach with VOF representing the gas and liquid phase as a single phase [98]. In VOF, the volume fraction of each fluid is typically computed in every cell, whereby a value between 0 and 1 represents the presence of a fluid interface between one or more fluids, and the volume fraction of all fluids must sum to unity within the cell. The single-phase flow properties, such as velocity and temperature, would then be directly governed by the single-phase momentum and energy equation by the volume-averaged values of density, viscosity and enthalpy.

Many studies had extended the conventional CFD-DEM to VOF-DEM for three-phase flow in various applications, such as slurry flow and solid-liquid mixing [91, 157-159]. In some studies [158, 159], the solid volume fraction was considered as negligible and its effect was not included in the fluid conservation equations, which would not be applicable for melting in a packed bed. Thus, in order to integrate the VOF equations into the CFD-DEM model, an extra equation must be included for the transport of the liquid phase fraction α_{l} as follows [91]:

$$\frac{\partial(\alpha_{\mathrm{f}}\alpha_{\mathrm{l}})}{\partial t} + \nabla\cdot(\alpha_{\mathrm{f}}\alpha_{\mathrm{l}}\vec{v}_{\mathrm{f}}) + \nabla\cdot(\alpha_{\mathrm{f}}\alpha_{\mathrm{l}}(1-\alpha_{\mathrm{l}})\vec{v}_{\mathrm{r}}) = 0 \tag{58}$$

In Celik’s paper, the transport equation included an additional source term on the right-hand side to account for the displacement of fluid by particles. However, the transported term is the liquid phase fraction α_{l} (defined as $\frac{V_{\mathrm{l}}}{V_{\mathrm{f}}}$), rather than the locally averaged phase fraction $\alpha_{\mathrm{f}}\alpha_{\mathrm{l}}$ which is equal to $\frac{V_{\mathrm{l}}}{V_{cell}}$, and is thus inconsistent with the similar VOF model by Jing et al. [91]. Additionally, in Celik et al., the mass conservation equations for the composite gas and liquid phase differ from the composite fluid continuity equation. In comparison, for the Eulerian approach of CD-MELT, the mass is conserved accurately without inconsistency through the conservation of volume fraction.

In the present application example, the direction of the velocity of the air flow is primarily upwards, while that of the liquid flow is downwards. If the VOF-DEM method is adopted, a small liquid volume fraction would result in an upward liquid velocity since VOF represents the air and liquid as a single composite fluid phase whereby the velocity field is shared and solved by a single momentum equation, which would not represent well the melted liquid flow downward through the bed. A finer mesh may better resolve and observe the different flow directions of gas and liquid with VOF, but it is in direct conflict with the DEM’s requirement of a minimum cell size to particle ratio at the same time. An Eulerian CFD-DEM model such as CD-MELT, on the other hand, does not face this challenge as the velocities of each phase are calculated separately, allowing for representation of separate directions for the gas and liquid flows with the use of a coarser mesh.

Finally, CD-MELT requires a comprehensive understanding of the detailed properties of the three phases as well as their interaction for the simulations. Thus, in situations whereby the information is lacking to some extent, the accuracy of CD-MELT would be difficult to assess. At the same time, the VOF method may still be able to yield some gross predictions in such cases as demonstrated in the earlier studies discussed above.

Table 5.4. Mass conservation equations for the simple DPM, VOF, VOF-DEM and Eulerian CFD-DEM model such as CD-MELT.

	DPM [78] (Dilute solid)	**VOF [23, 160]**	**VOF-DEM [91]**	**Eulerian CFD-DEM (DDPM) [119]**
Number of Eulerian phases	1	> 1	> 1	≥ 1
Lagrangian representation of solid phase	Yes	No	Yes	Yes
Continuity equation*	$\frac{\partial \rho}{\partial t} + \nabla \cdot (\rho \vec{v}) = S_\mathrm{p}$	$\frac{\partial \alpha_q \rho_\mathrm{q}}{\partial t} + \nabla \cdot \left(\rho_\mathrm{q} \alpha_q \vec{v}_\mathrm{f}\right) = 0$ $\frac{\partial \rho_\mathrm{f}}{\partial t} + \nabla \cdot (\rho_\mathrm{f} \vec{v}_\mathrm{f}) = 0$	$\frac{\partial \rho_\mathrm{f} \alpha_\mathrm{f}}{\partial t} + \nabla \cdot (\rho_\mathrm{f} \alpha_\mathrm{f} \vec{v}_\mathrm{f}) = S_\mathrm{p}$	$\frac{\partial}{\partial t}\left(\alpha_\mathrm{q} \rho_\mathrm{q}\right) + \nabla \cdot \left(\alpha_\mathrm{q} \rho_\mathrm{q} \vec{v}_\mathrm{q}\right) = S_\mathrm{p}$

*Subscript f – (composite) fluid, q – individual fluid phase (e.g. gas or liquid). $\boldsymbol{\alpha_q}$ represents an arbitrary fluid phase volume fraction and $\boldsymbol{S_\mathrm{p}}$ the source term from the Lagrangian discrete phase (if present).

5.5 Summary

CD-MELT is further extended to three phases (gas, liquid and solid) with non-isothermal melting. It provides the characteristics of the three individual phases, which is superior to the current VOF approaches whereby the fluid phases (gas and liquid) are lumped together in the computational cell and not distinguished. The separation of the three individual phases also allows for the use of a coarser mesh, saving computational time which is usually the primary concern in Euler-Lagrangian approaches. In addition, CD-MELT allows for the consideration of both latent heat and sensible heat in the non-isothermal melting process via the introduction of a particle enthalpy variable, where the melting rate is determined by the balance of heat gained from convection and heat required for melting.

CD-MELT is applied to simulate the non-isothermal melting of wax spheres packed in a single layer in a glass bed subjected to forced air convection with higher temperature, which referenced an experimental setup published in the literature. In this application, the coarse graining approach is adopted to accelerate the computation while reproducing the same melting rate and bed packing, based on theoretical considerations of the source terms and variables for non-isothermal melting. Validation of the coarse-graining approach with CD-MELT is important due to the final goal of using the software as a tool to model melting in large, full-scale gasifiers with a wide distribution of particle compositions and sizes. The predictions of CD-MELT are then compared with published experimental and theoretical studies related to this application. It is found that the latent heats and most importantly the tracking of the melted liquid phase are dominant factors in order to simulate the melting process accurately.

Furthermore, the predictions on the melted liquid movement through the packed bed provides additional insights to the gas channel formations and liquid holdup phenomena.

Chapter 6. Application to gasification

6.1 Overview

The three-phase non-isothermal melting approach for CD-MELT in Chapter 5 was extended to include other chemical processes for gasification simulations. To demonstrate the model capability, CD-MELT is used in this chapter to assess the need for slag recycling for the non-isothermal melting of MSW in a prototype Waste-to-Energy research facility. The simulation encompasses the slagging gasification process for the full fixed bed including chemical reactions and melting of MSW and slag. Comparisons are made for two cases with and without slag recycling, in terms of the slag mass, liquid slag volume fraction, exit gas composition, and temperature distribution in the gasifier. The prediction results show the tracking of the liquid molten slag as it permeates through the packed bed which is crucial to understand the design issues for slag tapping, including potential clogging within the porous media. In particular, the need for slag recycling is demonstrated in this gasifier with the uneven and intermittent slag permeation through the packed bed without the recycling. Finally, the predicted slag outlet temperature is also compared with the published data from an earlier case study for the same facility.

6.2 Application example: Prototype gasifier

In the application example for the prototype gasifier, the solid phase is represented by individual discrete particles, and the conservation equations are solved on a Lagrangian manner for each particle using the DEM [28]. Three types of particles, namely, coal, MSW, and slag were specified to account for the complexity and heterogeneity in the gasification processes of MSW. They can have varied composition, size distribution and varied melting rates, and their momentum fluxes are conserved in terms of accounting for the force balance and collision forces. As mentioned previously in Section 3.2.1, the gas phase is assumed to be a mixture of gases, which are produced and consumed during chemical and physical reactions, and an additional species transport model is included to track the local mass fraction of each species.

6.3 Simulation model

The numerical simulations are performed based on the geometry and operating conditions of the slagging gasification plant for MSW in the Waste-to-Energy Research Facility, Singapore [161]. Figure 6.1 shows the geometry and mesh of the gasifier, as well as the packing conditions. The CFD and DEM time step are chosen to be 0.1 s and 0.5 ms, respectively. The gasifier has a single inlet at the top for the feeding of MSW, coal and solid slag, a single gas outlet for the exit of syngas, and a set of main tuyeres and secondary tuyeres to inject the oxygen-enriched air and ambient air, respectively. The MSW and coal particles form a fixed bed at the bottom of the gasifier, where the coal combustion provides the very high temperature required to heat the MSW, which is mostly gasified and eventually, with the melting of the remaining metal content, producing slag. The plant has a daily treatment capacity of 11.5 tonnes, with the bulk of the MSW feedstock being collected from the nearby campus of Nanyang Technological University. Slag recycling, whereby the molten slag after drainage from the bottom outlet is quenched in a water bath and then returned as feedstock to the inlet of the gasifier, is found to be necessary in order to achieve operational stability. The recycling leads to direct wastage of energy and adds to the cost of the operation and should be minimised. The amount of slag recycling is presently determined empirically based on field experience, due to a lack of modelling tools for assessment.

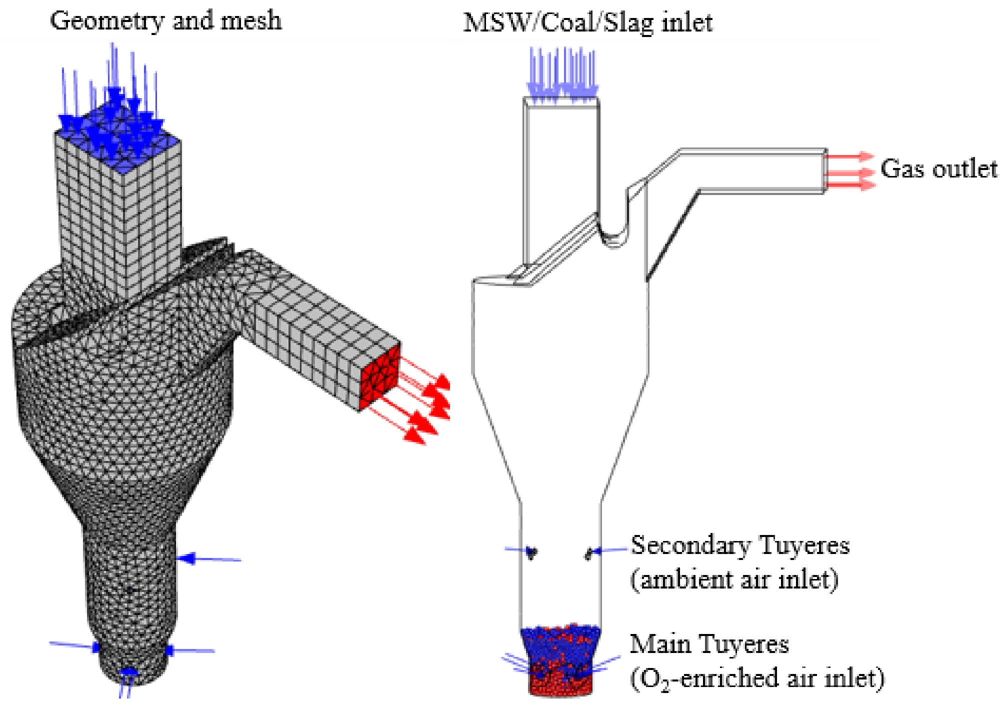

Figure 6.1. Geometry and mesh of gasifier in the Waste-to-Energy Research Facility (WTERF) in Singapore (Isometric and side views). Particle packing conditions of coal (red spheres) and MSW, including solid slag (blue spheres), at t = 5000 s are shown in the right-hand figure.

The physical properties and composition of coal, MSW and slag particles are listed in Table 6.1. The coal particles are injected as auxiliary fuels, and they are assumed to be fully fixed carbon (FC) that can undergo combustion only. On the other hand, the MSW particles (comprised of moisture, volatile matter (VM), FC and ash) can be subjected to vaporization, devolatilization, combustion, and melting sequentially, as mentioned in Section 3.3.2. Finally, the slag particles are assumed to be inert and undergo only heating and melting. Due to the short simulation time and much higher liquidus temperature for coal (~1573 to 2873 K, depending on element composition [162]), it was assumed that only MSW and slag particles undergo melting, with the solidus temperature fixed at 1421 K and the liquidus temperature at 1573 K.

Table 6.1. Properties and composition of solid particles used in the simulations.

Properties	**MSW**	**Coal**	**Slag**
Chemical composition (% weight)			
Moisture (W)	43.71	-	-
Volatile matter (VM) (% wt, dry basis)	79.89	-	-
Fixed Carbon (FC) (% wt, dry basis)	11.72	100.00	-
Ash (%wt, dry basis)	8.39	-	100.00
Density, ρ (kg/m^3) ρ_W = 1000, ρ_{VM}= 400, ρ_{FC} = 430, ρ_{ash} = 2200	Volume-weighted average from each component.	800	2200
Heat capacity, c_p (J/kg K) $c_{p,w}$ = 4200, $c_{p,VM}$ = 4.5099T - 101.4917, $c_{p,FC}$ = -6.85×10$^{-4}T^2$ + 2.09T + 420, $c_{p,ash}$ = -1.95×10$^{-4}T^2$ + 0.644T + 644	Mass-weighted average from each component.	$c_{\mathrm{p,FC}}$	$c_{\mathrm{p,ash}}$
Range of particle diameter (m) Rosin-Rammler distribution	0.01 – 0.07	0.06 – 0.07	0.005 – 0.02
Parcel diameter (m)	0.07	0.07	0.04
Element composition (% weight)			
C	51.81	-	-
H	7.48	-	-
N	1.40	-	-
O	30.92	-	-

Numerous chemical reactions were included for the gasification processes for MSW. They were classified into either homogenous (occurring within the gas phase) or heterogenous reactions (occurring between solid and gas phase). The detailed chemical reactions and kinetics are listed in Table 6.2 [163].

In the simulations, the molten liquid phase and inert slag, are assumed to be inactive in any chemical reactions. For homogenous reactions, the turbulence-chemistry interaction is based on the finite-rate/eddy-dissipation model, where the reaction rates are controlled by both the chemical kinetics and the turbulence mixing. Benzene is used to represent the formation of tar, with cracking into smaller gas molecules. The heterogenous reactions are modelled as particle surface reactions and the rate of reactions are based on Arrhenius kinetics.

The simulation is first performed for an initiation period from $t = 0$ to $t = 5000$ s with slag recycling. The feeding rate of MSW into the gasifier is kept constant at 446 kg/h, and the feeding rate of coal at 50 kg/h [161]. The solid slag recycling rate is kept constant at 130 kg/h. All solids are fed into the gasifier at 300 K. The main tuyere injects oxygen-enriched air at 400 Nm^3/h to maintain the high temperature in the melting zone, while the secondary tuyeres provide ambient air to facilitate the chemical reactions inside the gasifier, such as tar cracking in the freeboard region. The initiation period includes the building up of the coke bed and is run for a comparatively long time (5000 s) to ensure the stability of the chemical reactions and the syngas composition. During this initiation period, simplifications are made by removing the MSW particles when their temperatures escalate to the liquidus temperature (1573 K). In other words, no molten liquid is added to the simulations. At the end of the period, the packed

Table 6.2. Chemical reactions modelled and Arrhenius kinetics.

Chemical Reactions	**Reaction Rates [163]**
Homogenous reactions	
Oxidation	
CO (g) + 0.5 O_2 (g) → CO_2 (g)	$3.165 \times 10^{12} \exp\left(\frac{-1.8\times10^{5}}{RT}\right) [CO][O_2]^{0.25}[H_2O]^{0.5}$
H_2 (g) + 0.5 O_2 (g) → H_2O (g)	$1.08 \times 10^{10} \exp\left(\frac{-1.255\times10^{5}}{RT}\right) [O_2][H_2]$
CH_4 (g) + 2O_2 (g)→ 2 H_2O (g) + CO_2 (g)	$1.3 \times 10^{5} \exp\left(\frac{-2.025\times10^{5}}{RT}\right) [CH_4]^{0.3}[O_2]^{1.3}$
C_6H_6 (g) + 3 O_2 (g) → 6 CO (g) + 3 H_2 (g)	$1.58 \times 10^{15} \exp\left(\frac{-2.026\times10^{5}}{RT}\right) [C_6H_6][O_2]$
Tar Cracking	
C_6H_6 (g) + 5 H_2O (g) → 5 CO + 6 H_2 (g)+ CH_4 (g)	$4.4 \times 10^{8} \exp\left(\frac{-2.2\times10^{5}}{RT}\right) [C_6H_6]$
C_6H_6 (g) + 7.5 O_2 (g) → 6 CO_2 (g) + 3 H_2O (g)	$1.783 \exp\left(\frac{-1.255\times10^{5}}{RT}\right) [C_6H_6]^{-0.1}[O_2]^{1.25}$
Water-gas shift reaction	
CO (g) + H_2O (g) → CO_2 (g) + H_2 (g) (forward reaction)	$2.778 \times 10^{2} \exp\left(\frac{-1.256\times10^{4}}{RT}\right) [CO][H_2O]$
CO_2 (g) + H_2 (g) → CO (g) + H_2O (g) (backward reaction)	$1.263 \times 10^{4} \exp\left(\frac{-4.729\times10^{4}}{RT}\right) [CO_2][H_2]$
Heterogenous reactions	
Particle surface reactions	
$C_{1.088}H_{1.732}N_{0.023}O_{0.361}$ (s) → 0.088 C (char, s) + 0.03 CO_2 (g) + 0.065 H_2 (g) + 0.061 H_2O (g) + 0.08 C_6H_6 (g) + 0.24 CO (g) + 0.25 CH_4 (g) + 0.0115 N_2 (g)	$2.0 \times 10^{11} \exp\left(\frac{-1.8\times10^{5}}{RT}\right)$
C (s) + O_2 (g) → CO_2 (g)	MSW: $5.88 \times 10^{-6} \exp\left(\frac{-3.99\times10^{4}}{RT}\right) [O_2]$ Coal: $4.53 \times 10^{-6} \exp\left(\frac{-3.99\times10^{4}}{RT}\right) [O_2]$
C (s) + CO_2 (g) → 2 CO (g)	MSW: $5.88 \times 10^{-6} \exp\left(\frac{-3.99\times10^{4}}{RT}\right) [CO_2]$ Coal: $4.13 \times 10^{-6} \exp\left(\frac{-3.99\times10^{4}}{RT}\right) [CO_2]$
C (s) + H_2O (g) → CO (g) + H_2 (g)	MSW: $5.0 \times 10^{-6} \exp\left(\frac{-3.99\times10^{4}}{RT}\right) [H_2O]$ Coal: $4.13 \times 10^{-6} \exp\left(\frac{-3.99\times10^{4}}{RT}\right) [H_2O]$

bed achieves a particle composition similar to site observations, while the composition of the exhaust gas and temperature becomes steady.

After the initiation period, the full CD-MELT is then used to assess the need for slag recycling, and the melting from the recycled solid slag or MSW particles are now added to the liquid molten slag phase. Two simulations are performed, the first one with the continuation of the slag recycling while the other with the stoppage of the recycling. Both simulations are conducted for a period of 600 s from t = 5000 s to t = 5600 s, when the slag flow reaches a quasi-steady state. The molten slag is removed via UDF from a single cell located at the side wall and bottom of the reactor, which represents the slag outlet. In the real gasifier, thermocouples are used to measure the gas temperature at the upper, middle and lower parts of the furnace, as well as the exit gas outlet [161]. The temperature of the slag at the outlet is also measured with an infrared thermometer, and these temperature measurements are compared with the predicted results.

6.4 Effect of slag recycling on slag flow through packed bed

The following section compares the CD-MELT results for the two cases: with and without slag recycling. Figure 6.2(a) illustrates how a sample MSW particle changes in mass and temperature over time during this period inside the gasifier, while the liquid, volatile, and char mass fractions are shown in Figure 6.2(b).

During vaporization, the MSW particle undergoes a linear reduction in mass while its temperature remains constant at approximately 373 K. The evolved water vapor is added to the gas phase. After its liquid fraction decreases to zero, devolatilization occurs. Volatile gases are emitted from the particle surface, added to the gas phase as individual species, and the particle temperature increases rapidly. When the devolatilization is completed, combustion and pyrolysis occur where the char fraction is consumed, and the particle temperature continues to increase steadily. Upon reaching the solidus temperature, the particle begins to melt and the solid particle mass reduces. The char fraction decreases rapidly upon the initiation of the combustion-melting. The particle is finally removed when the mass loss fraction exceeds 0.95 which occurs at a temperature of 1517 K as shown in Figure 6.2(a).

To examine the need for slag recycling, the liquid slag flow through the bed is tracked at intervals of 100 s. Figure 6.3 shows the liquid volume fraction at the vertical cross-section of the centre plane (z = 0 m) as well as the horizontal cross-section within the packed bed at y = 0.25 m. The view plane is focused on the bottom packed bed of the gasifier for a clearer comparison. In both simulations, the liquid molten slag accumulates in and permeates through the bed over time. After reaching the slag outlet located at the bottom right corner in centre plane, z = 0.0 m, the liquid slag is then removed via UDF.

With slag recycling, the simulation results (Figure 6.3(a)) show that the distribution of molten slag is relatively uniform within the packed bed with the formation of a single horizontal layer. In contrast, the distribution is uneven without the slag recycling (Figure 6.3(b)), and pockets of accumulation with higher molten slag density can be observed, especially around the front tuyere. This accumulation diminishes the functioning of the packed bed in processing the MSW particles due to the lower temperature of the molten slag compared to the bed media, and the slag tapping would become challenging, which corresponds to the field experience from the plant operator that slag recycling is required to mitigate the process disruption.

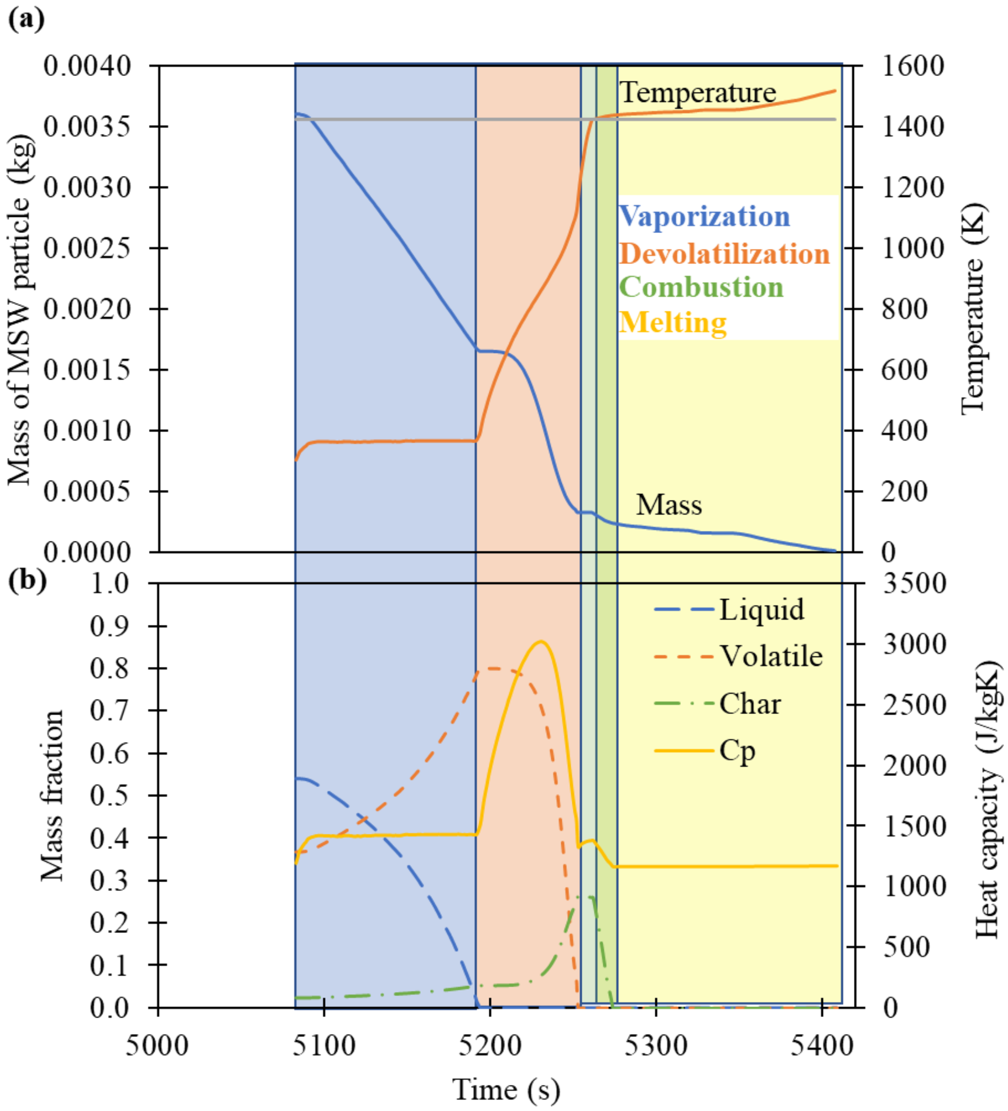

Figure 6.2. Predicted process and lifetime of a sample MSW particle in the gasifier: (a) temperature and mass over time, and (b) heat capacity and liquid, volatile and char mass fractions. The colored zones represent the physical and chemical processes occurring in the particle at any one time. The grey line represents the solidus temperature of MSW at 1423 K.

The predictions of solid, liquid, and total slag mass, as well as the slag temperature at the outlet, are plotted in Figure 6.4 with and without slag recycling.

In Figure 6.4(a), the slag temperature at the outlet is nearly the same for both cases from t = 5400 s onwards, with predicted average temperature for the slag recycling being 1564 ± 33 K, compared to 1562 ± 20 K without slag recycling. The predicted temperature is slightly lower than what is observed at the prototype gasifier of 1638 ± 43 K [161]. This can be attributed to the values of solidus and liquidus temperature for the MSW and slag particles, which differ significantly but are assumed to be similar in CD-MELT as the first approximation.

In addition, other factors not considered in the simulations, such as the ash fusion temperature of coal, heat loss from the boundary wall, and thermal conductivity of slag, can all have little effect on the slag outlet temperature. Comparing the predicted mass of solid and liquid slag in Figure 6.4(b), it is observed that the liquid slag is generated at a higher rate initially without slag recycling, but the rate of liquid slag production tapers off and eventually reaches a similar mass as the slag recycling case. This can be attributed to the fact that since the recycled slag is injected at 300 K, some of the energy in the gasifier is used to heat and melt the injected solid slag; the temperature of the gasifier is thus lower leading to a lower initial melting rate.

The area-averaged temperature of the gas mixture is recorded at different heights within the gasifier over a period of two minutes. The results are compared with the published data [161] in Figure 6.5. For the packed bed, the gas temperature is the highest at the bottom due to the charcoal combustion enhanced by the oxygen-enriched air, while the temperature decreases towards the surface (y ~ 1.0 m) due to the endothermic reactions of vaporization and devolatilization.

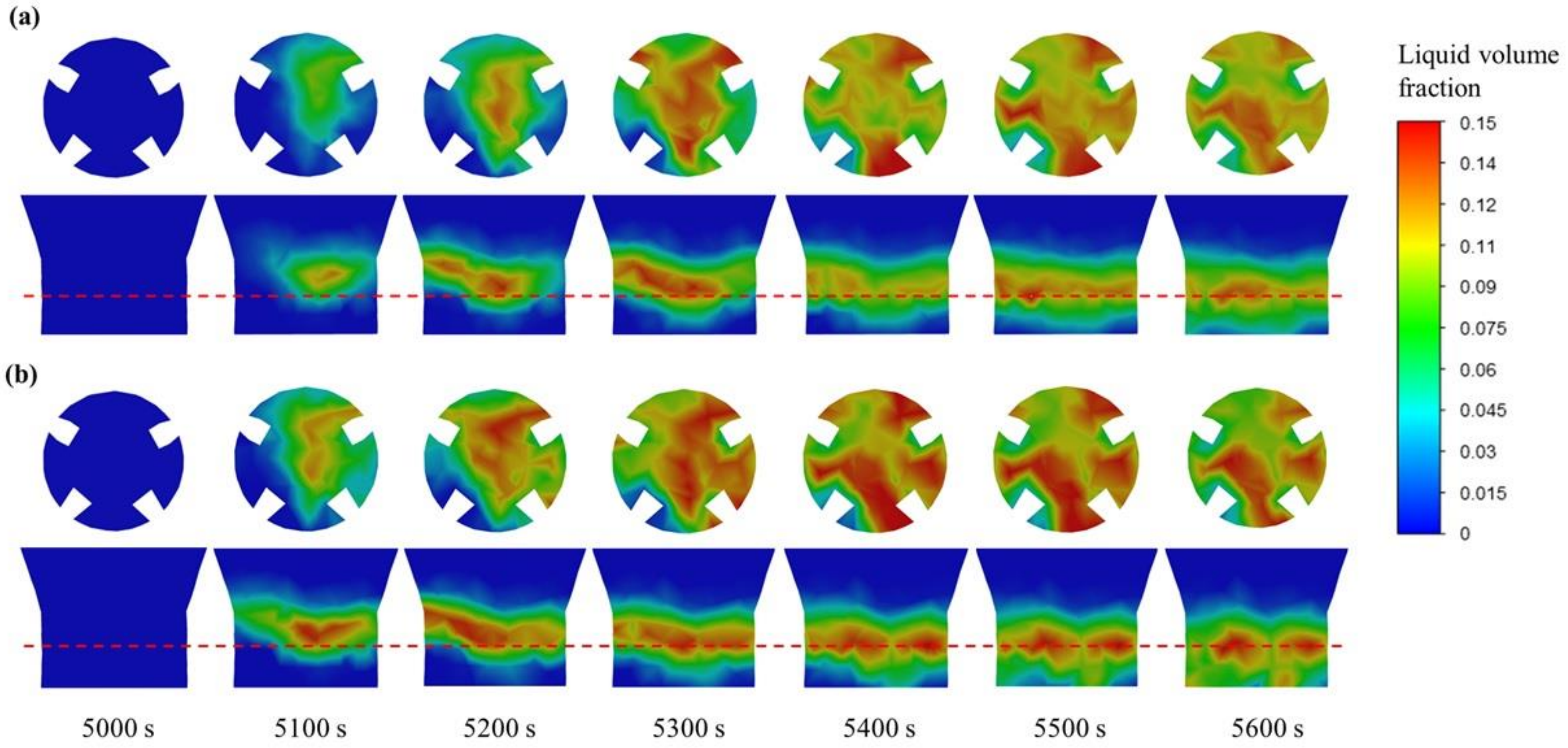

Figure 6.3. CD-MELT model prediction: Liquid slag volume fraction in gasifier at 100 s intervals from *t* = 5000 s to *t* = 5600 s, at *y* = 0.25 m (top view, position indicated by red dotted line) and centre of domain *z* = 0.0 m (side view), and *y* < 0.8 m; (a) with slag recycling, and (b) without slag recycling.

In general, the case with slag recycling has higher temperatures (difference of ~ 60 K) in the freeboard and fixed bed, except for near the bed surface, due to the absorbed heat by the injected slag particles. This is due to the heat retained by the increased amount of solid slag, which is transferred via convection to the air. When comparing with the measured data from the case study [161], the predictions of the gas temperature in the freeboard are significantly higher than the temperatures measured via thermocouples, which could be attributed to the heat loss in the gasifier through the inlet that was not accounted for in the simulations.

The simulated exit gas composition and temperature are plotted in Figure 6.6. The values in the figure represent the area-weighted average of the *y*-*z* vertical cross-section at the gas outlet. The results in the first 200 s, from $t = 5000$ s to $t = 5200$ s, show large fluctuations in the syngas composition with slag recycling, which can be attributed to the increase in H_2. As discussed above, the slag recycling could cause a lower temperature in the gasifier, favouring the forward water-gas shift reaction which is mildly exothermic. Nevertheless, at the quasi-steady state, the exit gas composition is no longer significantly affected by the slag recycling, as the solid slag does not take part in any chemical reactions.

As mentioned previously in Section 3.3.3, there have been some challenges and instability issues when developing the combustion-melting model and implementing it into an existing simulation. The challenges mainly revolve around determining corrective source terms into the gas phase, the removal of the existing particles, and the uncertainty caused by a temperature and composition-dependent specific heat capacity. Hence, the simulation is unable to continue past

5600 s and the focus of the results is the comparison of the case study with and without slag recycling, rather than the site observation. As of now, more work is still required to improve the model.

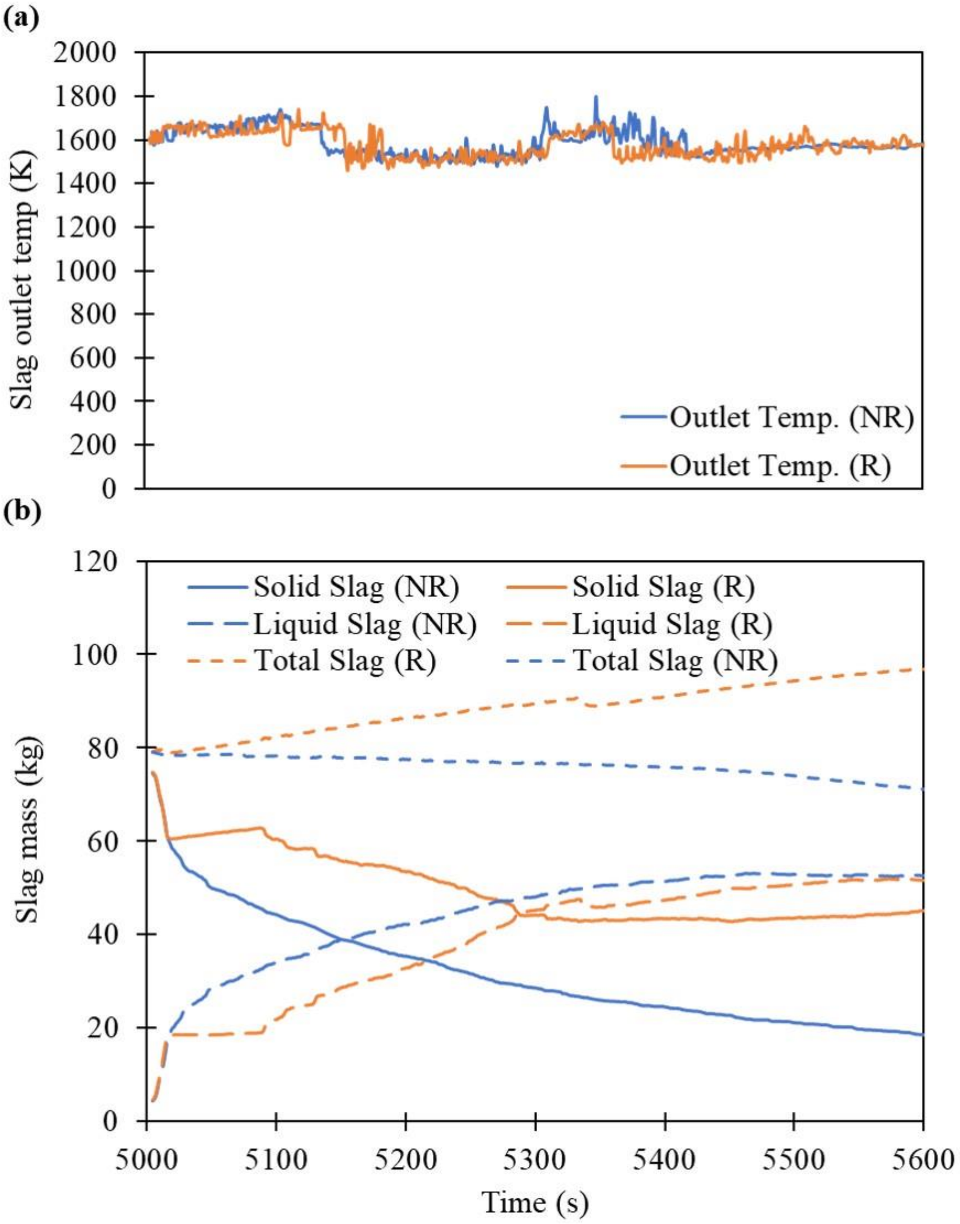

Figure 6.4. CD-MELT model prediction: Predicted slag profile in reactor with (R) and without (NR) slag recycling: (a) Outlet temperature of slag, and (b) mass of solid, liquid and total slag in reactor.

6.5 Summary

CD-MELT is extended to three-phase, non-isothermal, simultaneous combustion and melting in this chapter. The improved CFD-DEM model can be used for simulating multiphase flows with reactions, particularly in engineering applications with significant volume fractions of solid and liquid and with solid melting. It is especially useful for cases where the solid particles are separate or have different properties and melting rates, such as in mixed wastes gasifiers. Particularly, CD-MELT is applied to simulate the operation of the slagging gasification plant for MSW in the Waste-to-Energy Research Facility, Singapore. The simulation results agree well with the measurements from the facility, including the temperature of the slag at the outlet, exhaust gas composition, and liquid slag mass within the gasifier at a quasi-steady state (with deviation of less than 10%). The results also show that the distribution of the liquid slag within the packed bed is more uniform with slag recycling, which provides a plausible explanation for the operators' experience as to why slag recycling is important for process stability. Thus, the present study shows that CD-MELT can be used to assess the need as well as quantity of slag recycling, which is determined solely through empirical experience for MSW gasifiers up to now. Hence, it can act as an effective tool to aid the design and optimisation of full-scale gasifiers for MSW in the future. However, we note that there remains a significant difference between the predicted and observed temperatures of the gas phases in the freeboard region which can be attributed to the possible air exchanges (and heat losses) through the inlets as well as difficulty of implementing the corrective energy source term to the gas phase. Further improvement on the modelling approach and more case studies of field applications are thus still necessary in the future.

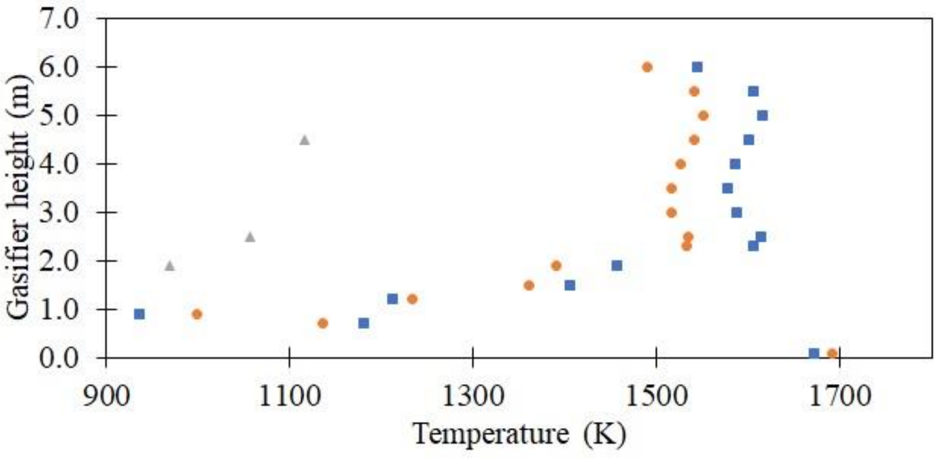

Figure 6.5. Comparison of predicted area-averaged temperature of gas mixture along the gasifier height (■: with slag recycling, and ●: without slag recycling; ▲: site observations).

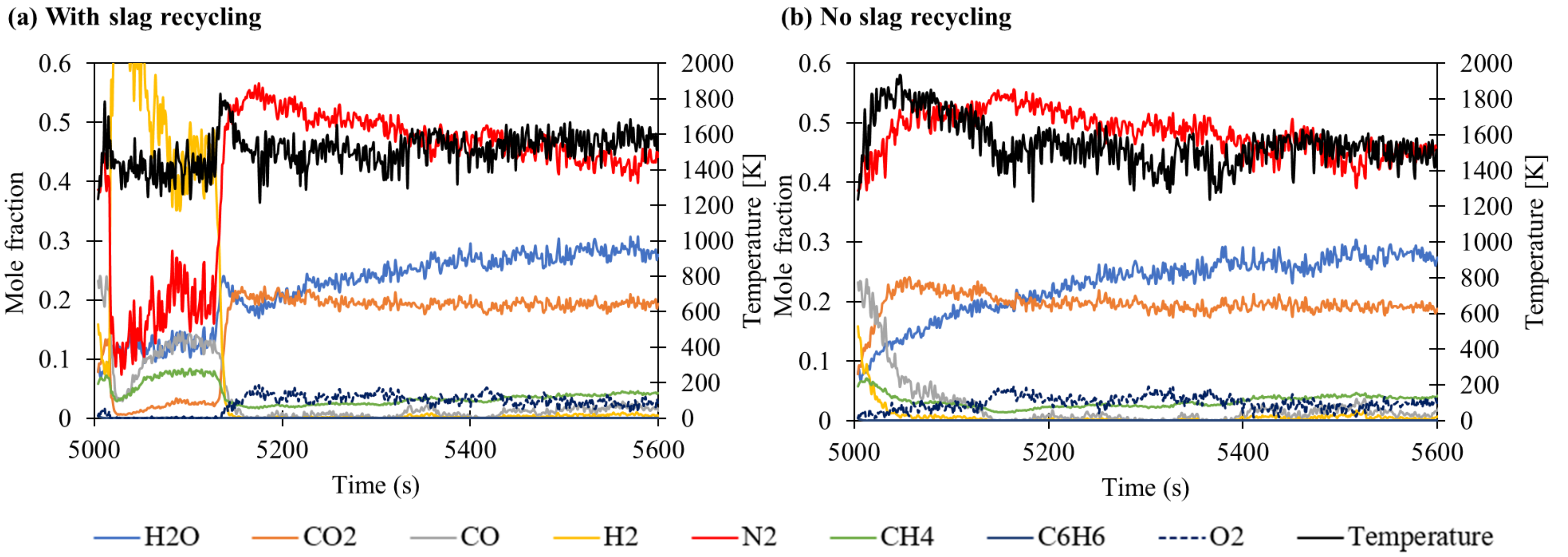

Figure 6.6. CD-MELT's predictions for exit gas composition in terms of mole fraction for H_2O, CO_2, CO, H_2, N_2, CH_4, C_6H_6, and O_2, and temperature over time: (a) with and (b) without slag recycling.

Chapter 7. Conclusions and recommendations

7.1 Conclusions

The study aims to develop a numerical modelling tool that includes the phenomenon of melting in multiphase flows for high-temperature slagging gasification and other applications. A CFD-DEM approach, CD-MELT, was established to be used in different scenarios involving melting and liquid flow in packed beds, such as isothermal melting, non-isothermal melting, and gas-solid reactive flows with non-isothermal melting. Additional insights into computational particle-fluid modelling have been gained. The main conclusions are listed as follows.

- An isothermal melting approach for two-phase flow was first developed to model the melting of a single particle, and subsequently in a packed bed of ice spheres flowing under warm water convection. With the developed approach, the changing of mesh-particle size ratio does not significantly affect stability of the runs, allowing for a coarser mesh. Lastly, smaller values of the spring constant and restitution coefficient in the linear-spring dashpot model for DEM collisions were found to be satisfactorily accurate, while facilitating for a larger DEM timestep, which ultimately provides savings in computational costs. To ensure that particle melting is able to be modelled as the particle size reduces, it is recommended that the spring constant and damping coefficient be set such that the estimated initial collision time, at the start of melting, should be at least 15 times the DEM timestep.

- The approach was then extended to three-phase flows with non-isothermal melting, allowing for the tracking of the liquid phase through the packed bed. Compatibility with coarse-graining was also evaluated and validated via comparison of the melting rate and bed packing, which was important to accelerate computational runs for the targeted objective of use in full-scale gasifiers. In particular, the use of coarse-graining allows the use of one parcel diameter to represent a range of particle diameters, as long as the source terms to the liquid and gas phases are modified correctly, allowing for a coarser mesh, as long as the particle-mesh ratio is suitable. Insights into gas channel formation and liquid flow through the packed bed were also observed through visualization of the gas velocity and liquid volume fractions.
- The approach was then applied to a prototype gasifier and modified to include simultaneous combustion and melting, including the full gasification processes and homogenous chemical reactions. The need for slag recycling within the facility was assessed and determined to be effective for use in design and operation of full-scale gasifiers.
- For the cases analyzed, the Gidaspow drag model and the representation of the liquid phase via an assembly of droplets were determined to be sufficient to represent drag force interactions in the three-phase flow, even when it is applied between each pair of phases. The diameter size of droplets in the liquid phase was deemed to be important and was calculated in a simplistic manner, assuming one spherical droplet per cell volume. This assumption is suitable for cases with low liquid volume

fraction, but further investigation is required and modifications are required to represent liquid phases at higher volume fractions.

7.2 Recommendations

The main focus of this study was on the purpose of modelling melting in packed beds and subsequent liquid flows, with targeting at large-scale gasification facilities. Hence, some assumptions were made to simplify and accelerate computational runtimes. For better accuracy in simulation of the solid-liquid transition stage, future work on the modelling of the softening process is recommended. This could be done through modifying the DEM collision models and contact forces, prior to the implementation of the melting model. Rather than using a spherical shape throughout, the shape of the particles could also be modified during the softening to consider the change in particle surface area and particle-particle interactions. For applications where a cohesive layer is formed and porosity through the bed is decreased, consideration of the softening process would be useful.

Due to the limitations of the software used, particle-particle heat transfer was not considered. Future work on implementing simple particle-particle heat transfer is recommended, especially for applications where the bed is relatively stagnant, there is a large thermal gradient within the bed, or the particles are large. The lack of particle-particle heat transfer could possibly reduce the melting rate to be lower than the actual rate, which would in turn lead to an under-estimation of slag flow rate. Temperature distribution within the particle could also be implemented if the particles are large and heated at a quick rate. However, we note that these implementations would cause an immense increase in computational requirements and should not be undertaken for simulation of large-scale facilities.

Since MSW particles vary widely in reality, especially in terms of shape, size, and composition, further studies on MSW gasification with the use of CD-MELT could incorporate different types of particles to represent MSW more accurately, such as wood, plastic and metal. This would also allow for different melting rates. The current study is an important first step into simulating melting in a packed bed, however much more needs to be done in future studies to improve the simulation of the prototype systems.

Lastly, the liquid phase in this study was represented by an assembly of droplets, which should work well when the liquid fraction is low. When the liquid fraction is high, however, the VOF approach may be better and thus future work is recommended for analysis in combining the different representations.

Appendix A. User-defined functions for coupling with ANSYS FLUENT

A.1. .h files

The following ANSYS Fluent header files are required and must be included in the .c file. These header files are created by ANSYS Fluent.

1. *“udf.h”*

2. *“dpm.h”*

3. *“inttypes.h”*

4. *“dpm_laws.h”*

A.2. .c file (Inert melting model)

The following .c files, written in the C programming language, provides the full list of UDFs for the melting model and drag laws used in this study, along with other functions required such as initializing and defining particle/fluid variables, writing and appending .txt files for post-processing purposes. The particle-specific functions are listed first, followed by the fluid-specific functions. Due to the addition of particle laws and other requirements for particles in Chapter 6, some functions in the code were adapted and some examples are shown in Appendix A.3.

The UDFs for inert isothermal and non-isothermal melting model in Chapters 4 and 5 are listed as follows.

Definitions and initializations of user-defined memory and particle variables, creation of headers for .txt files for recording and post-processing from such variables. For recording of particle data, one .txt file is created per node (total of 16 parallel nodes), while for the source term data, only one file is created at the host node.

```
#include <udf.h>
#include <inttypes.h>
#include <dpm.h>
#include <dpm_laws.h>
#define REMOVE_PARTICLES TRUE
/*Set MELT_TEMP < SOLIDUS_TEMP if isothermal melting [K]*/
/*Set MELT_TEMP > LIQUIDUS_TEMP if non-isothermal melting [K]*/
#define MELT_TEMP 500
#define SOLIDUS_TEMP 320.15
#define LIQUIDUS_TEMP 337.15
/*latent heat of fusion for wax, 334000 for ice [J/kg]*/
#define LATENT_HEAT 166000
/*number of user-defined memory locations (cell variables)*/
#define NUM_UDM 14
/*re-definition of UDM variables to cell for ease of reference*/
#define SOLID_FRACTION(c,t) C_UDMI(c, t, udm_offset)
#define XMOM_IND(c,t) C_UDMI(c, t, udm_offset+1)
#define YMOM_IND(c,t) C_UDMI(c, t, udm_offset+2)
```

```
#define ZMOM_IND(c,t) C_UDMI(c, t, udm_offset+3)
#define ENERGY_IND(c,t) C_UDMI (c, t, udm_offset+4)
#define mass_removed(c,t) C_UDMI (c, t, udm_offset+5)
#define AIR_FRACTION(c,t) C_UDMI(c, t, udm_offset+6)
#define EXIT_LIQ_MASS(c,t) C_UDMI(c, t, udm_offset+7)
#define PL_X(c,t) C_UDMI(c, t, udm_offset+8)
#define PL_Y(c,t) C_UDMI(c,t, udm_offset+9)
#define PL_Z(c,t) C_UDMI(c,t, udm_offset+10)
#define SOLID_DIAMETER(c,t) C_UDMI(c,t, udm_offset+11)
#define ABS_V(c,t) C_UDMI(c,t, udm_offset+12)
#define CUMULATED_EXIT_LIQ_MASS(c,t) C_UDMI(c,t, udm_offset+13)


/*Global variables*/
static int udm_offset = UDM_UNRESERVED;
real solid_capacity = 2500; //2100 for ice
real liquid_capacity = 3100; //4180 for water
FILE *fp;

/*Reserve and name UDMs*/
DEFINE_EXECUTE_ON_LOADING(on_loading, libname)
{
   if (udm_offset == UDM_UNRESERVED)
        udm_offset = Reserve_User_Memory_Vars(NUM_UDM);
   if (udm_offset == UDM_UNRESERVED)
        Message("\nLoaded");
   else
   {
    Message("\n%d UDMs have been reserved by the current library %s",
    NUM_UDM, libname);
    Set_User_Memory_Name(udm_offset,"Solid-Volume-Fraction");
    Set_User_Memory_Name(udm_offset+1,"X-Momentum-Indicator");
    Set_User_Memory_Name(udm_offset+2,"Y-Momentum-Indicator");
    Set_User_Memory_Name(udm_offset+3,"Z-Momentum-Indicator");
    Set_User_Memory_Name(udm_offset+4,"Energy-Indicator");
    Set_User_Memory_Name(udm_offset+5,"Mass-Removed");
    Set_User_Memory_Name(udm_offset+6,"Air-Fraction");
    Set_User_Memory_Name(udm_offset+7,"Exit-Liquid-Mass");
    Set_User_Memory_Name(udm_offset+8,"PL-X");
    Set_User_Memory_Name(udm_offset+9,"PL-Y");
    Set_User_Memory_Name(udm_offset+10,"PL-Z");
    Set_User_Memory_Name(udm_offset+11,"Solid-Diameter");
    Set_User_Memory_Name(udm_offset+12,"Abs-V");
    Set_User_Memory_Name(udm_offset+13,"Cumulated-Exit-Liquid-Mass");
    Message("\nUDM offset for current loaded library = %d",
    udm_offset);
   }
}


/*Initialize UDMs in all cells to 0*/
DEFINE_ON_DEMAND(set_udms)
{
   Domain *d;
   Thread *t;
   cell_t c;
   int i;
   d = Get_Domain(1);
   if(udm_offset != UDM_UNRESERVED)
```

```
      {
         Message("Setting UDMs\n");
         for (i=0;i<NUM_UDM;i++)
            {
               thread_loop_c(t,d) //Loop over all threads in the domain
               {
                  begin_c_loop(c,t) //Loop over all cells in each thread
                  {
                     C_UDMI(c,t,udm_offset+i)= 0;
                  }
                  end_c_loop(c,t)
               }
            }
      }
   else
      Message("UDMs have not yet been reserved.\n");
}

/*Set memory for particle variables*/
DEFINE_INIT(particle_setup,domain)
{
   /*allocate memory for particle variables*/
   if (NULLP(user_particle_vars))
   Init_User_Particle_Vars();
   /*set name and labels*/
   strcpy(user_particle_vars[0].name,"Enthalpy-Account");
   strcpy(user_particle_vars[0].label,"Enthalpy Account");
   /*Used to check if latent heat absorbed is correct*/
   strcpy(user_particle_vars[1].name,"Cumulated-Heat-Absorbed");
   strcpy(user_particle_vars[1].label,"Cumulated Heat Absorbed");
   /*Used to check if mass loss is correct*/
   strcpy(user_particle_vars[2].name,"Cumulated-mass-loss");
   strcpy(user_particle_vars[2].label,"Cumulated Mass Loss");
   strcpy(user_particle_vars[3].name,"Mass-Loss-Fraction");
   strcpy(user_particle_vars[3].label,"Mass Loss Fraction");
   /*Change in temperature from inert heating law for isothermal
   melting*/
   strcpy(user_particle_vars[4].name,"Delta-Temperature");
   strcpy(user_particle_vars[4].label,"Delta T");
   strcpy(user_particle_vars[5].name,"Cumulated-Enthalpy");
   strcpy(user_particle_vars[5].label,"Cumulated Enthalpy");
   strcpy(user_particle_vars[6].name,"Latent-Heat-Source");
   strcpy(user_particle_vars[6].label,"Latent Heat Source");
   /*Change in mass of particle over dpm timestep*/
   strcpy(user_particle_vars[7].name,"Delta-M");
   strcpy(user_particle_vars[7].label,"Delta M");

   #if !RP_HOST /*Create headers for text files, 1 per node, total
   number of nodes = 16*/
   switch (myid) {

   case 0:
      if(NULL == (fp = fopen("node0.txt","a")))
      Error("Could not open file for append!\n");
      break;
   case 1:
      if(NULL == (fp = fopen("node1.txt","a")))
      Error("Could not open file for append!\n");
      break;
```

```
  case 2:
     if(NULL == (fp = fopen("node2.txt","a")))
     Error("Could not open file for append!\n");
     break;
  case 3:
     if(NULL == (fp = fopen("node3.txt","a")))
     Error("Could not open file for append!\n");
     break;
  case 4:
     if(NULL == (fp = fopen("node4.txt","a")))
     Error("Could not open file for append!\n");
     break;
  case 5:
     if(NULL == (fp = fopen("node5.txt","a")))
     Error("Could not open file for append!\n");
     break;
  case 6:
     if(NULL == (fp = fopen("node6.txt","a")))
     Error("Could not open file for append!\n");
     break;
  case 7:
     if(NULL == (fp = fopen("node7.txt","a")))
     Error("Could not open file for append!\n");
     break;
  case 8:
     if(NULL == (fp = fopen("node8.txt","a")))
     Error("Could not open file for append!\n");
     break;
  case 9:
     if(NULL == (fp = fopen("node9.txt","a")))
     Error("Could not open file for append!\n");
     break;
  case 10:
     if(NULL == (fp = fopen("node10.txt","a")))
     Error("Could not open file for append!\n");
     break;
  case 11:
     if(NULL == (fp = fopen("node11.txt","a")))
     Error("Could not open file for append!\n");
     break;
  case 12:
     if(NULL == (fp = fopen("node12.txt","a")))
     Error("Could not open file for append!\n");
     break;
  case 13:
     if(NULL == (fp = fopen("node13.txt","a")))
     Error("Could not open file for append!\n");
     break;
  case 14:
     if(NULL == (fp = fopen("node14.txt","a")))
     Error("Could not open file for append!\n");
     break;
  case 15:
     if(NULL == (fp = fopen("node15.txt","a")))
     Error("Could not open file for append!\n");
     break;
  }
fprintf(fp, "Node Particle-ID Mass[kg] Source-Term[J/0.01s]
```

```
 Density[kg/m3] Diameter[m] Particle-Time[s] Temperature[K]
 Cumulated-Heat-Source[J] Liquid-Fraction Cumulated-Enthalpy[J]\n");
 Message("\nPrinting headers for file...%i",myid);
 fclose(fp);

   if (myid == 0)
   {
     if(NULL == (fp = fopen("sourceterms.txt","a")))
     Error("Could not open file for append!\n");

     fprintf(fp, "Node Total-Mass-Source[kg/s] Total-X-Mom-
     Source[kgm/s] Total-Y-Mom-Source[kgm/s] Total-Z-Mom-Source[kgm/s]
     Total-Energy-Source[J/s] Flow-time[s]\n");
     Message("\nSource terms file created...%i",myid);
     fclose(fp);
   }
   #endif
}

/*Calculate modulus of x%y*/
float dmod(float x, float y)
   {
    return x - (int)(x/y) * y;
   }
```

Particle-specific functions.

Summary: Updating of scalar variables, output of particle data to .txt files, comparing particle temperature with melting/solidus temperature, implementation of melting law, computation of source terms to liquid and/or gas phase, calculation of drag force on particle from liquid and gas phase.

```
DEFINE_DPM_SCALAR_UPDATE(scalar_update, c, t, initialize, tp)
{
   if (initialize) /*at the start of every dpm time step*/
   {
      TP_USER_REAL(tp,4) = 0.0; //deltaT
      float flow_time = CURRENT_TIME * 100.0;
      float particle_time = TP_TIME(tp);
      particle_time = round(particle_time*10000);
      float particle_interval = 1000;
      float interval = 100.0; //interval = 10/10 = 1s
      //print file properties for every flow second and particle_time
      is multiple of 0.1s so as to get only one value
      #if RP_NODE
      if (dmod(flow_time, interval) == 0.00 &&  abs(dmod(particle_time,
      particle_interval)) == 0.0000 && TP_MASS(tp) > 0.0 )
         {
            switch (myid)
            {
               case 0:
               if(NULL == (fp = fopen("node0.txt","a")))
               Error("Could not open file for append!\n");
               break;
               case 1:
               if(NULL == (fp = fopen("node1.txt","a")))
               Error("Could not open file for append!\n");
               break;
               case 2:
               if(NULL == (fp = fopen("node2.txt","a")))
               Error("Could not open file for append!\n");
               break;
               case 3:
               if(NULL == (fp = fopen("node3.txt","a")))
               Error("Could not open file for append!\n");
               break;
               case 4:
               if(NULL == (fp = fopen("node4.txt","a")))
               Error("Could not open file for append!\n");
               break;
               case 5:
               if(NULL == (fp = fopen("node5.txt","a")))
               Error("Could not open file for append!\n");
               break;
               case 6:
               if(NULL == (fp = fopen("node6.txt","a")))
               Error("Could not open file for append!\n");
               break;
```

```
             case 7:
             if(NULL == (fp = fopen("node7.txt","a")))
             Error("Could not open file for append!\n");
             break;
             case 8:
             if(NULL == (fp = fopen("node8.txt","a")))
             Error("Could not open file for append!\n");
             break;
             case 9:
             if(NULL == (fp = fopen("node9.txt","a")))
             Error("Could not open file for append!\n");
             break;
             case 10:
             if(NULL == (fp = fopen("node10.txt","a")))
             Error("Could not open file for append!\n");
             break;
             case 11:
             if(NULL == (fp = fopen("node11.txt","a")))
             Error("Could not open file for append!\n");
             break;
             case 12:
             if(NULL == (fp = fopen("node12.txt","a")))
             Error("Could not open file for append!\n");
             break;
             case 13:
             if(NULL == (fp = fopen("node13.txt","a")))
             Error("Could not open file for append!\n");
             break;
             case 14:
             if(NULL == (fp = fopen("node14.txt","a")))
             Error("Could not open file for append!\n");
             break;
             case 15:
             if(NULL == (fp = fopen("node15.txt","a")))
             Error("Could not open file for append!\n");
             break;
           }
     fprintf(fp, "\n%i %lli %f %f %f %f %f %f %f %f %f", myid,
     TP_ID(tp), TP_MASS(tp),TP_USER_REAL(tp,6)*10/*10 = parcel
     strength*/, TP_RHO(tp), TP_DIAM(tp), TP_TIME(tp), TP_T(tp),
     TP_USER_REAL(tp,1), TP_USER_REAL(tp,3), TP_USER_REAL(tp,5));
     fclose(fp);
        }
     #endif
     TP_USER_REAL(tp,6) = 0.0;
     TP_USER_REAL(tp,7) = 0.0;
   }
   /*if single particle setup, fix particle in initial position, zero
   velocity every timestep, uncomment the next section*/
     /*
     TP_POS(tp)[0] = TP_INIT_POS(tp)[0];
     TP_POS(tp)[1] = TP_INIT_POS(tp)[1];
     TP_POS(tp)[2] = TP_INIT_POS(tp)[2];
     TP_VEL(tp)[0] = 0.;
     TP_VEL(tp)[1] = 0.;
     TP_VEL(tp)[2] = 0.;
     */
}
```

```
/*If the volatile and char fractions are 0, and temperature is higher
than solidus/melt temperature, switch to melting law*/
DEFINE_DPM_SWITCH(dpm_switch, tp, coupled)
{
   real vf, cf;
   vf = DPM_VOLATILE_FRACTION(tp);
   cf = DPM_CHAR_FRACTION(tp);
   #if RP_NODE
   if (MELT_TEMP < SOLIDUS_TEMP) /*Undergo isothermal law and
   heating*/
   {
      if (vf == 0 && cf == 0 && TP_T(tp) >= MELT_TEMP )
      {
         TP_CURRENT_LAW(tp) = 8;
      }
      else if ((vf == 0) && (cf == 0) && (TP_T(tp) < MELT_TEMP))
      {
         TP_CURRENT_LAW(tp) = DPM_LAW_INITIAL_INERT_HEATING;
      }
   }

   else if (MELT_TEMP > LIQUIDUS_TEMP)/*Undergo nonisothermal law and
   heating*/
   {
      if (vf == 0 && cf == 0 && (TP_T(tp) >= SOLIDUS_TEMP))
      {
         TP_CURRENT_LAW(tp) = 8;
      }
      else if (vf == 0 && cf == 0 && (TP_T(tp) < SOLIDUS_TEMP))
      {
         TP_CURRENT_LAW(tp) = DPM_LAW_INITIAL_INERT_HEATING;
      }
   }
   #endif
}


/*particle melting law, only applies to melting particles*/
DEFINE_DPM_LAW(meltinglaw, tp, coupled)
{
   if (MELT_TEMP < SOLIDUS_TEMP) /*Undergo isothermal melting and
   heating*/
      {
         real temp;
         real heat_absorbed;
         real delta_m;
         temp = TP_T(tp);
         InertHeatingLaw(tp); //Inert heating law, measure change in
         temperature from convection
         TP_USER_REAL(tp,4) = TP_T(tp) - temp; /*Delta T*/
         if (TP_USER_REAL(tp,4) > 0) /*Heat gained from surroundings*/
            {
               heat_absorbed = -1 * (TP_MASS(tp) * solid_capacity *
               TP_USER_REAL(tp,4)); /*heat absorbed from fluid [J],
               mp*Cp,s*dT*/
               TP_USER_REAL(tp,6) = heat_absorbed;
               delta_m = heat_absorbed/LATENT_HEAT; //kg, change in mass
               TP_USER_REAL(tp,7) = delta_m; //accumulated change in
               mass over time step [kg]
```

```
             TP_MASS(tp) += delta_m; //mass of solid -= change in mass
             due to melting
             TP_DIAM(tp) = pow(6.0 * TP_MASS(tp) / (TP_RHO(tp) *
             M_PI), 1./3.);
             TP_T(tp) = MELT_TEMP;
             TP_USER_REAL(tp,1) += -1*TP_USER_REAL(tp,6); //cumulated
             latent heat source term [J]
             TP_USER_REAL(tp,2) += -1*TP_USER_REAL(tp,7); //cumulated
             mass loss [kg]
          }
        else if (TP_USER_REAL(tp,4) < 0)
          {
             heat_absorbed = -1 * (TP_MASS(tp) * solid_capacity *
             TP_USER_REAL(tp,4)); //heat given to fluid, positive [J]
             TP_USER_REAL(tp,6) = heat_absorbed;
             delta_m = heat_absorbed/LATENT_HEAT; //kg, change in
             mass, positive
             TP_USER_REAL(tp,7) = delta_m; //accumulated change in
             mass over time step [kg]
             TP_MASS(tp) += delta_m; //mass of solid -= change in mass
             due to melting
             TP_DIAM(tp) = pow(6.0 * TP_MASS(tp) / (TP_RHO(tp) *
             M_PI), 1./3.);
             TP_USER_REAL(tp,1) += -1*TP_USER_REAL(tp,6); //cumulated
             latent heat source term [J]
             TP_USER_REAL(tp,2) += -1*TP_USER_REAL(tp,7); //cumulated
             mass loss [kg]
          }
        }
   else if (MELT_TEMP > LIQUIDUS_TEMP)
   /*Undergo nonisothermal   melting and heating*/
     {
        real temp;
        real heat_absorbed;
        real dp_initial;
        dp_initial = TP_DIAM(tp);

        real solid_c;
        solid_c = 2500;

        //calculate heat gained from convection and radiation
        temp = TP_T(tp);
        InertHeatingLaw(tp); //Inert heating law, measure change in
        temperature from convection or radiation
        TP_USER_REAL(tp,4) = TP_T(tp) - temp;
        /*Calculate convection terms, Q*/
        heat_absorbed = (TP_MASS(tp) * solid_c * TP_USER_REAL(tp,4));
        TP_USER_REAL(tp,5) += heat_absorbed; /*Cumulative heat
        absorbed from convection*/
        TP_USER_REAL(tp,0) += heat_absorbed; /*h = h + Q, each
        particle's enthalpy account*/
        /*Change in diameter, and calculate associated mass change and
        latent heat required for this mass change*/
        TP_DIAM(tp) = TP_INIT_DIAM(tp) - TP_INIT_DIAM(tp) * (TP_T(tp)
        - SOLIDUS_TEMP) / (LIQUIDUS_TEMP - SOLIDUS_TEMP);
        TP_USER_REAL(tp,7) = TP_RHO(tp) * M_PI / 6 * (pow(TP_DIAM(tp),
        3.) - pow(dp_initial, 3.)); /*Change in mass with change in
        temperature, negative*/
```

```
        TP_USER_REAL(tp,6) = TP_USER_REAL(tp,7) * LATENT_HEAT;
        /*latent heat required to melt that mass*/

    if (TP_USER_REAL(tp,4) > 0) /*Heat gained from convection and
    radiation, Q is positive*/
          {
             if (TP_USER_REAL(tp,0) >= (-1 * TP_USER_REAL(tp,6) +
             heat_absorbed)) /*Heat gained is sufficient to melt and
             raise the temperature*/
             {
                TP_USER_REAL(tp,0) -= (-1 * TP_USER_REAL(tp,6) +
                heat_absorbed);
             }
             else if (TP_USER_REAL(tp,0) < (-1 * TP_USER_REAL(tp,6) +
             heat_absorbed)) /*Heat gained is insufficient to melt and
             raise the temperature*/
             {
                TP_T(tp) = temp; /*particle temp and diameter do not
                change*/
                TP_DIAM(tp) = dp_initial;
                TP_USER_REAL(tp,6) = 0; /*no latent heat absorbed*/
                TP_USER_REAL(tp,7) = 0; /*no mass change*/
             }
          }
    else if (TP_USER_REAL(tp,4) < 0) //Heat loss to convection and
    radiation, Q is negative
          {
             TP_T(tp) = temp;
             TP_DIAM(tp) = dp_initial; //particle temp and diameter do
             not change
             TP_USER_REAL(tp,6) = 0; //no latent heat absorbed
             TP_USER_REAL(tp,7) = 0; //no mass change
          }

    TP_MASS(tp) = TP_RHO(tp) * M_PI / 6 * pow(TP_DIAM(tp), 3.);
    TP_USER_REAL(tp,1) += -1*TP_USER_REAL(tp,6); //cumulated latent
    heat source term [J]
    TP_USER_REAL(tp,2) += -1*TP_USER_REAL(tp,7); //cumulated mass loss
    [kg]
     }
}

DEFINE_DPM_SOURCE(particle_source, c, t, S, strength, tp)
{
  /*Isothermal melting and heating, computation and addition of
  source terms to primary phase*/
  if (MELT_TEMP < SOLIDUS_TEMP && TP_CURRENT_LAW(tp) == 8)
     {
        /*interphase enthalpy from change in thermal energy of
        particles, only applies to primary phase, calculated by
        FLUENT*/
        real energy_source =
        strength*(TP_MASS0(tp)*solid_capacity*(TP_T0(tp)-298.15) -
        TP_MASS(tp)*solid_capacity*(TP_T(tp)-298.15));

        cell_t c = TP_CELL(tp);
        Thread *t = TP_CELL_THREAD(tp);
        /*Saving of source terms into cell locations*/
        /*mass source from discharged melt*/
```

```
      mass_removed(c,t) += -1*TP_USER_REAL(tp,7);
      /*momentum source from discharged melt*/
      XMOM_IND(c,t) += -1*TP_USER_REAL(tp,7)*TP_VEL(tp)[0];
      YMOM_IND(c,t) += -1*TP_USER_REAL(tp,7)*TP_VEL(tp)[1];
      ZMOM_IND(c,t) += -1*TP_USER_REAL(tp,7)*TP_VEL(tp)[2];
      /*energy source from discharged melt*/
      ENERGY_IND(c,t) += -1*TP_USER_REAL(tp,7)*liquid_capacity
      *(MELT_TEMP-298.15);
      /*DeltaT is positive, heat absorbed from primary phase,
      melting*/
      if (TP_USER_REAL(tp,4) > 0.0)
      {
         if (TP_USER_REAL(tp,3) >= 0.95) //condition for particle
         removal, mass loss fraction >=95%
         {
            MARK_TP(tp, P_FL_REMOVED);
            mass_removed(c,t) += TP_MASS(tp);
            TP_USER_REAL(tp,3) = 1;
            S->energy -= strength*TP_MASS(tp)*LATENT_HEAT;
         }
         else if (TP_USER_REAL(tp,3) < 0.99) //particle not removed
         {
            S->energy += strength*TP_USER_REAL(tp,7) *LATENT_HEAT;
            //latent heat of melting + change in thermal energy of
            particles (auto added)
            TP_USER_REAL(tp,3) = 1 - TP_MASS(tp)/TP_INIT_MASS(tp);
         }
      }

      /*DeltaT is negative, heat released to primary phase,
      resolidification*/
      else if (TP_USER_REAL(tp,4) <= 0.0)
      {
         S->energy += strength*TP_USER_REAL(tp,7)*LATENT_HEAT;
         //dmp/dt*latent_heat + heat absorbed from convection + heat
         from inert source
         TP_USER_REAL(tp,3) = 1 - TP_MASS(tp)/TP_INIT_MASS(tp);
      }
   }

/*Non-isothermal melting and heating, computation and addition of
source terms to primary phase*/
else if (MELT_TEMP > LIQUIDUS_TEMP && TP_CURRENT_LAW(tp) == 8)
   {
      real solid_c = 2500;
      /*interphase enthalpy from change in thermal energy of
      particles, only applies to primary phase, calculated by
      FLUENT*/
      real energy_source = strength*(TP_MASS0(tp)*solid_c*
      (TP_T0(tp)-298.15) - TP_MASS(tp)*solid_c*(TP_T(tp)-298.15));

      cell_t c = TP_CELL(tp);
      Thread *t = TP_CELL_THREAD(tp);
      /*Saving of source terms into cell locations*/
      /*mass source from discharged melt*/
      mass_removed(c,t) += -1*TP_USER_REAL(tp,7)*strength;
      /*momentum source from discharged melt*/
      XMOM_IND(c,t) += -1*TP_USER_REAL(tp,7)*TP_VEL(tp)[0]
      *strength;
```

```
        YMOM_IND(c,t) += -1*TP_USER_REAL(tp,7)*TP_VEL(tp)[1]
        *strength;
        ZMOM_IND(c,t) += -1*TP_USER_REAL(tp,7)*TP_VEL(tp)[2]
        *strength;
        /*energy source from discharged melt*/
        ENERGY_IND(c,t) += -1*TP_USER_REAL(tp,7)
        *liquid_capacity*(TP_T(tp)-298.15)*strength;
        S->mass += -S->mass;

        /*DeltaM is negative, melting occurs*/
        if (TP_USER_REAL(tp,7) < 0.0)
        {
          if (TP_USER_REAL(tp,3) >= 0.95) //condition for particle
          removal, mass loss fraction >=95%
          {
             MARK_TP(tp, P_FL_REMOVED);
             mass_removed(c,t) += TP_MASS(tp)*strength;
             TP_USER_REAL(tp,3) = 1;
             S->energy -= strength*TP_MASS(tp)*LATENT_HEAT;
          }
          else if (TP_USER_REAL(tp,3) < 0.95) //particle not removed
          {
             S->energy += -S->energy -strength*TP_MASS(tp)
             *solid_c*TP_USER_REAL(tp,4) -energy_source; //heat
             absorbed from convection and radiation + change in
             thermal energy of particles (auto added)
             TP_USER_REAL(tp,3) = 1 - TP_MASS(tp) /TP_INIT_MASS(tp);
          }
        }

        /*DeltaT is negative, heat released to primary phase,
        resolidification*/
        else if (TP_USER_REAL(tp,7) >= 0.0)
        {
          S->energy += -S->energy -strength*TP_MASS(tp)
          *solid_c*TP_USER_REAL(tp,4) - energy_source;
          //dmp/dt*latent_heat + heat absorbed from convection
          TP_USER_REAL(tp,3) = 1 - TP_MASS(tp)/TP_INIT_MASS(tp);
        }
     }
}

DEFINE_DPM_DRAG(dpm_drag, Re, tp)
{
   cell_t c = TP_CELL(tp);
   Thread *t = TP_CELL_THREAD(tp);
   real drag_force, C_d;
   real x[ND_ND];
   C_CENTROID(x,c,t);
   drag_force = (150*SOLID_FRACTION(c,t)*SOLID_FRACTION(c,t)
   /AIR_FRACTION(c,t) + 1.75*Re*SOLID_FRACTION(c,t)
   /AIR_FRACTION(c,t));
   return drag_force;
}

DEFINE_DPM_BODY_FORCE(liqsolidforce,tp,i)
{
   cell_t c = TP_CELL(tp);
   Thread *t = TP_CELL_THREAD(tp);
```

```
   real k_l_p;
   if (i==0) /*force in x-direction*/
   {
        k_l_p = -1*PL_X(c,t); /*PL_X(c,t) is N/m^3*/
   }
   if (i==1) /*force in y-direction*/
   {
        k_l_p = -1*PL_Y(c,t);
   }
   if (i==2) /*force in z-direction*/
   {
        k_l_p = -1*PL_Z(c,t);
   }

   return (k_l_p/TP_RHO(tp)); /*an acceleration is returned*/
}
```

Fluid-specific functions.

Summary: Addition of source terms to liquid phase via UDMs, definition of droplet diameter, calculation of liquid-gas drag coefficient, addition of drag force on liquid droplets due to resistance of the packed bed via momentum source terms, removal of liquid phase through bottom layer, assignment of solid and air volume fractions to UDMs, summation of source terms for checking purposes.

```
/*For addition of source terms to secondary continuous phases*/
//units of all source term is generation rate/volume

/*Mass (kg/m3s), momentum (N/m3) and energy source terms due to
addition of molten liquid from solid phase*/
DEFINE_SOURCE(mass_source, c, t, dS, eqn) /*compute real mass source
term for a single cell and return it to the solver*/
{
   real source;
   source = mass_removed(c,t) / C_VOLUME(c,t);
   dS[eqn] = 0; //force explicit solution of source term
   return source;
}

DEFINE_SOURCE(xmom_source, c, t, dS, eqn) /*compute real x-momentum
source term for a single cell and return it to the solver*/
{
   real source;
   source = XMOM_IND(c,t) / C_VOLUME(c,t);
   dS[eqn] = 0; //force explicit solution of source term
   return source;
}
```

```
DEFINE_SOURCE(ymom_source, c, t, dS, eqn) /*compute real y-momentum
source term for a single cell and return it to the solver*/
{
   real source;
   source = YMOM_IND(c,t)/ C_VOLUME(c,t);
   dS[eqn] = 0; //force explicit solution of source term
   return source;
}

DEFINE_SOURCE(zmom_source, c, t, dS, eqn)
{
   real source;
   source = ZMOM_IND(c,t) / C_VOLUME(c,t);
   dS[eqn] = 0; //force explicit solution of source term
   return source;
}

DEFINE_SOURCE(energy_source, c, t, dS, eqn)
{
   real source;
   source = ENERGY_IND(c,t) / C_VOLUME(c,t);
   dS[eqn] = 0; //force explicit solution of source term
   return source;
}

DEFINE_PROPERTY(droplet_diameter, c, t)
/*compute diameter based on coarse-grain droplet*/
{
   real coarse_diameter, wax_volume;
   if (C_VOF(c,t) > 0)
   {
      wax_volume = C_VOF(c,t) * C_VOLUME(c,t);
      coarse_diameter = MAX(0.001,pow(6.0 * wax_volume / M_PI, 1./3.));
   }
   else coarse_diameter = 0.;

   return coarse_diameter;
}

DEFINE_EXCHANGE_PROPERTY(drag_coefficient, c, t, i, j)
{
   /*i is primary phase, index 0, j is liquid phase, index 1*/
   Thread *thread_liq, *thread_air;
   real k_g_l, liquid_d, slip_x, slip_y, slip_z, abs_v;
   real x[ND_ND];
   thread_liq = THREAD_SUB_THREAD(t,j);
   thread_air = THREAD_SUB_THREAD(t,i);
   C_CENTROID(x,c,t);
   if ((C_VOF(c,thread_liq) > 0.001 && C_VOF(c,thread_air) > 0.001) &&
   x[1] > 0.03)
   {
      liquid_d = C_PHASE_DIAMETER(c,thread_liq);
      slip_x = C_U(c,thread_air) - C_U(c,thread_liq);
      slip_y = C_V(c,thread_air) - C_V(c,thread_liq);
      slip_z = C_W(c,thread_air) - C_W(c,thread_liq);
      abs_v = sqrt(slip_x*slip_x + slip_y*slip_y + slip_z*slip_z);
      k_g_l = (150*C_VOF(c,thread_liq)*C_VOF(c,thread_liq)
      *C_MU_L(c,thread_air)/(C_VOF(c,thread_air)*liquid_d*liquid_d) +
      1.75*C_R(c,thread_air)*C_VOF(c,thread_liq) *abs_v/(liquid_d));
```

```
   }
   else k_g_l = 0.;
   return k_g_l;
}

/*Drag model for liquid phase*/
DEFINE_SOURCE(xmom_sldrag, c, t, dS, eqn) /*compute real x-momentum
sink for solid-liquid interaction force and return it to the solver*/
{
   real source;
   Thread *tm = THREAD_SUPER_THREAD(t);
   Thread *ts = THREAD_SUB_THREAD(tm, 2); /*solid phase thread 2*/
   source = PL_X(c,t);
   dS[eqn] = PL_X(c,t)/(C_U(c,t)-C_U(c,ts));
   return source;
}

DEFINE_SOURCE(ymom_sldrag, c, t, dS, eqn) /*compute real y-momentum
sink for solid-liquid interaction force and return it to the solver*/
{
   real source;
   Thread *tm = THREAD_SUPER_THREAD(t);
   Thread *ts = THREAD_SUB_THREAD(tm, 2);
   source = PL_Y(c,t);
   dS[eqn] = PL_Y(c,t)/(C_V(c,t)-C_V(c,ts));
   return source;
}

DEFINE_SOURCE(zmom_sldrag, c, t, dS, eqn) /*compute real z-momentum
sink for solid-liquid interaction force and return it to the solver*/
{
   real source;
   Thread *tm = THREAD_SUPER_THREAD(t);
   Thread *ts = THREAD_SUB_THREAD(tm, 2);
   source = PL_Z(c,t);
   dS[eqn] = PL_Z(c,t)/(C_W(c,t)-C_W(c,ts));
   return source;
}

/*Removal of liquid at bottom of reactor; mass sink for phase-2,
momentum and enthalpy sink for phase 1 and 2*/
DEFINE_ADJUST(liq_mass_calculation, d) /*save liquid mass to be
removed to cell variable [kg/m3s]*/
{
   int phase_domain_index;
   Thread *t;
   cell_t c;
   Domain *subdomain;
   real x[ND_ND];

   sub_domain_loop(subdomain, d, phase_domain_index) /*loop over all
   subdomains (phases) in mixture*/
   {
      if (DOMAIN_ID(subdomain) == 3) /*loop if liquid phase*/
      {
         thread_loop_c(t,subdomain)
         {
            begin_c_loop(c,t)
            {
```

```
               C_CENTROID(x,c,t);
               if ( x[1] < 0.03 && C_VOF(c,t) > 0.)
               {
                  EXIT_LIQ_MASS(c,t) = -
                  C_R(c,t)*C_VOF(c,t)/CURRENT_TIMESTEP;
               }
               else EXIT_LIQ_MASS(c,t) = 0.;
               Thread *tm = THREAD_SUPER_THREAD(t);
               Thread *ts = THREAD_SUB_THREAD(tm, 2);
               real slip_x, slip_y, slip_z, solid_d;
               if ((C_VOF(c,t) > 0.00001 && x[1] < 0.23) && x[1] > 0.03)
               {
                  slip_x = C_U(c,t) - C_U(c,ts);
                  slip_y = C_V(c,t) - C_V(c,ts);
                  slip_z = C_W(c,t) - C_W(c,ts);
                  ABS_V(c,t) = sqrt(slip_x*slip_x + slip_y*slip_y +
                  slip_z*slip_z);
                  solid_d = SOLID_DIAMETER(c,t);
                  PL_X(c,t) = -1*(150*SOLID_FRACTION(c,t)
                  *SOLID_FRACTION(c,t)*C_MU_L(c,t)/(C_VOF(c,t)*solid_d*s
                  olid_d) + 1.75*C_R(c,t)*SOLID_FRACTION(c,t)
                  *ABS_V(c,t)/(solid_d))*(C_U(c,t)-C_U(c,ts));
                  PL_Y(c,t) = -1*(150*SOLID_FRACTION(c,t)
                  *SOLID_FRACTION(c,t)*C_MU_L(c,t)/(C_VOF(c,t)*solid_d*s
                  olid_d) + 1.75*C_R(c,t)*SOLID_FRACTION(c,t)
                  *ABS_V(c,t)/(solid_d))*(C_V(c,t)-C_V(c,ts));
                  PL_Z(c,t) = -1*(150*SOLID_FRACTION(c,t)
                  *SOLID_FRACTION(c,t)*C_MU_L(c,t)/(C_VOF(c,t)*solid_d*s
                  olid_d) + 1.75*C_R(c,t)*SOLID_FRACTION(c,t)
                  *ABS_V(c,t)/(solid_d))*(C_W(c,t)-C_W(c,ts));
               }
               else
               {
                  ABS_V(c,t) = 0.0;
                  PL_X(c,t) = 0.0;
                  PL_Y(c,t) = 0.0;
                  PL_Z(c,t) = 0.0;
               }
            }
            end_c_loop(c,t)
         }
      }
   }
}

DEFINE_SOURCE(liq_mass_exit, c, t, dS, eqn) /*mass sink at bottom
layer, y = 0.03 m*/
{
   real source;
   if (EXIT_LIQ_MASS(c,t) < 0.)
      {
         source = EXIT_LIQ_MASS(c,t);
         dS[eqn] = -C_R(c,t)/CURRENT_TIMESTEP;
      }
   else
      {
         source = dS[eqn] = 0.;
      }
   return source;
```

```
}

DEFINE_SOURCE(xmom_liqexit, c, t, dS, eqn)
{
   /*x,y, and z momentum UDF applied for liquid phase only*/
   real source;
   if (EXIT_LIQ_MASS(c,t) < 0.)
   {
      source = EXIT_LIQ_MASS(c,t)*C_U(c,t);
      dS[eqn] = EXIT_LIQ_MASS(c,t);
   }
   else source = dS[eqn] = 0.;
   return source;
}

DEFINE_SOURCE(ymom_liqexit, c, t, dS, eqn)
{
   real source;
   if (EXIT_LIQ_MASS(c,t) < 0.)
   {
      source = EXIT_LIQ_MASS(c,t)*C_V(c,t);
      dS[eqn] = EXIT_LIQ_MASS(c,t);
   }
   else source = dS[eqn] = 0.;
   return source;
}

DEFINE_SOURCE(zmom_liqexit, c, t, dS, eqn)
{
   real source;
   if (EXIT_LIQ_MASS(c,t) < 0.)
   {
      source = EXIT_LIQ_MASS(c,t)*C_W(c,t);
      dS[eqn] = EXIT_LIQ_MASS(c,t);
   }
   else source = dS[eqn] = 0.;
   return source;
}

DEFINE_SOURCE(e_liq, c, t, dS, eqn)
{
   real source;
   if (EXIT_LIQ_MASS(c,t) < 0.)
   {
      source = EXIT_LIQ_MASS(c,t) * liquid_capacity * (C_T(c,t) -
      298.15);
      dS[eqn] = 0;
   }
   else source = dS[eqn] = 0.;
   return source;
}

/*Save solid and air phase volume fraction to UDM at end of every
timestep, for post-processing purposes*/
DEFINE_EXECUTE_AT_END(solid_volume_fraction)
{
#if !RP_HOST
   Domain *d = Get_Domain(4);/*Discrete Phase is Domain ID 4*/
   Thread *t;
```

```
   cell_t c;
   thread_loop_c(t,d)
   {
     begin_c_loop(c,t)
     {
        Thread *tm = THREAD_SUPER_THREAD(t);
        Thread *tg = THREAD_SUB_THREAD(tm, 0); /*Liquid thread
        definition*/
        SOLID_FRACTION(c,t) = C_VOF(c,t); /*save solid volume fraction
        to cell UDM*/
        AIR_FRACTION(c,t) = C_VOF(c,tg); /*save air vf to cell value*/
     }
     end_c_loop(c,t)
   }
#endif
}

/*For recording of total source terms for phase-2, executed at end of
each CFD time-step*/
DEFINE_EXECUTE_AT_END(execute_at_end)
 {
   #if RP_NODE
  Domain *d;
  Thread *t;
  cell_t c;
  d = Get_Domain(4);
   /* Integrate mass, momentum, and energy source terms over domain,
   at each CFD timestep, and reset to 0 */
   real mass_s = 0.;
   real xmom_s = 0.;
   real ymom_s = 0.;
   real zmom_s = 0.;
   real energy_s = 0.;
   real mass_outflow = 0.;
   real exit_mass = 0.;
   double exit_masst = 0.;
   double mass_st = 0.;
   double xmom_st = 0.;
   double ymom_st = 0.;
   double zmom_st = 0.;
   double energy_st = 0.;
   double mass_outflows = 0.;
  thread_loop_c(t,d) /*sum source terms across all cells on one node*/
      {
        begin_c_loop(c,t)
             {

             mass_s += mass_removed(c,t);
                xmom_s += XMOM_IND(c,t);
                ymom_s += YMOM_IND(c,t);
                zmom_s += ZMOM_IND(c,t);
                energy_s += ENERGY_IND(c,t);
                mass_outflow += EXIT_LIQ_MASS(c,t) * CURRENT_TIMESTEP
                * C_VOLUME(c,t);
                CUMULATED_EXIT_LIQ_MASS(c,t) +=
                EXIT_LIQ_MASS(c,t)*CURRENT_TIMESTEP*C_VOLUME(c,t);
                exit_mass += CUMULATED_EXIT_LIQ_MASS(c,t);
                SOLID_DIAMETER(c,t) = C_PHASE_DIAMETER(c,t);
                mass_removed(c,t) = 0.;
```

```
                XMOM_IND(c,t) = 0.;
                YMOM_IND(c,t) = 0.;
                ZMOM_IND(c,t) = 0.;
                ENERGY_IND(c,t) = 0.;
             }
         end_c_loop(c,t)
     }

    /*summing over all compute nodes*/
    mass_st = PRF_GRSUM1(mass_s);
    xmom_st = PRF_GRSUM1(xmom_s);
    ymom_st = PRF_GRSUM1(ymom_s);
    zmom_st = PRF_GRSUM1(zmom_s);
    energy_st = PRF_GRSUM1(energy_s);
    mass_outflows = PRF_GRSUM1(mass_outflow);
    exit_masst =PRF_GRSUM1(exit_mass);
     float flow_time = CURRENT_TIME * 10.0;
     float interval = 10.0; //interval = 10/10 = 1s
     //print file properties for every flow second
   if ( dmod(flow_time, interval) == 0.0 )
   {
     if (myid == 0)
          {
             if(NULL == (fp = fopen("sourceterms.txt","a")))
             Error("Could not open file for append!\n");
             fprintf(fp, "\n%i %.9f %.9f %.9f %.9f %.9f %.3f %f %f",
             myid, mass_st, xmom_st, ymom_st, zmom_st, energy_st,
             mass_outflows, exit_masst, CURRENT_TIME);
             fclose(fp);
          }
   }
#endif
 }
```

A.3. .c file (Non-inert melting model)

A large proportion of the code for the non-inert, non-isothermal melting model specified in Chapter 6 is similar to the code for the inert non-isothermal melting model. Hence, only the functions that were specifically written for the non-inert melting model were included in this section.

Summary: on-demand flagging of particles above solidus temperature, definition of composition-dependent density or assignment of fixed density, definition of composition-dependent heat capacity or assignment of fixed heat capacity, switching of particle laws, implementation of the combustion-melting model, calculation of the source terms to liquid and gas phase.

```
DEFINE_ON_DEMAND(flag_particles) /*Flag particles that are above
solidus temperature*/
{
   Injection *I;
   Particle *p;
  Injection *Ilist = Get_dpm_injections();

     loop(I, Ilist) /*Loop over all particle injections*/
     {
        loop(p,I->p)
        {
          if (TP_T(p) > SOLIDUS_TEMP)
          {
             TP_USER_REAL(p,12) = 1;
          }
          else TP_USER_REAL(p,12) = 0;
          TP_USER_REAL(p,8) = 0;
        }
     }
   if (myid == 0) Message("Particles have been allocated.");
}

DEFINE_DPM_PROPERTY(MSW_density, c, t, tp, T)
{
   real density_a, density_ch, density_v, density_w;

   density_w=1000.;    /* moisture */
   density_v=400.;     /* volatile matter */
   density_ch=430.;     /* fixed carbon/char */
   density_a=2200.;    /* ash */

   real w, v, ch, a;
   real density;
```

```
   if (TP_T(tp) < SOLIDUS_TEMP || (TP_USER_REAL(tp,12) == 1 &&
   TP_T(tp) < LIQUIDUS_TEMP))
   {
     if (NULLP(tp->pp) ||
     NULLP(TP_CELL_THREAD(tp)))
     {
        density=456.75;         /* initial density */
     }
     else
     {
        w = TP_LMF(tp);
        v = TP_VF(tp)/(1-w);
        ch = TP_CF(tp)/(1-w);
        a = 1-v-ch;
        density = 1 / (v/density_v + ch/density_ch + a/density_a);
     }
   }
   else if (TP_T(tp)>=SOLIDUS_TEMP && TP_USER_REAL(tp,12) == 0)
   {
     if (TP_USER_REAL(tp,11) == 0)
     {
        density = TP_RHO(tp);
     }
     else density = TP_USER_REAL(tp,11);
   }
   density = MIN(density, 2200);
   return density;
}

DEFINE_DPM_PROPERTY(MSW_Cp, c, t, tp, T)
{
   real   Cp_a, Cp_v, Cp_ch;
   Cp_v = 4.5099*TP_T(tp) - 101.4917; /* volatile matter
   (biomass+plastics) */
   Cp_ch = 2.09*TP_T(tp) - 0.000685*TP_T(tp)*TP_T(tp) + 420; /* char*/

   if (TP_T(tp) < SOLIDUS_TEMP || TP_USER_REAL(tp,12) != 0)
     {
        if ((TP_T(tp)>1421&&TP_T(tp)<1554) && TP_USER_REAL(tp,12) !=
        0) /*Heat capacity of ash increased to consider latent heat of
        melting*/
        Cp_a = 0.644*TP_T(tp) - 0.000195*TP_T(tp)*TP_T(tp) + 644 +
        3440;

        else
        {
           Cp_a = 0.644*TP_T(tp) - 0.000195*TP_T(tp)*TP_T(tp) + 644;
           /* ash, (same with typical slag composition)*/
        }
     }
   else if (TP_T(tp) >= SOLIDUS_TEMP && TP_USER_REAL(tp,12) == 0)
   /*latent heat of melting considered under melting law*/
     {
        Cp_a = 0.644*TP_T(tp) - 0.000195*TP_T(tp)*TP_T(tp) + 644;
     }

     real w, v, ch, a;
     real Cp;
```

```
   if (NULLP(tp->pp) || NULLP(TP_CELL_THREAD(tp)))
   {
      Cp = 1368.88;         /* initial heat capacity */
   }
   else if (TP_T(tp) >= SOLIDUS_TEMP && TP_USER_REAL(tp,12) == 0)
   {
      if (TP_USER_REAL(tp,9) == 0)
      {
         w = TP_LMF(tp);
         v = TP_VF(tp)/(1-w);
         ch = TP_CF(tp)/(1-w);
         a = 1-v-ch;
         Cp = Cp_a*a + Cp_v*v + Cp_ch*ch;
      }
      else Cp = TP_USER_REAL(tp,9);
   }

   else
   {
      w = TP_LMF(tp);
      v = TP_VF(tp)/(1-w);
      ch = TP_CF(tp)/(1-w);
      a = 1-v-ch;
      Cp = Cp_a*a + Cp_v*v + Cp_ch*ch;
   }

   return Cp;
}

/*Assignment of particle laws and switch to melting law*/
DEFINE_DPM_SWITCH(dpm_switch, tp, ci)
{
   if (TP_LMF(tp) > 0)
   {
      TP_CURRENT_LAW(tp) = DPM_LAW_VAPORIZATION;
   }
   else if (TP_LMF(tp) == 0 && TP_VF(tp) > 0)
   {
      TP_CURRENT_LAW(tp) = DPM_LAW_DEVOLATILIZATION;
   }

   else if (TP_LMF(tp) == 0 && TP_VF(tp) == 0)
      {
            if (TP_T(tp) < SOLIDUS_TEMP || (TP_USER_REAL(tp,12) == 1 &&
            TP_T(tp) < LIQUIDUS_TEMP))
               {
                  if (TP_CF(tp) > 0)
                  {
                     TP_CURRENT_LAW(tp) = DPM_LAW_SURFACE_COMBUSTION;
                  }
                  else if (TP_CF(tp) == 0)
                     TP_CURRENT_LAW(tp) = DPM_LAW_INITIAL_INERT_HEATING;
               }
            else if (TP_T(tp) >= SOLIDUS_TEMP &&
         TP_USER_REAL(tp,12) == 0)
               {
                  if (TP_USER_REAL(tp,8) == 0.0)
                  {
                     TP_USER_REAL(tp,8) = TP_DIAM(tp);
```

```
                  TP_USER_REAL(tp,10) = TP_MASS(tp);
                  TP_USER_REAL(tp,11) = TP_RHO(tp);
                  TP_USER_REAL(tp,9) =
                  DPM_SPECIFIC_HEAT(tp,TP_T(tp));
                }
                TP_CURRENT_LAW(tp) = 8;
             }
     }
}

/*combustion with melting*/
DEFINE_DPM_LAW(meltinglaw, tp, coupled)
{
   if (TP_CURRENT_LAW(tp) == 8 && TP_USER_REAL(tp,12) == 0)
   {
        real temp;
        real heat_absorbed;
        real dp_initial, mass_after_combustion;
        real char_mass;
        real ash_mass;
        //calculate heat gained from convection and combustion

        if (TP_CF(tp) > 0.0)
        {
           temp = TP_T(tp);
           SurfaceCombustionLaw(tp);
           TP_CF(tp) = 1 - TP_USER_REAL(tp,13)/TP_MASS(tp);
           dp_initial = TP_DIAM(tp);
           mass_after_combustion = TP_MASS(tp);
           TP_USER_REAL(tp,4) = TP_T(tp) - temp;
           heat_absorbed = (TP_MASS(tp) *
           DPM_SPECIFIC_HEAT(tp,TP_T(tp)) * TP_USER_REAL(tp,4));
           /*Calculate heat absorbed from gas phase, Q*/
           TP_USER_REAL(tp,5) += heat_absorbed; /*Cumulative heat
           absorbed from convection and combustion*/
           TP_USER_REAL(tp,0) += heat_absorbed; /*h = h + Q, each
           particle's enthalpy account*/
           char_mass = TP_CF(tp)*TP_MASS(tp);
           /*Change in diameter, and calculate associated mass change
           and latent heat required for this mass change*/
           ash_mass = TP_MASS(tp) - char_mass;
           TP_DIAM(tp) = TP_USER_REAL(tp,8) - TP_USER_REAL(tp,8) *
           (TP_T(tp) - SOLIDUS_TEMP) / (LIQUIDUS_TEMP - SOLIDUS_TEMP);
           TP_USER_REAL(tp,7) = TP_RHO(tp) * M_PI / 6 *
           pow(TP_DIAM(tp), 3.) - mass_after_combustion; /*Change in
           mass with change in temperature, negative*/
           TP_USER_REAL(tp,6) = TP_USER_REAL(tp,7) * LATENT_HEAT;
           /*latent heat required to melt that mass*/
        }
        //calculate heat gained from convection only, char fraction =
        0, no density or heat capacity change
        else if (TP_CF(tp) == 0.0)
        {
           temp = TP_T(tp);
           dp_initial = TP_DIAM(tp);
           InertHeatingLaw(tp);
           TP_USER_REAL(tp,4) = TP_T(tp) - temp;
```

```
          heat_absorbed = (TP_MASS(tp) *
          DPM_SPECIFIC_HEAT(tp,TP_T(tp)) * TP_USER_REAL(tp,4));
          /*Calculate heat absorbed from gas phase, Q*/
          TP_USER_REAL(tp,5) += heat_absorbed; /*Cumulative heat
          absorbed from convection and combustion*/
          TP_USER_REAL(tp,0) += heat_absorbed; /*h = h + Q, each
          particle's enthalpy account*/
          char_mass = TP_CF(tp)*TP_MASS(tp);
          /*Change in diameter, and calculate associated mass change
          and latent heat required for this mass change*/
          TP_DIAM(tp) = TP_USER_REAL(tp,8) - TP_USER_REAL(tp,8) *
          (TP_T(tp) - SOLIDUS_TEMP) / (LIQUIDUS_TEMP - SOLIDUS_TEMP);
          TP_USER_REAL(tp,7) = TP_RHO(tp) * M_PI / 6 *
          (pow(TP_DIAM(tp), 3.) - pow(dp_initial, 3.)); /*Change in
          mass with change in temperature, negative*/
          TP_USER_REAL(tp,6) = TP_USER_REAL(tp,7) * LATENT_HEAT;
          /*latent heat required to melt that mass*/
       }

       if (TP_USER_REAL(tp,4) > 0)
       {/*Heat gained from convection and radiation, Q is positive*/
            if (TP_USER_REAL(tp,0) >= (-1 * TP_USER_REAL(tp,6) +
            heat_absorbed)) /*Heat gained is sufficient to melt and
            raise the temperature*/
            {
               TP_USER_REAL(tp,0) -= (-1 * TP_USER_REAL(tp,6) +
               heat_absorbed);
               TP_USER_REAL(tp,13) += TP_USER_REAL(tp,7);
            }
            else if (TP_USER_REAL(tp,0) < (-1 * TP_USER_REAL(tp,6) +
            heat_absorbed)) /*Heat gained is insufficient to melt and
            raise the temperature*/
            {
               TP_T(tp) = temp; /*particle temp and diameter do not
               change*/
               TP_DIAM(tp) = dp_initial;
               TP_USER_REAL(tp,6) = 0; /*no latent heat absorbed*/
               TP_USER_REAL(tp,7) = 0; /*no mass change*/
               TP_USER_REAL(tp,13) += TP_USER_REAL(tp,7);
            }
       }
       else //Heat loss to convection and radiation, Q is negative
          {
            TP_T(tp) = temp;
            TP_DIAM(tp) = dp_initial; //particle temp and diameter do
            not change
            TP_USER_REAL(tp,6) = 0;
            TP_USER_REAL(tp,13) += TP_USER_REAL(tp,7);
            TP_USER_REAL(tp,7) = 0;
          }
          TP_MASS(tp) = TP_RHO(tp) * M_PI / 6 * pow(TP_DIAM(tp), 3.);
          TP_CF(tp) = char_mass / (char_mass + TP_USER_REAL(tp,13));
          TP_USER_REAL(tp,1) += -1*TP_USER_REAL(tp,6); //cumulated
          latent heat absorbed [J]
          TP_USER_REAL(tp,2) += -1*TP_USER_REAL(tp,7); //cumulated
          mass loss due to melting [kg]
  }
}
```

```
/*Only applies to particles under melting law*/
DEFINE_DPM_SOURCE(particle_source, c, t, S, strength, tp)
{
 if (TP_CURRENT_LAW(tp) == 8 && TP_USER_REAL(tp,12) != 0)
     {
        if (TP_T(tp) >= LIQUIDUS_TEMP)
        {
             fp = fopen("removedmswtoslag.txt","a");
             fprintf(fp, "\n %s %" int64_fmt
             " %e %f %f %f %f %f %f %.0f %i",
             TP_INJECTION(tp)->name,TP_ID(tp), TP_TIME(tp),
             TP_T(tp),TP_MASS(tp), TP_N(tp),TP_DIAM(tp),
             TP_CF(tp), TP_USER_REAL(tp,9),
          TP_USER_REAL(tp,12),TP_CURRENT_LAW(tp));
             fclose(fp);
             MARK_TP(tp, P_FL_REMOVED);
             S->energy -= TP_MASS(tp)*LATENT_HEAT*strength;
        }
     }
   /*Non-isothermal melting*/
   if (TP_CURRENT_LAW(tp) == 8 && TP_USER_REAL(tp,12) == 0)
     {
        real solid_c = TP_USER_REAL(tp,9);
        /*interphase enthalpy from change in thermal energy of
        particles, only applies to primary phase, calculated by
        FLUENT*/
        real energy_source = strength*(TP_MASS0(tp)*solid_c
        *(TP_T0(tp)-298.15) - TP_MASS(tp)*solid_c*(TP_T(tp)-298.15));

        cell_t c = TP_CELL(tp);
        Thread *t = TP_CELL_THREAD(tp);

        /*Saving of source terms into cell locations*/
        /*mass source from discharged melt*/
        mass_removed(c,t) += -1*TP_USER_REAL(tp,7)*strength;
        /*momentum source from discharged melt*/
        XMOM_IND(c,t) += -1*TP_USER_REAL(tp,7)*TP_VEL(tp)[0]
        *strength;
        YMOM_IND(c,t) += -1*TP_USER_REAL(tp,7)*TP_VEL(tp)[1]
        *strength;
        ZMOM_IND(c,t) += -1*TP_USER_REAL(tp,7)*TP_VEL(tp)[2]
        *strength;
        /*energy source from discharged melt*/
        ENERGY_IND(c,t) += -1*TP_USER_REAL(tp,7)*strength
        *liquid_capacity*(TP_T(tp)-298.15);

        S->mass += -S->mass;
        S->energy += -S->energy -strength*TP_MASS(tp)*solid_c
        *TP_USER_REAL(tp,4) - energy_source;
        TP_USER_REAL(tp,3) = TP_USER_REAL(tp,2) /TP_USER_REAL(tp,10);
        if (TP_USER_REAL(tp,3)>=0.95 && TP_USER_REAL(tp,3) < 1)
   {
             fp = fopen("melted.txt","a");
             fprintf(fp, "\n %s %" int64_fmt
             " %e %f %f %f %f %f %f %.4f %i",
             TP_INJECTION(tp)->name,TP_ID(tp), TP_TIME(tp), TP_T(tp),
             TP_MASS(tp), TP_N(tp),  TP_DIAM(tp),
             TP_CF(tp),TP_USER_REAL(tp,5), TP_USER_REAL(tp,3),
             TP_CURRENT_LAW(tp));
```

```
             fclose(fp);

             mass_removed(c,t) += TP_MASS(tp)*strength;
             XMOM_IND(c,t) += TP_MASS(tp)*TP_VEL(tp)[0]*strength;
             YMOM_IND(c,t) += TP_MASS(tp)*TP_VEL(tp)[1]*strength;
             ZMOM_IND(c,t) += TP_MASS(tp)*TP_VEL(tp)[2]*strength;
             ENERGY_IND(c,t) += TP_MASS(tp)*LATENT_HEAT*strength;
             TP_USER_REAL(tp,3) = 1;
             MARK_TP(tp, P_FL_REMOVED);
             S->energy -= TP_MASS(tp)*LATENT_HEAT*strength;
        }
     }
}
```

Appendix B. Process flow of combustion-melting model

Table B.1. Process flow of combustion-melting model.

	Char fraction > 0	***Char fraction = 0***
Step 1	Obtain the new particle temperature T_{p}, assuming combustion takes place.	Obtain the new particle temperature T_{p}, assuming inert heating takes place.
Step 2	Calculate the heat absorbed from fluid and combustion and add to particle enthalpy, h_{p}. $Q = m_{\mathrm{p}} c_{\mathrm{p}} \frac{dT_p}{dt} = h_c A_{\mathrm{p}}(T_{\mathrm{f}} - T_{\mathrm{p}}) - f_h \frac{dm_p}{dt} H_{reac}$	Calculate the heat absorbed from fluid and add to particle enthalpy, h_{p}. $Q = m_{\mathrm{p}} c_{\mathrm{p}} \frac{dT_p}{dt} = h_c A_{\mathrm{p}}(T_{\mathrm{f}} - T_{\mathrm{p}})$
Step 3	"State 1": Record particle mass and diameter after combustion, and particle temperature before combustion.	"State 1": Record particle temperature and diameter before inert heating.

*Step 4 to Step 9 are the same regardless of char fraction***

Step 4 Assuming that particle rises to temperature T_{p}, calculate theoretical particle diameter and mass based on the new temperature. $d_{\mathrm{p,0}}$ is the particle diameter just before melting occurs and is saved for every particle as the diameter when the particle first reaches the solidus temperature.

$$d_{\mathrm{p}} = d_{\mathrm{p,0}} - d_{\mathrm{p,0}} \frac{T_{\mathrm{p}} - T_{\mathrm{s}}}{T_{\mathrm{l}} - T_{\mathrm{s}}}$$

Particle density is assumed to be constant throughout the melting process by setting it to the particle density when the particle first reaches solidus temperature.

The theoretical mass is then calculated as $m_{\mathrm{p}} = \frac{\rho_{\mathrm{p,0}}\pi}{6}(d_{\mathrm{p}}^3)$

Table B.1. (continued)

Step 5	Compare particle enthalpy with the calculated heat required for the change in mass (sum of sensible and latent heat). $\frac{dm_\mathrm{p}}{dt}$ for char fraction > 0 is the change in mass from the particle mass after combustion. Compare h_p with $m_\mathrm{p} c_\mathrm{p} \frac{dT_\mathrm{p}}{dt} + (-\frac{dm_\mathrm{p}}{dt} h_m)$
Step 6	If particle enthalpy is sufficient, melting occurs, and particle changes in mass, temperature, and diameter take place according to Step 4. Heat required is subtracted from particle enthalpy.
Step 7	If particle enthalpy is insufficient, no melting occurs, and particle values return to those saved in Step 3 (“State 1”). This means that for char fraction > 0, particle mass is still lost to combustion.
Step 8	Calculate the mass loss fraction, $\beta = 1 - \frac{m_\mathrm{p}}{m_\mathrm{p,0}}$, where $m_\mathrm{p,0}$ is the particle mass recorded at the start of the melting process.
Step 9	Convert to volumetric and add the relevant source terms to the gas (energy: Q_pg) and molten liquid phase (mass: S_mass; momentum: $S_\mathrm{mass}\vec{v}_\mathrm{f}$; energy: $S_\mathrm{mass}(h_\mathrm{melt} - h_\mathrm{ref})$).

References

[1] S. Kaza, L. Yao, P. Bhada-Tata, and F. Van Woerden, *What a waste 2.0: a global snapshot of solid waste management to 2050*. World Bank Publications, 2018.

[2] National Environment Agency, "Waste Management: Overview," November 1 2019. [Online]. Available: https://www.nea.gov.sg/our-services/waste-management/overview

[3] Ministry of the Environment and Water Resources and National Environment Agency, *Zero Waste Masterplan Singapore*. 2019.

[4] A. Ramos, E. Monteiro, and A. Rouboa, "Numerical approaches and comprehensive models for gasification process: A review," *Renewable and Sustainable Energy Reviews*, vol. 110, pp. 188-206, 2019, doi: 10.1016/j.rser.2019.04.048.

[5] C. Magnani and S. Ali, "Mathematical modeling of the stream method of underground coal gasification," *Society of Petroleum Engineers Journal*, vol. 15, no. 05, pp. 425-436, 1975.

[6] C. Thorsness and R. Rosza, "Lawrence Livermore Laboratory in-situ coal gasification program: model calculations and laboratory experiments," 1976.

[7] A. Winslow, "Numerical model of coal gasification in a packed bed," in *Symposium (international) on combustion*, 1977, vol. 16, no. 1: Elsevier, pp. 503-513.

[8] S. K. Sansaniwal, K. Pal, M. A. Rosen, and S. K. Tyagi, "Recent advances in the development of biomass gasification technology: A comprehensive review," *Renewable and Sustainable Energy Reviews*, vol. 72, pp. 363-384, 2017, doi: 10.1016/j.rser.2017.01.038.

[9] U. Arena, "Process and technological aspects of municipal solid waste gasification. A review," *Waste Management*, vol. 32, no. 4, pp. 625-639, 2012, doi: 10.1016/j.wasman.2011.09.025.

[10] H. A. Long and T. Wang, "Parametric techno-economic studies of coal/biomass co-gasification for IGCC plants with carbon capture using various coal ranks, fuel-feeding schemes, and syngas cooling methods," *International Journal of Energy Research*, vol. 40, no. 4, pp. 473-496, 2016, doi: 10.1002/er.3452.

[11] V. S. Sikarwar *et al.*, "An overview of advances in biomass gasification," *Energy & Environmental Science*, vol. 9, no. 10, pp. 2939-2977, 2016, doi: 10.1039/c6ee00935b.

[12] K. Choy, J. Porter, C. Hui, and G. McKay, "Process design and feasibility study for small scale MSW gasification," *Chemical Engineering Journal*, vol. 105, no. 1-2, pp. 31-41, 2004, doi: 10.1016/j.cej.2004.07.012.

[13] N. Tanigaki, Y. Ishida, and M. Osada, "A case-study of landfill minimization and material recovery via waste co-gasification in a new waste management scheme," *Waste Management*, vol. 37, pp. 137-146, 2015, doi: 10.1016/j.wasman.2014.07.024.

[14] T. Goh. "Processed waste known as NEWSand may be used as construction materials here." The Straits Times. https://www.straitstimes.com/singapore/processed-waste-known-as-

newsand-may-be-used-as-construction-materials-here (accessed Nov 11, 2019).

[15] R. Siddique, "Utilization of municipal solid waste (MSW) ash in cement and mortar," *Resources, Conservation and Recycling*, vol. 54, no. 12, pp. 1037-1047, 2010, doi: 10.1016/j.resconrec.2010.05.002.

[16] B. Tang, J. Lin, S. Qian, J. Wang, and S. Zhang, "Preparation of glass–ceramic foams from the municipal solid waste slag produced by plasma gasification process," *Materials Letters*, vol. 128, pp. 68-70, 2014, doi: 10.1016/j.matlet.2014.04.097.

[17] R. Dippenaar, "Industrial uses of slag (the use and re-use of iron and steelmaking slags)," *Ironmaking & Steelmaking*, vol. 32, no. 1, pp. 35-46, 2013, doi: 10.1179/174328105x15805.

[18] K. Laohalidanond, P. Chaiyawong, and S. Kerdsuwan, "Status of Using Biomass Gasification for Heat and Power in Thailand," *Energy Procedia*, vol. 79, pp. 385-390, 2015, doi: 10.1016/j.egypro.2015.11.507.

[19] T. M. Ismail, A. Ramos, E. Monteiro, M. A. El-Salam, and A. Rouboa, "Parametric studies in the gasification agent and fluidization velocity during oxygen-enriched gasification of biomass in a pilot-scale fluidized bed: Experimental and numerical assessment," *Renewable Energy*, vol. 147, pp. 2429-2439, 2020, doi: 10.1016/j.renene.2019.10.029.

[20] D. T. Pio, L. A. C. Tarelho, A. M. A. Tavares, M. A. A. Matos, and V. Silva, "Co-gasification of refused derived fuel and biomass in a pilot-scale bubbling fluidized bed reactor," *Energy Conversion and Management*, vol. 206, p. 112476, 2020, doi: 10.1016/j.enconman.2020.112476.

[21] E. Simsek, B. Brosch, S. Wirtz, V. Scherer, and F. Krüll, "Numerical simulation of grate firing systems using a coupled CFD/discrete element method (DEM)," *Powder Technology*, vol. 193, no. 3, pp. 266-273, 2009, doi: 10.1016/j.powtec.2009.03.011.

[22] W. Li and W. Zhong, "CFD simulation of hydrodynamics of gas–liquid–solid three-phase bubble column," *Powder Technology*, vol. 286, pp. 766-788, 2015, doi: 10.1016/j.powtec.2015.09.028.

[23] E. Guerrero, F. Muñoz, and N. Ratkovich, "Comparison between Eulerian and VOF models for two-phase flow assessment in vertical pipes," *CT&F-Ciencia, Tecnología y Futuro*, vol. 7, no. 1, pp. 73-84, 2017.

[24] X. F. Dong *et al.*, "Investigation of Molten Liquids Flow in the Blast Furnace Lower Zone: Numerical Modelling of Molten Slag Through Channels in a Packed Bed," *Metallurgical and Materials Transactions B*, vol. 52, no. 1, pp. 255-266, 2020, doi: 10.1007/s11663-020-02009-1.

[25] H. Takeda, N. Esaki, K. Doi, H. Murakami, K. Yamasaki, and Y. Kawase, "Flow Simulation in Bubble Columns in Regard to Bubble Coalescence and Break-up Utilizing LES and DEM," *Journal of Chemical Engineering of Japan*, vol. 37, no. 8, pp. 976-989, 2004, doi: 10.1252/jcej.37.976.

[26] B. Chaudhuri, F. J. Muzzio, and M. S. Tomassone, "Modeling of heat transfer in granular flow in rotating vessels," *Chemical Engineering Science*, vol. 61, no. 19, pp. 6348-6360, 2006, doi: 10.1016/j.ces.2006.05.034.

[27] A. M. C. Branco Jr, A. L. A. Mesquita, and J. R. P. Vaz, "Application of the linear spring-dashpot model in the CFD-DEM simulation of alumina fluidization," *Revista de Engenharia Térmica*, vol. 14, no. 2, pp. 95-101, 2015.

[28] P. A. Cundall and O. D. Strack, "A discrete numerical model for granular assemblies," *Geotechnique,* vol. 29, no. 1, pp. 47-65, 1979.

[29] T. Srivastava, "Renewable energy (Gasification)," *Advance in Electronic and Electric Engineering,* vol. 3, no. 9, pp. 1243-1250, 2013.

[30] J. Phillips, "Different types of gasifiers and their integration with gas turbines," *The gas turbine handbook,* vol. 1, 2006.

[31] R. Warnecke, "Gasification of biomass: comparison of fixed bed and fluidized bed gasifier," *Biomass and Bioenergy,* vol. 18, no. 6, pp. 489-497, 2000, doi: 10.1016/S0961-9534(00)00009-X.

[32] R. I. Singh, A. Brink, and M. Hupa, "CFD modeling to study fluidized bed combustion and gasification," *Applied Thermal Engineering,* vol. 52, no. 2, pp. 585-614, 2013, doi: 10.1016/j.applthermaleng.2012.12.017.

[33] T. Zhou, S. Yang, Y. Wei, J. Hu, and H. Wang, "Impact of wide particle size distribution on the gasification performance of biomass in a bubbling fluidized bed gasifier," *Renewable Energy,* vol. 148, pp. 534-547, 2020, doi: 10.1016/j.renene.2019.10.059.

[34] Y. Wu, P. J. Smith, J. Zhang, J. N. Thornock, and G. Yue, "Effects of turbulent mixing and controlling mechanisms in an entrained flow coal gasifier," *Energy & Fuels,* vol. 24, no. 2, pp. 1170-1175, 2009.

[35] Z. Hu, Y. Peng, F. Sun, S. Chen, and Y. Zhou, "Thermodynamic equilibrium simulation on the synthesis gas composition in the context of underground coal gasification," *Fuel,* vol. 293, p. 120462, 2021, doi: 10.1016/j.fuel.2021.120462.

[36] M. Awais *et al.*, "Co-gasification of different biomass feedstock in a pilot-scale (24 kWe) downdraft gasifier: An experimental approach," *Energy,* vol. 238, p. 121821, 2022, doi: 10.1016/j.energy.2021.121821.

[37] A. Silaen and T. Wang, "Effects of turbulence and devolatilization models on gasification simulation," in *25th International Pittsburgh Coal Conference*, Pittsburgh, USA, 2008.

[38] S. Hosseini and R. Gupta, "Inorganic Matter Behavior during Coal Gasification: Effect of Operating Conditions and Particle Trajectory on Ash Deposition and Slag Formation," *Energy & Fuels,* vol. 29, no. 3, pp. 1503-1519, 2015, doi: 10.1021/ef502640p.

[39] V. Krishnamoorthy and S. Pisupati, "A Critical Review of Mineral Matter Related Issues during Gasification of Coal in Fixed, Fluidized, and Entrained Flow Gasifiers," *Energies,* vol. 8, no. 9, pp. 10430-10463, 2015, doi: 10.3390/en80910430.

[40] M. Zhai, X. Li, D. Yang, Z. Ma, and P. Dong, "Ash fusion characteristics of biomass pellets during combustion," *Journal of Cleaner Production,* vol. 336, p. 130361, 2022, doi: 10.1016/j.jclepro.2022.130361.

[41] Q. Huang, P. Paul, D. Bhattacharyya, R. C. Pillai, K. Sabolsky, and E. M. Sabolsky, "Estimations of Gasifier Wall Temperature and Extent of Slag Penetration Using a Refractory Brick with Embedded Sensors," *Industrial & Engineering Chemistry Research,* vol. 56, no. 35, pp. 9858-9867, 2017, doi: 10.1021/acs.iecr.7b02604.

[42] J. P. Bennett and K.-S. Kwong, "Failure Mechanisms in High Chrome Oxide Gasifier Refractories," *Metallurgical and Materials Transactions A,* vol. 42, no. 4, pp. 888-904, 2011, doi: 10.1007/s11661-011-0635-x.

[43] P. Wang and M. Massoudi, "Slag Behavior in Gasifiers. Part I: Influence of Coal Properties and Gasification Conditions," *Energies*, vol. 6, no. 2, pp. 784-806, 2013, doi: 10.3390/en6020784.

[44] M. Massoudi and P. Wang, "Slag Behavior in Gasifiers. Part II: Constitutive Modeling of Slag," *Energies*, vol. 6, no. 2, pp. 807-838, 2013, doi: 10.3390/en6020807.

[45] Y. Z. Zheng, Q. Li, Z. H. Zheng, J. F. Zhu, and P. L. Cao, "Modeling the impact, flattening and solidification of a molten droplet on a solid substrate during plasma spraying," *Applied Surface Science*, vol. 317, pp. 526-533, 2014, doi: 10.1016/j.apsusc.2014.08.032.

[46] T. Tsory, N. Ben-Jacob, T. Brosh, and A. Levy, "Thermal DEM–CFD modeling and simulation of heat transfer through packed bed," *Powder Technology*, vol. 244, pp. 52-60, 2013, doi: 10.1016/j.powtec.2013.04.013.

[47] D. Hummel, S. Beer, and A. Hornung, "A conjugate heat transfer model for unconstrained melting of macroencapsulated phase change materials subjected to external convection," *International Journal of Heat and Mass Transfer,* vol. 149, p. 119205, 2020, doi: 10.1016/j.ijheatmasstransfer.2019.119205.

[48] H. Li, N. Yoshihiko, Z. Dong, and M. Zhang, "Application of the FactSage to Predict the Ash Melting Behavior in Reducing Conditions," *Chinese Journal of Chemical Engineering,* vol. 14, no. 6, pp. 784-789, 2006, doi: 10.1016/s1004-9541(07)60012-3.

[49] H. Wang, B. Ding, X.-Y. Liu, X. Zhu, X.-Y. He, and Q. Liao, "Solidification behaviors of a molten blast furnace slag droplet cooled by air," *Applied Thermal Engineering,* vol. 127, pp. 915-924, 2017, doi: 10.1016/j.applthermaleng.2017.07.215.

[50] Y. Dutil, D. R. Rousse, N. B. Salah, S. Lassue, and L. Zalewski, "A review on phase-change materials: Mathematical modeling and simulations," *Renewable and Sustainable Energy Reviews,* vol. 15, no. 1, pp. 112-130, 2011, doi: 10.1016/j.rser.2010.06.011.

[51] Z. Liang and X. Ma, "Mathematical modeling of MSW combustion and SNCR in a full-scale municipal incinerator and effects of grate speed and oxygen-enriched atmospheres on operating conditions," *Waste Management,* vol. 30, no. 12, pp. 2520-9, Dec 2010, doi: 10.1016/j.wasman.2010.05.006.

[52] M. Oevermann, S. Gerber, and F. Behrendt, "Euler–Lagrange/DEM simulation of wood gasification in a bubbling fluidized bed reactor," *Particuology,* vol. 7, no. 4, pp. 307-316, 2009, doi: 10.1016/j.partic.2009.04.004.

[53] Q. Xiong, K. Hong, F. Xu, J. Smith, and J. Chaouki, "CFD simulation of biomass thermochemical conversion: Model development, practical application and experimental validation," *Renewable Energy,* vol. 147, pp. 2043-2045, 2020, doi: 10.1016/j.renene.2019.10.013.

[54] S. Golshan, R. Sotudeh-Gharebagh, R. Zarghami, N. Mostoufi, B. Blais, and J. A. M. Kuipers, "Review and implementation of CFD-DEM applied to chemical process systems," *Chemical Engineering Science,* vol. 221, p. 115646, 2020, doi: 10.1016/j.ces.2020.115646.

[55] S. Wang, K. Luo, and J. Fan, "CFD-DEM coupled with thermochemical sub-models for biomass gasification: Validation and sensitivity analysis,"

Chemical Engineering Science, vol. 217, p. 115550, 2020, doi: 10.1016/j.ces.2020.115550.

[56] W. H. Ariyaratne, E. V. P. J. Manjula, C. Ratnayake, and M. C. Melaaen, "CFD approaches for modeling gas-solids multiphase flows–A review," in *Proceedings of The 9th EUROSIM Congress on Modelling and Simulation, EUROSIM 2016, The 57th SIMS Conference on Simulation and Modelling SIMS 2016*, 2018, no. 142: Linköping University Electronic Press, pp. 680-686.

[57] Z. Deng *et al.*, "Computational Fluid Dynamics Modeling of Coal Gasification in a Pressurized Spout-Fluid Bed," *Energy & Fuels,* vol. 22, no. 3, pp. 1560-1569, 2008, doi: 10.1021/ef7007437.

[58] A. Ramos, E. Monteiro, V. Silva, and A. Rouboa, "Co-gasification and recent developments on waste-to-energy conversion: A review," *Renewable and Sustainable Energy Reviews,* vol. 81, pp. 380-398, 2018, doi: 10.1016/j.rser.2017.07.025.

[59] R. Sun, T. M. Ismail, X. Ren, and M. A. El-Salam, "Numerical and experimental studies on effects of moisture content on combustion characteristics of simulated municipal solid wastes in a fixed bed," *Waste Management,* vol. 39, pp. 166-178, 2015, doi: 10.1016/j.wasman.2015.02.018.

[60] Y. B. Yang, V. N. Sharifi, and J. Swithenbank, "Effect of air flow rate and fuel moisture on the burning behaviours of biomass and simulated municipal solid wastes in packed beds," *Fuel,* vol. 83, no. 11-12, pp. 1553-1562, 2004, doi: 10.1016/j.fuel.2004.01.016.

[61] J. Collazo, J. Porteiro, D. Patiño, and E. Granada, "Numerical modeling of the combustion of densified wood under fixed-bed conditions," *Fuel,* vol. 93, pp. 149-159, 2012, doi: 10.1016/j.fuel.2011.09.044.

[62] N. Couto, V. Silva, E. Monteiro, P. Brito, and A. Rouboa, "Using an Eulerian-granular 2-D multiphase CFD model to simulate oxygen air enriched gasification of agroindustrial residues," *Renewable Energy,* vol. 77, pp. 174-181, 2015, doi: 10.1016/j.renene.2014.11.089.

[63] M. Sommerfeld, "Numerical methods for dispersed multiphase flows," in *Particles in flows*: Springer, 2017, pp. 327-396.

[64] G. Xiao *et al.*, "Experimental study on MSW gasification and melting technology," *Journal of Environmental Sciences,* vol. 19, no. 11, pp. 1398-1403, 2007, doi: 10.1016/s1001-0742(07)60228-9.

[65] L. M. Armstrong, S. Gu, and K. H. Luo, "Parametric Study of Gasification Processes in a BFB Coal Gasifier," *Industrial & Engineering Chemistry Research,* vol. 50, no. 10, pp. 5959-5974, 2011, doi: 10.1021/ie1023029.

[66] R. Sun, T. M. Ismail, X. Ren, and M. A. El-Salam, "Effect of ash content on the combustion process of simulated MSW in the fixed bed," *Waste Management,* vol. 48, pp. 236-249, 2016, doi: 10.1016/j.wasman.2015.10.007.

[67] R. Sun, T. M. Ismail, X. Ren, and M. A. El-Salam, "CFD Study on the Effect of Primary Air on Combustion of Simulated MSW Process in the Fixed Bed," *International Journal of Mechanical, Aerospace, Industrial, Mechatronic and Manufacturing Engineering,* vol. 9, pp. 612-621, 2015. [Online]. Available: http://waset.org/publications/10001138.

[68] R. Sun, T. M. Ismail, X. Ren, and M. A. El-Salam, "Influence of simulated MSW sizes on the combustion process in a fixed bed: CFD and

experimental approaches," *Waste Management,* vol. 49, pp. 272-286, 2016, doi: 10.1016/j.wasman.2015.12.019.

[69] D. Shin and S. Choi, "The Combustion of Simulated Waste Particles in a Fixed Bed," *Combustion and Flame,* vol. 121, no. 1, pp. 167-180, 2000, doi: 10.1016/S0010-2180(99)00124-8.

[70] W. P. Adamczyk, P. Kozołub, G. Węcel, A. Klimanek, R. A. Białecki, and T. Czakiert, "Modeling oxy-fuel combustion in a 3D circulating fluidized bed using the hybrid Euler–Lagrange approach," *Applied Thermal Engineering,* vol. 71, no. 1, pp. 266-275, 2014, doi: 10.1016/j.applthermaleng.2014.06.063.

[71] A. Frank and M. J. Castaldi, "CFD analysis of municipal solid waste combustion using detailed chemical kinetic modelling," *Waste Management & Research,* vol. 32, no. 8, pp. 745-754, 2014, doi: 10.1177/0734242X14538305.

[72] X. L. Huai *et al.*, "Numerical simulation of municipal solid waste combustion in a novel two-stage reciprocating incinerator," *Waste Management,* vol. 28, no. 1, pp. 15-29, 2008, doi: 10.1016/j.wasman.2006.11.010.

[73] M. Costa, N. Massarotti, A. Mauro, F. Arpino, and V. Rocco, "CFD modelling of a RDF incineration plant," *Applied Thermal Engineering,* vol. 101, pp. 710-719, 2016, doi: 10.1016/j.applthermaleng.2016.01.073.

[74] Y. He, A. E. Bayly, and A. Hassanpour, "Coupling CFD-DEM with dynamic meshing: A new approach for fluid-structure interaction in particle-fluid flows," *Powder Technology,* vol. 325, pp. 620-631, 2018, doi: 10.1016/j.powtec.2017.11.045.

[75] K. Kuwagi *et al.*, "Development of DEM–CFD simulation of combustion flow in incinerator with the representative particle model," *Journal of Chemical Engineering of Japan,* vol. 49, no. 5, pp. 425-434, 2016.

[76] H. Zhou, G. Flamant, and D. Gauthier, "DEM-LES of coal combustion in a bubbling fluidized bed. Part I: gas-particle turbulent flow structure," *Chemical Engineering Science,* vol. 59, no. 20, pp. 4193-4203, 2004.

[77] X. Ku, T. Li, and T. Løvås, "CFD–DEM simulation of biomass gasification with steam in a fluidized bed reactor," *Chemical Engineering Science,* vol. 122, pp. 270-283, 2015, doi: 10.1016/j.ces.2014.08.045.

[78] ANSYS® Academic Research Fluent, Release 20.2, Help System, *ANSYS Fluent Theory Guide* ANSYS, Inc., 2020.

[79] A. Di Renzo and F. P. Di Maio, "Comparison of contact-force models for the simulation of collisions in DEM-based granular flow codes," *Chemical Engineering Science,* vol. 59, no. 3, pp. 525-541, 2004, doi: 10.1016/j.ces.2003.09.037.

[80] K. Washino, E. L. Chan, T. Kaji, Y. Matsuno, and T. Tanaka, "On large scale CFD–DEM simulation for gas–liquid–solid three-phase flows," *Particuology,* vol. 59, pp. 2-15, 2021, doi: 10.1016/j.partic.2020.05.006.

[81] Y. Tsuji, T. Kawaguchi, and T. Tanaka, "Discrete particle simulation of two-dimensional fluidized bed," *Powder Technology,* vol. 77, no. 1, pp. 79-87, 1993, doi: 10.1016/0032-5910(93)85010-7.

[82] H. A. Navarro and M. P. de Souza Braun, "Determination of the normal spring stiffness coefficient in the linear spring–dashpot contact model of discrete element method," *Powder Technology,* vol. 246, pp. 707-722, 2013, doi: 10.1016/j.powtec.2013.05.049.

[83] O. R. Walton, "Numerical simulation of inelastic, frictional particle-particle interactions," *Particulate two-phase flow,* vol. 25, pp. 884-911, 1993.

[84] C. B. Fonte, J. A. Oliveira Jr, and L. C. de ALMEIDA, "DEM-CFD coupling: mathematical modelling and case studies using ROCKY-DEM® and ANSYS Fluent®," in *Eleventh International Conference on CFD in the Minerals and Process Industries CSIRO, Melbourne, Australia*, 2015.

[85] F. Wissing, S. Wirtz, and V. Scherer, "Simulating municipal solid waste incineration with a DEM/CFD method – Influences of waste properties, grate and furnace design," *Fuel,* vol. 206, pp. 638-656, 2017, doi: 10.1016/j.fuel.2017.06.037.

[86] J. Cheng, Y. Dou, N. Zhang, Z. Li, and Z. Wang, "A New Method for Predicting Erosion Damage of Suddenly Contracted Pipe Impacted by Particle Cluster via CFD-DEM," *Materials (Basel),* vol. 11, no. 10, p. 1858, 2018, doi: 10.3390/ma11101858.

[87] J. Hilton and P. Cleary, "Comparison of resolved and coarse grain DEM models for gas flow through particle beds," in *Ninth International Conference on CFD in the Minerals and Process Industries, Melbourne*, 2012.

[88] D. Queteschiner, T. Lichtenegger, S. Pirker, and S. Schneiderbauer, "Multi-level coarse-grain model of the DEM," *Powder Technology,* vol. 338, pp. 614-624, 2018, doi: 10.1016/j.powtec.2018.07.033.

[89] M. Sakai *et al.*, "Verification and validation of a coarse grain model of the DEM in a bubbling fluidized bed," *Chemical Engineering Journal,* vol. 244, pp. 33-43, 2014, doi: 10.1016/j.cej.2014.01.029.

[90] J. Lin, K. Luo, S. Wang, C. Hu, and J. Fan, "An augmented coarse-grained CFD-DEM approach for simulation of fluidized beds," *Advanced Powder Technology,* vol. 31, no. 10, pp. 4420-4427, 2020, doi: 10.1016/j.apt.2020.09.014.

[91] L. Jing, C. Y. Kwok, Y. F. Leung, and Y. D. Sobral, "Extended CFD-DEM for free-surface flow with multi-size granules," *International Journal for Numerical and Analytical Methods in Geomechanics,* vol. 40, no. 1, pp. 62-79, 2016, doi: 10.1002/nag.2387.

[92] W. Yin, S. Wang, K. Zhang, and Y. He, "Investigation of oxygen-enriched biomass gasification with TFM-DEM hybrid model," *Chemical Engineering Science,* vol. 211, p. 115293, 2020, doi: 10.1016/j.ces.2019.115293.

[93] F. Bambauer, S. Wirtz, V. Scherer, and H. Bartusch, "Transient DEM-CFD simulation of solid and fluid flow in a three dimensional blast furnace model," *Powder Technology,* vol. 334, pp. 53-64, 2018, doi: 10.1016/j.powtec.2018.04.062.

[94] S. Ueda, T. Kon, H. Kurosawa, S. Natsui, T. Ariyama, and H. Nogami, "Influence of Shape of Cohesive Zone on Gas Flow and Permeability in the Blast Furnace Analyzed by DEM-CFD Model," *ISIJ International,* vol. 55, no. 6, pp. 1232-1236, 2015, doi: 10.2355/isijinternational.55.1232.

[95] W. J. Yang, Z. Y. Zhou, A. B. Yu, and D. Pinson, "Particle scale simulation of softening–melting behaviour of multiple layers of particles

in a blast furnace cohesive zone," *Powder Technology,* vol. 279, pp. 134-145, 2015, doi: 10.1016/j.powtec.2015.04.002.

[96] J. E. Olsen and Q. G. Reynolds, "Mathematical Modeling of Furnace Drainage While Tapping Slag and Metal Through a Single Tap-Hole," *Metallurgical and Materials Transactions B,* vol. 51, no. 4, pp. 1750-1759, 2020, doi: 10.1007/s11663-020-01873-1.

[97] K.-i. Ohno, Y. Kitamura, S. Sukenaga, S. Natsui, T. Maeda, and K. Kunitomo, "Gas Permeability Evaluation of Granulated Slag Particles Packed Bed during Softening and Melting Stage with Fanning's Equation," *ISIJ International,* vol. 60, no. 7, pp. 1512-1519, 2020, doi: 10.2355/isijinternational.ISIJINT-2020-012.

[98] A. Celik, C. Bonten, R. Togni, C. Kloss, and C. Goniva, "A Novel Modeling Approach for Plastics Melting within a CFD-DEM Framework," *Polymers (Basel),* vol. 13, no. 2, p. 227, 2021, doi: 10.3390/polym13020227.

[99] W. J. Yang, Z. Y. Zhou, D. Pinson, and A. B. Yu, "A New Approach for Studying Softening and Melting Behavior of Particles in a Blast Furnace Cohesive Zone," *Metallurgical and Materials Transactions B,* vol. 46, no. 2, pp. 977-992, 2015, doi: 10.1007/s11663-014-0223-8.

[100] S. Natsui, S. Ishihara, T. Kon, K.-i. Ohno, and H. Nogami, "Detailed modelling of packed-bed gas clogging due to thermal-softening of iron ore by Eulerian–Lagrangian approach," *Chemical Engineering Journal,* vol. 392, p. 123643, 2020, doi: 10.1016/j.cej.2019.123643.

[101] M. Baniasadi, M. Baniasadi, and B. Peters, "Coupled CFD-DEM with heat and mass transfer to investigate the melting of a granular packed bed," *Chemical Engineering Science,* vol. 178, pp. 136-145, 2018, doi: 10.1016/j.ces.2017.12.044.

[102] M. Baniasadi, M. Baniasadi, and B. Peters, "Application of the extended discrete element method (XDEM) in the melting of a single particle," 2017.

[103] A. D. Brent, V. R. Voller, and K. J. Reid, "Enthalpy-Porosity Technique for Modeling Convection-Diffusion Phase Change: Application to the Melting of a Pure Metal," *Numerical Heat Transfer,* vol. 13, no. 3, pp. 297-318, 1988, doi: 10.1080/10407788808913615.

[104] Y. Feng, J. Gao, D. Feng, and X. Zhang, "Modeling of the molten blast furnace slag particle deposition on the wall including phase change and heat transfer," *Applied Energy,* vol. 248, pp. 288-298, 2019, doi: 10.1016/j.apenergy.2019.04.100.

[105] M. Sajjadi and J. Azaiez, "Heat and mass transfer in melting porous media: Stable miscible displacements," *International Journal of Heat and Mass Transfer,* vol. 88, pp. 926-944, 2015, doi: 10.1016/j.ijheatmasstransfer.2015.05.017.

[106] Q. Zhang, L. Dor, W. Yang, and W. Blasiak, "Eulerian Model for Municipal Solid Waste Gasification in a Fixed-Bed Plasma Gasification Melting Reactor," *Energy & Fuels,* vol. 25, no. 9, pp. 4129-4137, 2011, doi: 10.1021/ef200383j.

[107] V. Athawale, A. Bhattacharya, and P. Rath, "Prediction of melting characteristics of encapsulated phase change material energy storage systems," *International Journal of Heat and Mass Transfer,* vol. 181, p. 121872, 2021, doi: 10.1016/j.ijheatmasstransfer.2021.121872.

[108] M. Parsazadeh, M. Malik, X. Duan, and A. McDonald, "Numerical study on melting of phase change material in an enclosure subject to Neumann boundary condition in the presence of Rayleigh-Bénard convection," *International Journal of Heat and Mass Transfer,* vol. 171, p. 121103, 2021, doi: 10.1016/j.ijheatmasstransfer.2021.121103.

[109] J. Ni, Q. Liang, Z. Zhou, Z. Dai, and G. Yu, "Numerical and experimental investigations on gas–particle flow behaviors of the Opposed Multi-Burner Gasifier," *Energy Conversion and Management,* vol. 50, no. 12, pp. 3035-3044, 2009, doi: 10.1016/j.enconman.2009.07.023.

[110] M. Losurdo, H. Spliethoff, and J. Kiel, "Ash deposition modeling using a visco-elastic approach," *Fuel,* vol. 102, pp. 145-155, 2012, doi: 10.1016/j.fuel.2012.04.047.

[111] S. Li, Y. Wu, and K. J. Whitty, "Ash Deposition Behavior during Char−Slag Transition under Simulated Gasification Conditions," *Energy & Fuels,* vol. 24, no. 3, pp. 1868-1876, 2010, doi: 10.1021/ef901480e.

[112] D. Safronov *et al.*, "Numerical study on entrained-flow gasification performance using combined slag model and experimental characterization of slag properties," *Fuel Processing Technology,* vol. 161, pp. 62-75, 2017, doi: 10.1016/j.fuproc.2017.03.007.

[113] L. Chen and A. F. Ghoniem, "Simulation of Oxy-Coal Combustion in a 100 kWthTest Facility Using RANS and LES: A Validation Study," *Energy & Fuels,* vol. 26, no. 8, pp. 4783-4798, 2012, doi: 10.1021/ef3006993.

[114] L. Chen, S. Z. Yong, and A. F. Ghoniem, "Modeling the slag behavior in three dimensional CFD simulation of a vertically-oriented oxy-coal combustor," *Fuel Processing Technology,* vol. 112, pp. 106-117, 2013, doi: 10.1016/j.fuproc.2013.02.010.

[115] S. Z. Yong and A. Ghoniem, "Modeling the slag layer in solid fuel gasification and combustion – Two-way coupling with CFD," *Fuel,* vol. 97, pp. 457-466, 2012, doi: 10.1016/j.fuel.2012.02.063.

[116] F. Montagnaro and P. Salatino, "Analysis of char–slag interaction and near-wall particle segregation in entrained-flow gasification of coal," *Combustion and Flame,* vol. 157, no. 5, pp. 874-883, 2010, doi: 10.1016/j.combustflame.2009.12.006.

[117] T. Shimizu and H. Tominaga, "A model of char capture by molten slag surface under high-temperature gasification conditions," *Fuel,* vol. 85, no. 2, pp. 170-178, 2006, doi: 10.1016/j.fuel.2005.03.033.

[118] V. Jain, L. Kalo, D. Kumar, H. J. Pant, and R. K. Upadhyay, "Experimental and numerical investigation of liquid–solid binary fluidized beds: Radioactive particle tracking technique and dense discrete phase model simulations," *Particuology,* vol. 33, pp. 112-122, 2017, doi: 10.1016/j.partic.2016.07.011.

[119] A. Klimanek, W. Adamczyk, A. Katelbach-Woźniak, G. Węcel, and A. Szlęk, "Towards a hybrid Eulerian–Lagrangian CFD modeling of coal gasification in a circulating fluidized bed reactor," *Fuel,* vol. 152, pp. 131-137, 2015, doi: 10.1016/j.fuel.2014.10.058.

[120] C. Prakash, "Two-phase model for binary solid-liquid phase change, part II: Some illustrative examples," *Numerical Heat Transfer, Part B: Fundamentals,* vol. 18, no. 2, pp. 147-167, 1990/10/01 1990, doi: 10.1080/10407799008944947.

[121] F. Marchelli, Q. Hou, B. Bosio, E. Arato, and A. Yu, "Comparison of different drag models in CFD-DEM simulations of spouted beds," *Powder Technology*, vol. 360, pp. 1253-1270, 2020, doi: 10.1016/j.powtec.2019.10.058.

[122] B. E. Launder and D. B. Spalding, *Mathematical models of turbulence* (no. BOOK). Academic press, 1972.

[123] S. A. Orszag *et al.*, "Renormalisation group modelling and turbulence simulations," *Near-wall turbulent flows*, pp. 1031-1046, 1993.

[124] J. Kim, "A numerical study of the effects of ambient wind direction on flow and dispersion in urban street canyons using the RNG k-ε turbulence model," *Atmospheric Environment*, vol. 38, no. 19, pp. 3039-3048, 2004, doi: 10.1016/j.atmosenv.2004.02.047.

[125] S. A. J. Morsi and A. J. Alexander, "An investigation of particle trajectories in two-phase flow systems," *Journal of Fluid Mechanics*, vol. 55, no. 2, pp. 193-208, 1972.

[126] D. Gidaspow, *Multiphase flow and fluidization: continuum and kinetic theory descriptions*. Academic press, 1994.

[127] W. E. Ranz and W. R. Marshall, "Evaporation from drops," *Chem. Eng. Prog.*, vol. 48, no. 3, pp. 141-146, 1952.

[128] S. Patankar, *Numerical heat transfer and fluid flow*. Taylor & Francis, 2018.

[129] Z. Peng, E. Doroodchi, C. Luo, and B. Moghtaderi, "Influence of void fraction calculation on fidelity of CFD-DEM simulation of gas-solid bubbling fluidized beds," *AIChE Journal*, vol. 60, no. 6, pp. 2000-2018, 2014, doi: 10.1002/aic.14421.

[130] H. Hu and S. A. Argyropoulos, "Mathematical modelling of solidification and melting: a review," *Modelling and Simulation in Materials Science and Engineering*, vol. 4, no. 4, pp. 371-396, 1996/07/01 1996, doi: 10.1088/0965-0393/4/4/004.

[131] V. R. Voller, M. Cross, and N. C. Markatos, "An enthalpy method for convection/diffusion phase change," *International Journal for Numerical Methods in Engineering*, vol. 24, no. 1, pp. 271-284, 1987.

[132] A. D. Gosman and E. Loannides, "Aspects of Computer Simulation of Liquid-Fueled Combustors," *Journal of Energy*, vol. 7, no. 6, pp. 482-490, 1983, doi: 10.2514/3.62687.

[133] C. Y. Wen, "Mechanics of fluidization," in *Chem. Eng. Prog. Symp. Ser.*, 1966, vol. 62, pp. 100-111.

[134] S. Ergun, "Fluid Flow through Packed Columns," *Journal of Chemical Engineering Progress*, vol. 48, no. 2, pp. 89-94, 1952.

[135] L. Zhou *et al.*, "Experimental study and transient CFD/DEM simulation in a fluidized bed based on different drag models," *RSC Advances*, vol. 7, no. 21, pp. 12764-12774, 2017, doi: 10.1039/c6ra28615a.

[136] Y. L. Hao and Y. X. Tao, "Heat transfer characteristics of melting ice spheres under forced and mixed convection," *Journal of Heat Transfer*, vol. 124, no. 5, pp. 891-903, 2002.

[137] W. Guo, Y. Zhang, Z. Meng, P. Zhang, and S. Poncet, "Non-uniform melting of a spherical ice particle in free ascending," *International Journal of Heat and Mass Transfer*, vol. 148, 2020, doi: 10.1016/j.ijheatmasstransfer.2019.119097.

[138] A. Kaufmann, M. Moreau, O. Simonin, and J. Helie, "Comparison between Lagrangian and mesoscopic Eulerian modelling approaches for inertial particles suspended in decaying isotropic turbulence," *Journal of Computational Physics,* vol. 227, no. 13, pp. 6448-6472, 2008, doi: 10.1016/j.jcp.2008.03.004.

[139] Y. L. Hao and Y. X. Tao, "Non-thermal equilibrium melting of granular packed bed in horizontal forced convection. Part I: experiment," *International Journal of Heat and Mass Transfer,* vol. 46, no. 26, pp. 5017-5030, 2003, doi: 10.1016/s0017-9310(03)00359-4.

[140] S. Yang, Y. Sun, J. Wang, A. Cahyadi, and J. W. Chew, "Influence of operating parameters and flow regime on solid dispersion behavior in a gas–solid spout-fluid bed," *Chemical Engineering Science,* vol. 142, pp. 112-125, 2016, doi: 10.1016/j.ces.2015.11.038.

[141] R. Ramírez, T. Pöschel, N. V. Brilliantov, and T. Schwager, "Coefficient of restitution of colliding viscoelastic spheres," *Physical Review E,* vol. 60, no. 4, p. 4465, 1999.

[142] A. P. Hatzes, F. G. Bridges, and D. Lin, "Collisional properties of ice spheres at low impact velocities," *Monthly Notices of the Royal Astronomical Society,* vol. 231, no. 4, pp. 1091-1115, 1988.

[143] M. Higa, M. Arakawa, and N. Maeno, "Size dependence of restitution coefficients of ice in relation to collision strength," *Icarus,* vol. 133, no. 2, pp. 310-320, 1998.

[144] J. M. Gorman, A. Zheng, and E. M. Sparrow, "Bounding wall effects on fluid flow and pressure drop through packed beds of spheres," *Chemical Engineering Journal,* vol. 373, pp. 519-530, 2019, doi: 10.1016/j.cej.2019.05.068.

[145] S. W. Churchill, *Free convection around immersed bodies* (Heat Exchanger Design Handbook). New York: Begell House, 2002.

[146] T. L. Bergman, F. P. Incropera, D. P. DeWitt, and A. S. Lavine, *Fundamentals of heat and mass transfer,* 7th ed. Hoboken: John Wiley & Sons, 2011.

[147] J. Ou, A. Chatterjee, S. L. Cockcroft, D. M. Maijer, C. Reilly, and L. Yao, "Study of melting mechanism of a solid material in a liquid," *International Journal of Heat and Mass Transfer,* vol. 80, pp. 386-397, 2015, doi: 10.1016/j.ijheatmasstransfer.2014.09.022.

[148] Z. P. Zhang, L. F. Liu, Y. D. Yuan, and A. B. Yu, "A simulation study of the effects of dynamic variables on the packing of spheres," *Powder Technology,* vol. 116, no. 1, pp. 23-32, 2001, doi: 10.1016/S0032-5910(00)00356-9.

[149] H. Tangri, Y. Guo, and J. S. Curtis, "Packing of cylindrical particles: DEM simulations and experimental measurements," *Powder Technology,* vol. 317, pp. 72-82, 2017, doi: 10.1016/j.powtec.2017.03.058.

[150] W. Nan, Y. Wang, Y. Liu, and H. Tang, "DEM simulation of the packing of rodlike particles," *Advanced Powder Technology,* vol. 26, no. 2, pp. 527-536, 2015, doi: 10.1016/j.apt.2014.12.012.

[151] S. J. Chew, P. Zulli, D. Maldonado, and A. Yu, "Melt Down Behaviour of a Fused Layer in the Blast Furnace Cohesive Zone," *ISIJ International,* vol. 43, no. 3, pp. 304-313, 2003, doi: 10.2355/isijinternational.43.304.

[152] G. Wei, H. Zhang, X. An, and D. E, "Numerical investigation on the mutual interaction between heat transfer and non-spherical particle

dynamics in the blast furnace raceway," *International Journal of Heat and Mass Transfer,* vol. 153, p. 119577, 2020, doi: 10.1016/j.ijheatmasstransfer.2020.119577.

[153] A. Di Renzo, E. Napolitano, and F. Di Maio, "Coarse-Grain DEM Modelling in Fluidized Bed Simulation: A Review," *Processes,* vol. 9, no. 2, p. 279, 2021, doi: 10.3390/pr9020279.

[154] K. Chu, J. Chen, and A. Yu, "Applicability of a coarse-grained CFD–DEM model on dense medium cyclone," *Minerals Engineering,* vol. 90, pp. 43-54, 2016, doi: 10.1016/j.mineng.2016.01.020.

[155] G. Soon, H. Zhang, C. Yang, and A. W.-K. Law, "Simulations of Melting in Fluid-filled Packed Media due to Forced Convection with Higher Temperature," *International Journal of Heat and Mass Transfer,* vol. 175, p. 121358, 2021, doi: 10.1016/j.ijheatmasstransfer.2021.121358.

[156] M. Sakai and S. Koshizuka, "Large-scale discrete element modeling in pneumatic conveying," *Chemical Engineering Science,* vol. 64, no. 3, pp. 533-539, 2009, doi: 10.1016/j.ces.2008.10.003.

[157] L. Wu, M. Gong, and J. Wang, "Development of a DEM–VOF Model for the Turbulent Free-Surface Flows with Particles and Its Application to Stirred Mixing System," *Industrial & Engineering Chemistry Research,* vol. 57, no. 5, pp. 1714-1725, 2018, doi: 10.1021/acs.iecr.7b04833.

[158] L. Ge, Z. Peng, R. Moreno-Atanasio, E. Doroodchi, and G. M. Evans, "Three-Dimensional VOF-DEM Model for Simulating Particle Dynamics in the Liquid Slugs of a Vertical Gas–Liquid–Solid Taylor Flow Microreactor," *Industrial & Engineering Chemistry Research,* vol. 59, no. 16, pp. 7965-7981, 2020, doi: 10.1021/acs.iecr.0c00108.

[159] Z. Peng, L. Ge, R. Moreno-Atanasio, G. Evans, B. Moghtaderi, and E. Doroodchi, "VOF-DEM study of solid distribution characteristics in slurry Taylor flow-based multiphase microreactors," *Chemical Engineering Journal,* vol. 396, p. 124738, 2020, doi: 10.1016/j.cej.2020.124738.

[160] D. Qian and A. Lawal, "Numerical study on gas and liquid slugs for Taylor flow in a T-junction microchannel," *Chemical Engineering Science,* vol. 61, no. 23, pp. 7609-7625, 2006, doi: 10.1016/j.ces.2006.08.073.

[161] S. Heberlein, W. P. Chan, A. Veksha, A. Giannis, L. Hupa, and G. Lisak, "High temperature slagging gasification of municipal solid waste with biomass charcoal as a greener auxiliary fuel," *Journal of Hazardous Materials,* vol. 423, p. 127057, 2022, doi: 10.1016/j.jhazmat.2021.127057.

[162] W. J. Song, L. H. Tang, X. D. Zhu, Y. Q. Wu, Z. B. Zhu, and S. Koyama, "Effect of Coal Ash Composition on Ash Fusion Temperatures†," *Energy & Fuels,* vol. 24, no. 1, pp. 182-189, 2010, doi: 10.1021/ef900537m.

[163] A. Fourcault, F. Marias, and U. Michon, "Modelling of thermal removal of tars in a high temperature stage fed by a plasma torch," *Biomass and Bioenergy,* vol. 34, no. 9, pp. 1363-1374, 2010, doi: 10.1016/j.biombioe.2010.04.018.